UNIVERSITY OF CALIFORNIA,
IRVINE

Fabrication and Characterization of Lithographically Patterned Nanostructured Mesoscale Optical Materials

DISSERTATION

submitted in partial satisfaction of the requirements
for the degree of

DOCTOR OF PHILOSOPHY

in Chemistry

by

Han Wai Millie Fung

Dissertation Committee:
Professor Robert Corn, Chair
Professor Reginald Penner
Professor Rachel Martin

2019

DEDICATION

To my family: Mom, Dad, Mimi, and Han-Chi

for their unconditional love

TABLE OF CONTENTS

LIST OF FIGURES

ACKNOWLEDGMENTS

As I reflect on my time in graduate school, there are several individuals I would like to acknowledge for their help and support. First, I would like to express the deepest appreciation to my advisor and committee chair, Professor Robert Corn. Thank you for your endless ideas, patience, and guidance over the years. Thank you for encouraging me to explore and pursue my research interests; I'm proud to say that I've worked with almost every single instrument in the lab. I would also like to thank the other members of my Ph.D. committee, Professor Reginald Penner and Professor Rachel Martin. Thank you for your encouragement and support.

Next, I would like to thank the wonderful scientists I collaborated with: Dr. Mana Toma and Dr. Gabriel Loget, for starting the nanocone arrays project. George, thanks for showing me how to make nanocones when I first joined the lab. Dr. Seulgi So and Kellen Kartub, for helping with experiments and writing our manuscripts. I would also like to thank Dr. Dima Fishman from the Laser Spectroscopy Laboratories, Dr. Jian-Guo Zheng, Dr. Qiyin Lin, as well as the other staff of IMRI, for training and helping me on many instruments.

I am extremely grateful for the past and present members of the Corn Lab for research discussions, but more importantly, for your support and friendship. Mike, I will remember our ping pong and tennis sessions fondly. Jen, I am so grateful for your friendship. I can't wait to get coffee with you and Suzie (and little Arthur!) soon! Anna, thank you for being the voice of reason. Brandon, we need to get breakfast and BBQ again. Gerald, thanks for discovering my talents in fantasy football. Kellen, thank you for all your help in research, from running experiments to revising manuscripts and grants. I also had a great time doing outreach with you; definitely some of the best times in graduate school. Chloe, thanks for the talks, sticker runs, and "Starbucks runs." Alana, you'll always be an honorary group member. I'll never forget the time we were mesmerized at the car wash. Also, thanks to you and Will for always taking care of me. Erin, Yuhei, and Hiroshi: it was such a pleasure to have you in the group! Finally, to Adam, the best office mate: I couldn't have done it without you! Thank you for all your helpful research discussions, but more importantly, thank you for being a wonderful friend.

To my friends, thank you for keeping me sane over the years. Mike, I really cherish our friendship. Thanks for the Disney runs, Dunkin breakfasts, and other shenanigans. Winfong and Nate: thanks for taking me in for Thanksgiving over the past five years. Jeff and Ben, thanks for always checking up on me. Teresa, Steph, and Ash: you're like family to me. Thanks for always letting me crash at your places. Also, thanks for all your words of encouragement, and thanks for letting me practice my defense talk with you.

I am also grateful for my peers and professors I had the chance to work with at UCI; I learned a lot from all of you! To ISP, the Chem Outreach Program, and Sharks with Lasers: thanks for providing an outlet when I needed a break from work. I would also like to thank Professor Katherine Maloney, you're my advisor forever; thanks for supporting everything I've done in my science career. Thank you to Dr. Chris Fox, for encouraging me to go to graduate school in the first place.

Finally, thank you to my family. Mom, Dad, Mimi, and Han-Chi: thank you for your unconditional love and support. I love you guys so much!

The work present in this dissertation was made possible by funding from the National Science Foundation (through grant CHE-1403506).

CURRICULUM VITAE

Han Wai Millie Fung

EDUCATION

Ph.D., Chemistry, University of California, Irvine — Dec 2018
B.S., Joint Chemistry and Biology, Harvey Mudd College — May 2011

RESEARCH AND PROFESSIONAL EXPERIENCE

Graduate Researcher, UC Irvine, Irvine, CA — Feb 2014 – Jan 2019

- Advisor: Professor Robert Corn
- Dissertation: Fabrication and Characterization of Lithographically Patterned Nanostructured Mesoscale Optical Materials

Process Development Associate, IDRI, Seattle, WA — Aug 2011 – Aug 2013

- Advisor: Dr. Christopher Fox
- Physicochemical Characterization of Colloidal Vaccine Adjuvant Formulations used for Clinical Trials

Summer Intern, IDRI, Seattle, WA — Jun 2011 – Aug 2011

- Advisor: Ayesha Misquith
- Purification of Bioactive Proteins for Vaccine Products

Undergraduate Researcher, Harvey Mudd College, Claremont, CA — Jan 2010 – May 2011

- Advisor: Professor Katherine Maloney
- Senior Thesis: Progress towards the Isolation and Structure Elucidation of Antibiotic Compounds Produced by Endophytic Fungus from *Ribes viburnifolium*

TEACHING ASSISTANT EXPERIENCE

UC Irvine, Chemistry Department

- Chem 249 Analytical Spectroscopy — Winter 2018
- Chem M3LC, Quantitative Chemistry Lab, Co-Head TA — Spring 2015
- Chem 1B General Chemistry Lecture — Winter 2014
- Chem 1LC General Chemistry Lab — Spring 2014
- Chem 1LD General Chemistry Lab — Fall 2013, Summer 2017

PUBLICATIONS

1. **H.W. Millie Fung**, Seulgi So, Kellen Kartub and Robert M. Corn, "Quantitative Characterization of Optical Coupling in Nanoporous ZnO-WO_3 and ZnO-PEDOT Composite Electrodeposited Gratings using Electrodiffraction Measurements" *Submitted for publication.*
2. **H.W. Millie Fung**, Seulgi So, Kellen Kartub, Gabriel Loget and Robert M. Corn, "Ultra-Antireflective Electrodeposited Plasmonic and PEDOT Nanocone Array Surfaces" *J. Phys. Chem. C,* **121,** 22377-22383 (2017).
3. Seulgi So, **H.W. Millie Fung**, Kellen Kartub, Adam M. Maley and Robert M. Corn, "Fabrication of PEDOT Nanocone Arrays with Electrochemically Modulated Broadband Antireflective Properties" *J. Phys. Chem. Lett.*, **8,** 576-579 (2017).

4. Lauri Viitala, Adam M. Maley, **H.W. Millie Fung**, Robert M. Corn, Tapani Viitala and Lasse Murtomaki,
   "Surface Plasmon Resonance Imaging Microscopy of Liposomes and Liposome-Encapsulated Gold Nanoparticles" *J. Phys. Chem. C*, **120,** 25958-25966 (2016).
5. Christopher B. Fox, Sean Mulligan, Joyce Sung, Quinton M. Dowling, **H.W. Millie Fung**, Thomas S. Vedvick, Rhea N. Coler. "Cryo-Transmission Electron Microscopy of Recombinant Tuberculosis Vaccine Antigen with Anionic Liposomes Reveals Formation of Flattened Liposomes" *Intl. J. Nanomed.*, **9,** 1367-1377 (2014).
6. **H.W. Millie Fung[1]**, Ayesha Misquith[1], Quinton M. Dowling, Jeffrey A. Guderian, Thomas S. Vedvick, Christopher B. Fox. "In Vitro Evaluation of TLR4 Agonist Activity: Formulation Effects" *Colloids Surf. B*, **113,** 312-319 (2014).
7. **H.W. Millie Fung**, Traci J.T. Mikasa, Julie Vergara, Sandra J. Sivananthan, Jeffrey A. Guderian, Malcolm S. Duthie, Thomas S. Vedvick, Christopher B. Fox. "Optimizing Manufacturing and Composition of a TLR4 Nanosuspension: Physicochemical Stability and Vaccine Adjuvant Activity" *J Nanobiotechnol*, **11,** 43 (2013).

PRESENTATIONS

1. **H.W. Millie Fung**. "Single Nanoparticle SPRI Microscopy for the Enzymatic Detection of Single MicroRNA Molecules" *American Chemical Society 251st National Meeting*, San Diego, CA, Mar 16, 2016. Oral Presentation.
2. **H.W. Millie Fung** and Robert M. Corn. "Fabrication of Flexible Plasmonic Nanocone Array Surfaces with Broadband Anti-reflectivity and Tunable Hydrophobicity for Photovoltaic, Catalytic, and Biosensing Applications" *Pacifichem 2015*, Honolulu, HI, Dec 16, 2015. Poster Presentation.
3. **Millie Fung**. "Progress towards the Isolation and Structure Elucidation of Antibiotic Compounds Produced by Endophytic Fungus from Ribes viburnifolium" *Harvey Mudd College Presentation Days: A Celebration of Student Projects*, Claremont, CA, May 1, 2011. Oral Presentation.
4. **Millie Fung**, Caitlin M. Olmsted and Katherine N. Maloney. "Progress towards the Isolation and Structure Elucidation of Antibiotic Compounds Produced by Endophytic Fungus from *Ribes viburnifolium*" *American Chemical Society 241st National Meeting*, Anaheim, CA, Mar 27, 2011. Poster Presentation.

PATENTS

"Nanostructured Arrays on Flexible Polymer Films," United States Patent: 10006085; Inventors: Corn R.M., Toma M., Loget G., **Fung H.W.M.** June 26, 2018.

HONORS

NSF Graduate Research Fellowship Program Honorable Mention 2015

PROFESSIONAL MEMBERSHIPS

American Chemical Society
Iota Sigma Pi National Honor Society for Women in Chemistry – Calcium Chapter

ABSTRACT OF THE DISSERTATION

Fabrication and Characterization of Lithographically Patterned Nanostructured Mesoscale Optical Materials

By

Han Wai Millie Fung

Doctor of Philosophy in Chemistry

University of California, Irvine, 2019

Professor Robert Corn, Chair

This dissertation presents the study of lithographically patterned nanostructured mesoscale optical materials with potential applications in biomedical devices, chemical sensing, and energy storage. We describe the fabrication and characterization of two types of nanostructured mesoscale surfaces: periodic nanocone arrays and diffraction gratings. The first part of the dissertation focuses on our research on periodic nanocone arrays. Using a straight-forward fabrication process, periodic nanocone arrays are created through oxygen plasma etching of hexagonally close-packed polystyrene bead monolayers on polymer surfaces. The periodicity and the height of the nanocone arrays are controlled by the polystyrene bead diameter and the overall etching time, due to the differential etching rates of the bead and the polymer surface underneath. These nanocone arrays exhibit broadband antireflectivity over a wide spectral range (450 – 800 nm) at various angles of incidence ($8° \leq \theta \leq 67.5°$). In Chapter 2, we present the interesting electrochemically modulated optical properties shown by periodic nanocone arrays composed of the electroactive polymer poly(3,4-ethylenedioxythiophene) (PEDOT). Electrochemical modulation of the oxidation state of PEDOT nanocone arrays was used to

change both its optical absorption (electrochromism) and reflection (electroreflectivity). In Chapter 3, we demonstrate that nanocone arrays modified with a nanostructured zinc oxide (ZnO) thin film on the surface exhibited a very low broadband reflectivity of less than 0.1% at a wide range of incident angles. The ultra-antireflective ZnO-coated nanocone array surfaces also exhibited an enhanced photoreactivity for the oxidative degradation of methylene blue, suggesting their potential as self-cleaning antireflective surfaces. The final chapter of this dissertation shifts focus to mesoscale diffraction gratings. Electrodiffractive and electrochromic properties were investigated from a novel two-component composite nanostructured electrodeposited grating that incorporated both ZnO and either tungsten oxide (WO_3) or PEDOT. The sequential electrodeposition of these two materials through a photopatterned photoresist layer onto a fluorine-doped tin oxide (FTO) coated glass substrate created a grating structure that exhibited optical diffraction that could be modulated electrochemically. While the nanostructured ZnO is non-absorbing, its high refractive index and large surface area redirect light into the electrochromic grating and create a four-fold enhancement in the grating's electrodiffractive response.

Chapter 1

Introduction

1.1 Dissertation Overview

The plethora of unique optical effects presented by nanostructured materials have led to applications in several fields such as biomedical devices,[1-4] chemical sensing,[5-8] and energy storage.[9-12] For example, biomolecule-functionalized gold nanoparticles have long been used in ultrasensitive surface plasmon-based biosensing schemes.[13-16] In addition, sub-wavelength silicon nanopillars are often incorporated in high-efficiency solar panels to minimize the energy lost through reflection.[17-21] In recent years, however, there has been increased interest in examining the collective effects of nanomaterials at the mesoscale dimensions.[22-23] The mesoscale ranges from the nanometer (~10 nm) to the micrometer (~10 μm) dimensions. This is

the domain where ensemble effects and properties relevant to macroscopic phenomena emerge, and generally can no longer be described by atomic and molecular behavior alone. At the mesoscale, defects, interfaces, and heterogeneous structures are common, and these collective interactions can result in novel properties that are not found in the nano- or macroscale dimensions alone. Mesoscale materials are often synthesized via the assembly of atomic or nanoscale building blocks. Examples include composite materials, optical metamaterials, self-assembled nanoparticles, and biological membranes.[24-28]

The interest in nanostructured mesoscale materials has called for the development of simple, inexpensive, and high-throughput processes for the fabrication of arrays composed of a large number of materials. While electron beam lithography (EBL) can be used to create nanostructures on the scale of tens to hundreds of microns,[29-30] the time and cost required to fabricate arrays over larger areas (on the squared cm scale) using EBL is not feasible. Alternatively, patterned nanostructures have been fabricated using methods such as nanochannel glass replica membranes, colloidal lithography, and evaporative self-assembly.[31-34] The Corn Lab has presented novel methods to create a variety of nanostructured surfaces over large areas (on the squared cm scale) via a combination of colloidal lithography, oxygen plasma etching, photolithography, and electrochemistry.[4, 35-38]

In this dissertation, we describe the interesting optical effects exhibited by large-area nanocone array surfaces and two-component composite diffraction gratings that exhibit both nanoscale and mesoscale dimensions. In Chapter 2, we discuss the broadband electrochemically modulated reflectivity of sub-wavelength electroactive nanocone arrays. Next, Chapter 3 details the fabrication and characterization of ultra-antireflective electrodeposited composite nanocone arrays. Finally, Chapter 4 describes the fabrication of mesoscale composite diffraction gratings

that exhibit optical coupling between a non-absorptive high refractive index material and an absorptive host material.

1.2 Broadband Antireflective Nanocone Array Surfaces

Antireflective coatings can reduce reflection and increase the quality of optical systems. They are found in a variety of applications ranging from camera manufacturing, flat screen displays, high performance lenses, and photovoltaic devices. For example, antireflective surfaces on solar cells can improve their efficiency as less light is lost from reflection. The basic concept of reflectivity can be explained by a transition in the medium in which light is travelling. The medium (glass, water, air, and others) is characterized optically by the refractive index (n) which quantifies the speed of light in the current medium with respect to the speed of light in vacuum. As light travels, our eyes can spot an optical disturbance if there is a change in refractive index. The Fresnel equations represent the basic mathematical model of reflectivity in relation to the refractive indices of the media[39]. At normal incidence, the intensity of the light reflected (R) is described by Equation 1:

$$R = \left[\frac{n_1 - n_2}{n_1 + n_2}\right]^2 \quad (1)$$

where n_1 = refractive index of air

n_2 = refractive index of the surface

When $n_1 = n_2$, $R = 0$, indicating reflection is completely suppressed.

To improve antireflective surfaces, researchers have looked to nature for inspiration. Periodic nanostructures are commonly found in nature, and their unique properties have inspired scientists to create biomimetic nanostructures for practical applications. For example, moths possess cornea that are 0.1% reflective in the visible spectral range. The low reflectivity of the corneal surface allows for improved light transmission so that moths can see better in the dark. Scanning electron microscopy (SEM) demonstrates that the corneal surface of moth eyes are comprised of cone-like structures with sub-wavelength height protuberances, typically ~200 nm in diameter and ~300 nm apart from each other.[39,40]

The broadband antireflective properties of these nanocone structures are attributed to the gradual refractive index change between air and the surface. In this case, the reflectivity of nanocone array surface can be viewed as a resultant of an infinite series of reflection at each incremental change in refractive index at various depths of each individual nanocone. If there is an optical distance of $\frac{\lambda}{2}$ between the incident light at various depths of the nanocone, there will be destructive interference, and reflectivity will be suppressed.[41,42]

Multiple fabrication methods have been developed to replicate biomimetic nanocone arrays. Notably, “top-down” technologies, such as electron-beam etching and nanoimprint lithography, have been applied to fabricate periodic nanocone arrays. Although these techniques allow precise control of the nanocone array dimensions, these methods are costly, slow, and very limited in the obtainable nanostructured areas (typically on the square μm scale). Alternatively, "bottom-up" method combining colloidal lithography and reactive ion etching has also been explored.[43,44] In this method, a colloidal monolayer is used as an etching mask, which allows for fabrication of nanostructured arrays on a larger scale.

Recently, the Corn group developed a simple, two-step method to fabricate two-

dimensional, periodic nanocone arrays on flexible Teflon films over large surface areas (on the square cm scale). As shown in Figure 1.1, in our approach, oxygen plasma etching of a colloidal monolayer of polystyrene (PS) beads on a Teflon film is employed. The simultaneous competitive differential etching of the PS beads and the Teflon is responsible for creating the nanocone arrays.

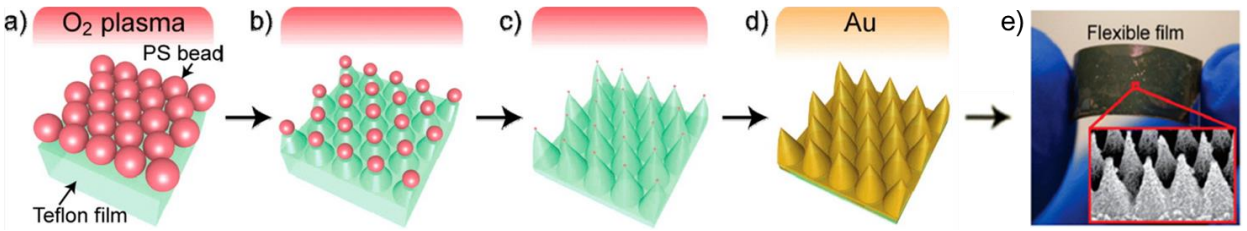

Figure 1.1. Schematic of the two-step fabrication process[7]. a) Formation of a polystyrene (PS) bead monolayer on a flexible Teflon film via spincoating. b), c) Formation of nanocone arrays via simultaneous plasma etching of PS beads and Teflon film. d) Vapor deposition of gold thin film on the Teflon nanocone array. e) The flexible gold-coated Teflon nanocone array surface appears black visually.

In this versatile fabrication scheme, PS bead diameter and etching time control the periodicity and height, respectively, of the Teflon nanocone arrays. Subsequent modification of these nanocone arrays with a plasmonic material allow for the tunability of the surface's optical properties. For example, after 50 nm of gold was vapor deposited onto the Teflon nanocone arrays, a combination of diffractive scattering loss and localized plasmonic absorption attributed to the gold nanocone arrays' reflectivity of less than 1% over a wide spectral range (400–900 nm) at a wide range of incident angles (0–65°).[36] In Chapter 2, we present the interesting electrochemically modulated optical properties shown by periodic nanocone arrays composed of the electroactive polymer poly(3,4-ethylenedioxythiophene) (PEDOT). Then, Chapter 3 describes ultra-antireflective ZnO-coated nanocone array surfaces that exhibit a very low

broadband reflectivity of less than 0.1% at a wide range of incident angles.

1.3 Optical Enhancement using Zinc Oxide

Zinc oxide's (ZnO) well-documented optical properties have been utilized for a variety of light-based applications. For example, its wide band gap (3.37 eV) has made ZnO a popular semiconductor material for photosensitized dyes with enhanced photovoltaic efficiency.[45-47] In addition to its semiconductor capabilities, ZnO has been observed to enhance the optical properties within various systems. ZnO was reported to improve the light trapping capabilities of solar cells both as a thin film on an absorbing material[48] and as a nanopatterned surface.[49-50] In our lab, we create nanostructured ZnO films on nanocone arrays and micron size gratings to create broadband ultra-antireflecive surfaces and enhanced electrochemically modulated diffraction gratings, respectively. These mesoscale structures present striking optical effects: while ZnO has no absorptive properties itself, it seems to enhance those of the host material beneath. As discussed in Chapters 3 and 4, we believe the enhanced optical effects observed in composite nanocone arrays and diffraction gratings are a result of optical coupling between the nanostructured ZnO and absorptive host material underneath.

1.4 Electrochemically Modulated Optical Properties

Electrochromic materials have the ability to change their optical properties as a result of redox reactions induced by an electric field charge intercalation.[51-53] With the ability to modulate transmittance, absorbance, and reflectivity, electrochromic materials have found applications in the development of optical devices such as smart windows, anti-glare displays, and sensors.[54-58]

Typically, the switching between redox states results in the generation of different visible region electronic absorption bands, thus a color change is observed upon an applied electric field.[51-53] Both organic and inorganic compounds have been utilized as electrochromic materials, but we will focus on the organic conductive polymer poly(3,4-ethylenedioxythiophene) (PEDOT) and the inorganic material tungsten oxide (WO_3) in this dissertation. PEDOT has been widely studied due to its high stability, moderate band gap, and low reduction potential. Typically, PEDOT undergoes a color change between a dark blue color in its neutral state and a lighter blue color in its oxidized state.[59-62] As seen in Figure 1.2, the absorption band of an electrodeposited PEDOT thin film shifts under different applied potentials. This is responsible for the visible color changes of the film, as shown in the photos of Figure 1.2.

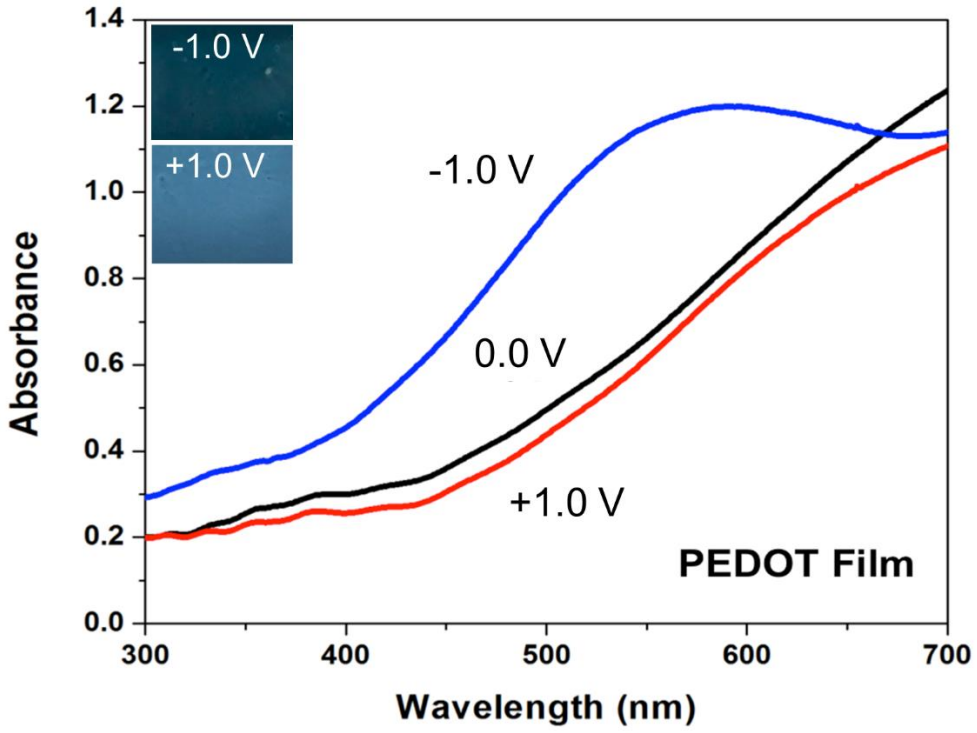

Figure 1.2. Electrochromic behavior of PEDOT thin films. UV-Vis absorption spectra of PEDOT thin films removed from solution after 20 s under potentiostatic control at three potentials: −1.0 V (blue spectrum), 0.0 V (black spectrum) and +1.0 V (red spectrum) vs. Ag/AgCl. The two inserted photographs show the different colors of PEDOT at −1.0 V (dark-blue/black) and +1.0 V (blue).

Similarly, WO_3 has also been one of the most extensively studied electrochromic materials due to its highly desired physical properties: strong coloration contrast, fast color switching kinetics, and stability. The optical effect is created through an electrochemical ion intercalation and redox process expressed in Equation 2:

$$WO_3 + xM^+ + xe^- \leftrightarrow M_xWO_3 \quad (2)$$

where M^+ denotes intercalated cations

Under the application of an external electric field, the ions move into and out of WO_3 and a color change is observed. Since the edge- and corner-sharing WO_6 octahedra in WO_3 form periodic structures with openings in interstitial sites, ion motion and intercalation into WO_3 is made possible. When WO_3 is cathodically charged, intercalated cations M^+ (typically small ions such as H^+ or Li^+) are compensated by injected electrons, which reduce tungsten cations from W_6^+ to W_5^+. This leads to a change in electron density of WO_3, causing a shift in its band gap and optical absorption. As a result, WO_3 transforms from a transparent/pale-yellow color to a blue color upon reduction.[54, 63-65]

While most research has focused on the tunability of the transmittance of PEDOT of WO_3 thin films for electrochromic surfaces, in Chapter 2, we explore the electrochemical modulation of reflectivity of a nanostructured PEDOT surface. By combining the electrochromic nature of PEDOT and the antireflective nature of sub-wavelength nanocone arrays, we fabricated and characterized nanostructured surfaces with broadband antireflectivity that could be controlled by electrochemical modulation. Then, in Chapter 4, we discuss electrochemically modulated diffraction in mesoscale electrodeposited PEDOT and WO_3 gratings.

1.5 Diffraction Gratings for Electrodiffraction Measurements

In Chapter 4, we shift our focus from nanocone arrays to mesoscale electroactive diffraction gratings in order to measure electrochemically modulated diffraction. Using a straight-forward fabrication process that combines photolithography and electrochemistry, we are able to create diffraction gratings with micron wide, centimeter long stripes with nanoscale heights. As shown in the schematic in Figure 1.3, a layer of positive photoresist in spincoated onto a conductive fluorine-doped tin oxide (FTO) glass substrate. Then, the photomask with micron wide chromium lines and glass spacings is placed flushed onto the substrate. The photoresist is exposed through the photomask using UV light, and the substrate is patterned and developed. Next, electrodeposition is performed to create a patterned surface composed of a variety of organic and inorganic materials. As long as the surface remains conductive, electrodeposition can be performed multiple times to create composite diffraction gratings. Finally, the photoresist is removed using acetone.

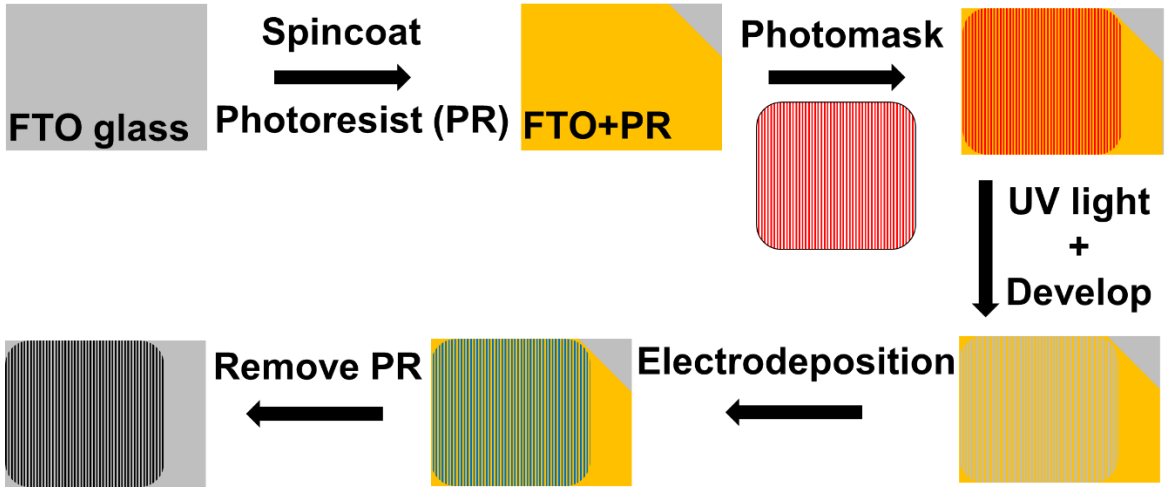

Figure 1.3. The fabrication scheme for creating large scale (on the squared centimeter scale) diffraction grating surfaces using a combination of photolithography and electrodeposition.

As electrodeposition is an inexpensive and versatile method for creating squared centimeter scale surfaces composed of a variety of organic and inorganic materials,[37,66-68] our lab has taken advantage of creating multi-component composite diffraction gratings. These diffraction gratings with both nanoscale and mesoscale dimensions exhibit unique optical properties, as they will be utilized to examine enhanced optical effects due to optical coupling between the various components.

In Chapter 4, we quantitatively characterized the optical coupling between ZnO (a high refractive index, but non-absorptive material) and an absorptive material (either tungsten oxide (WO_3) or poly(3,4-ethylenedioxythiophene) (PEDOT)). Electrodiffractive and electrochromic properties were investigated from a novel two-component composite nanostructured electrodeposited grating that incorporated both ZnO and either WO_3 or PEDOT. The sequential electrodeposition of these two materials through a photopatterned photoresist layer onto a fluorine-doped tin oxide (FTO) coated glass substrate created a grating structure that exhibited optical diffraction that could be modulated electrochemically.

1.6 References

1. Miller, M. M.; Prinz, G. A.; Cheng, S.-F.; Bounnak, S. Detection of a Micron-Sized Magnetic Sphere Using a Ring-Shaped Anisotropic Magnetoresistance-Based Sensor: A Model for a Magnetoresistance-Based Biosensor. *Appl. Phys. Lett.* **2002,** *81*, 2211–2213.

2. Larsson, E. M.; Alegret, J.; Kall, M.; Sutherland, D. S. Sensing Characteristics of NIR Localized Surface Plasmon Resonances in Gold Nanorings for Application as Ultrasensitive Biosensors. *Nano Lett.* **2007,** *7*, 1256–1263.

3. Clark, A. W.; Glidle, A.; Cumming, D. R. S.; Cooper, J. M. Plasmonic Split-Ring Resonators as Dichroic Nanophotonic DNA Biosensors. *J. Am. Chem. Soc.* **2009,** *131*, 17615–17619.

4. Loget, G.; Corn, R. M. Silica Nanowire Arrays for Diffraction-Based Bioaffinity Sensing. *Chem. Eur. J.* 2014, ***20***, 10802–10810.

5. Willets, K. A.; Van Duyne, R. P. Localized Surface Plasmon Resonance Spectroscopy and Sensing. *Annu. Rev. Phys. Chem.* **2007,** *58*, 267–297.

6. Wang, S.-C.; Shaikh, M. O. A Room Temperature H_2 Sensor Fabricated using High Performance Pt-Loaded SnO_2 Nanoparticles. *Sensors* **2015,** *15*, 14286–14297.

7. Gu, H.; Wang, Z.; Hu, Y. Hydrogen Gas Sensors Based on Semiconductor Oxide Nanostructures. *Sensors* **2012,** *12*, 5517–5550.

8. Li, X.; Liu, Y.; Hemminger, J. C.; Penner, R. M. Catalytically Activated Palladium@ Platinum Nanowires for Accelerated Hydrogen Gas Detection. *ACS Nano* **2015,** *9*, 3215–3225.

9. Rolison, D. R.; Long, R. W.; Lytle, J. C.; Fischer, A. E.; Rhodes, C. P.; McEvoy, T. M.; Bourga, M. E.;Lubers, A. M. Multifunctional 3D Nanoarchitectures for Energy Storage and Conversion. *Chem. Soc. Rev.* **2009,** *38*, 226–252.

10. Xia, H.; Feng, J.; Wang, H.; Lai, M. O.; Lu, L. MnO_2 Nanotube and Nanowire Arrays by Electrochemical Deposition for Supercapacitors. *J. Power Source* **2010,** *195*, 4410–4413.

11. Shir, D.; Yoon, J.; Chanda, D.; Ryu, J.-H.; Rogers, J. A. Performance of Ultrathin Silicon Solar Microcells with Nanostructures of Relief Formed by Soft Imprint Lithography for Broad Band Absorption Enhancement. *Nano Lett.* **2010,** *10*, 3041–3046.

12. Huo, F.; Li, Y.; To, S.; Liu, T.; Xue, C. Optimal Design of Broadband Antireflective Subwavelength Gratings for Solar Applications. *Optik* **2015,** *126*, 2626–2628.

13. He, L.; Musick, M. D.; Nicewarner, S. R.; Salinas, F. G.; Benkovic, S. J.; Natan, M. J.; Keating, C. D. Colloidal Au-Enhanced Surface Plasmon Resonance for Ultrasensitive Detection of DNA Hybridization. *J. Am. Chem. Soc.* **2000,** *122*, 9071-9077.

14. Lee, H. J.; Wark, A. W.; Corn, R. M. Enhanced Bioaffinity Sensing using Surface Plasmons, Surface Enzyme Reactions, Nanoparticles and Diffraction Gratings. *Analyst* **2008,** *133*, 596-601.

15. Lai, Y. J.; Tseng, W. L. Role of 5-Thio-(2-Nitrobenzoic Acid)-Capped Gold Nanoparticles in the Sensing of Chromium(VI): Remover and Sensor. *Analyst* **2011,** *136*, 2712-2717.

16. Sendroiu, I. E.; Gifford, L. K.; Lupták, A.; Corn, R. M. Ultrasensitive DNA Microarray Biosensing via in Situ RNA Transcription-Based Amplification and Nanoparticle-Enhanced SPR Imaging. *J. Am. Chem. Soc.* **2011,** *133*, 4271-4273.

17. Chen, Y.; Xu, Z.; Gartia, M. R.; Whitlock, D.; Lian, Y.; Liu, G. L. Ultrahigh Throughput Silicon Nanomanufacturing by Simultaneous Reactive Ion Synthesis and Etching. *ACS Nano* **2011,** *5*, 8002–8012.

18. Wang, H.-P.; Lin, T.-Y.; Hsu, C.-W.; Tsai, M.-L.; Huang, C.-H.; Wei, W.-R.; Huang, M.-Y.; Chien, Y.-J.;Yang, P.-C.; Liu, C.-W.; Chou, L.-J.; He, J.-H. Realizing High-Efficiency Omnidirectional n-Type Si Solar Cells via the Hierarchical Architecture Concept with Radial Junctions. *ACS Nano* **2013,** *7*, 9325–9335.

19. Jung, J.-Y.; Guo, Z.; Jee, S.-W.; Um, H.-D.; Park, K.-T.; Lee, J.-H. A Strong Antireflective Solar Cell Prepared by Tapering Silicon Nanowires. *Optics Express* **2010,** *18*, A286-A292.

20. Fan, Z. Y.; Kapadia, R.; Leu, P. W.; Zhang, X. B.; Chueh, Y. L.; Takei, K.; Yu, K.; Jamshidi, A.; Rathore, A. A.; Ruebusch, D. J.; Wu, M.; Javey, A. Ordered Arrays of Dual-Diameter Nanopillars for Maximized Optical Absorption. *Nano Lett.* **2010,** *10*, 3823-3827.

21. Zhu, J.; Yu, Z.; Burkhard, G. F.; Hsu, C.-M.; Connor, S. T.; Xu, Y.; Wang, Q.; McGehee, M.; Fan, S.; Cui, Y. Optical Absorption Enhancement in Amorphous Silicon Nanowire and Nanocone Arrays. *Nano Lett.* **2009,** *9*, 279-282.

22. Sorrao, J. L.; Crabtree, G. W. Opportunities and Advances in Mesoscale Science. *Curr Opin Solid State Mater Sci* **2015,** *19*, 227-234.

23. Antonietti, M.; Ozin, G. Promises and Problems of Mesoscale Materials Chemistry or Why Meso? *Chem. Eur. J.* 2004, ***10***, 28-41.

24. Xie, X.; Zhao, W.; Lee, H. R.; Liu, C.; Ye, M.; Xie, W.; Cui, B.; Criddle, C. S.; Cui, Y. Enhancing the Nanomaterial Bio-Interface by Addition of Mesoscale Secondary Features: Crinkling of Carbon Nanotube Films to Create Subcellular Ridges. ***ACS Nano*** 2014, *8*, 11958–11965.

25. Sadakane, M.; Endo, K.; Kodato, K.; Ishikawa, S.; Murayama, T.; Ueda, W. Assembly of a Pentagonal Polyoxomolybdate Building Block, $[Mo_6O_{21}]^{6-}$, into Crystalline MoV Oxides. *Eur. J. Inorg. Chem.* **2013,** 1731–1736.

26. He, Q.; Woo, J.; Belianinov, A.; Guliants, V. V.; Borisevich, A. Y. Better Catalysts Through Microscopy: Mesoscale M1/M2 Intergrowth in Molybdenum–Vanadium Based Complex Oxide Catalysts For Propane Ammoxidation. *ACS Nano* **2015,** *9,* 3470–3478.

27. Saka, S. K.; Honigmann, A.; Eggeling, C.; Hell, S. W.; Lang, T.; Rizzoli, S. O. Multi-Protein Assemblies Underlie the Mesoscale Organization of the Plasma Membrane. *Nat. Commun.* **2014,** *5,* 4509-4522.

28. Chavent, M.; Duncan, A. L.; Rassam, P.; Birkholz, O.; Helie, J.; Reddy, T.; Beliaev, D.; Hambly, B.; Piehler, J.; Kleanthous, C.; Sansom, M. S. P. How Nanoscale Protein Interactions Determine the Mesoscale Dynamic Organisation of Bacterial Outer Membrane Proteins. *Nat. Commun.* **2018,** *9,* 2846-2857.

29. Heyderman, L. J.; David, C.; Klaui, M.; Vaz, C. A. F.; Bland, J. Nanoscale Ferromagnetic Rings Fabricated by Electron-Beam Lithography. *J. Appl. Phys.* **2003,** *93,* 10011–10013.

30. Near, R.; Tabor, C.; Duan, J. S.; Pachter, R.; El-Sayed, M. Pronounced Effects of Anisotropy on Plasmonic Properties of Nanorings Fabricated by Electron Beam Lithography. *Nano Lett.* **2012,** *12,* 2158– 2164.

31. Pearson, D. H.; Tonucci, R. J. Nanochannel Glass Replica Membranes. Science 1995, 270, 68-70.

32. Pearson, D. H.; Tonucci, R. J. Parallel Patterning with Nanochannel Glass Replica Membranes. *Adv. Mater.* **1996,** *8,* 1031–1034.

33. Zhang, G.; Wang, D. Colloidal Lithography – The Art of Nanochemical Patterning. *Chem. – Asian J.* **2009,** *4,* 236-245.

34. Lusker, K. L.; Li, J. R.; Garno, J. C. Nanostructures of Functionalized Gold Nanoparticles Prepared by Particle Lithography with Organosilanes. *Langmuir* **2011,** *27,* 13269-13275.

35. Halpern, A. R.; Corn, R. M. Lithographically Patterned Electrodeposition of Gold, Silver, and Nickel Nanoring Arrays with Widely Tunable Near-Infrared Plasmonic Resonances. *ACS Nano* **2013,** *7,* 1755-1762.

36. Loget, G.; Wood, J. B.; Cho, K.; Halpern, A. R.; Corn, R. M. Electrodeposition of Polydopamine Thin Films for DNA Patterning and Microarrays. *Anal. Chem.* **2013,** *85,* 9991-9995.

37. Cho, K.; Loget, G.; Corn, R. M. Lithographically Patterned Nanoscale Electrodeposition of Plasmonic, Bimetallic, Semiconductor, Magnetic, and Polymer Nanoring Arrays. *J. Phys. Chem. C* **2014,** *118*, 28993–29000.

38. Toma, M.; Loget, G.; Corn, R. M. Fabrication of Broadband Antireflective Plasmonic Gold Nanocone Arrays on Flexible Polymer Films. *Nano Lett.* **2013,** *13*, 6164-6169.

39. Huang, Y.-F.; Chattopadhyay, S.; Jen, Y.-J.; Peng, C.-Y. Anti-Reflecting and Photonic Nanostructures. *Nat. Nanotechnol*. **2007,** *2*, 770-774.

40. Tang, Y.-H.; Huang, M.-J.; Su, J.-Y.; Shiao, M.-H. Fabrication of Nanocone Subwavelength Antireflection Structures on Quartz Substrates. *Jpn. J. Appl. Phys*. **2012,** 51-57.

41. Brunner, R.; Keil, B.; Morhard, C.; Lehr, D.; Draheim, J.; Wallrabe, U.; Spatz, J. Antireflective "Moth-Eye" Structures on Tunable Optical Silicone Membrances. *J. Appl. Opt*. **2012,** *51*, 4370-4376.

42. Garnett, E.; Yang, P. Ordered Arrays of Dual-Diameter Nanopillars for Maximized Optical Absorption. *Nano Lett*. **2010,** *10*, 1082-1087.

43. Tiwari, J. N.; Chen, T.-M.; Pan, F.-M.; Lin, K.-L. Controlled Synthesis and Growth of Perfect Platinum Nanocubes using a Pair of Low-Resistivity Fastened Silicon Wafers and their Electrocatalytic Properties. *J. Power Sources* **2008,** *182*, 510-514.

44. Su, R.; Liu, H.; Kong, T.; Song, Q.; Li, N.; Jin, G.; Cheng, G. Tuning Surface Wettability of InGaN Nanotip Arrays by Phosphonic Acid Modification and Photoillumination. *Langmuir* **2011,** *27*, 13220-13225.

45. Murakoshi, K.; Yanagida, S.; Capel, M.; Castner, E. W. Interfacial Electron Transfer Dynamics of Photosensitized Zinc Oxide Nanoclusters. In Nanostructured Materials, American Chemical Society: 1997; Vol. 679, pp 221-238.

46. Conradt, J.; Sartor, J.; Thiele, C.; Maier-Flaig, F.; Fallert, J.; Kalt, H.; Schneider, R.; Fotouhi, M.; Pfundstein, P.; Zibat, V.; Gerthsen, D. Catalyst-Free Growth of Zinc Oxide Nanorod Arrays on Sputtered Aluminum-Doped Zinc Oxide for Photovoltaic Applications. *J. Phys. Chem. C* **2011,** *115*, 3539-3543.

47. Gonzalez-Valls, I.; Lira-Cantu, M. Vertically-Aligned Nanostructures of ZnO for Excitonic Solar Cells: A Review. *Energy Environ. Sci.* **2009,** *2*, 19-34.

48. Müller, J.; Rech, B.; Springer, J.; Vanecek, M. TCO and Light Trapping in Silicon Thin Film Solar Cells. *Solar Energy* **2004,** *77*, 917-930.

49. Battaglia, C.; Escarré, J.; Söderström, K.; Charrière, M.; Despeisse, M.; Haug, F.-J.; Ballif, C. Nanomoulding of Transparent Zinc Oxide Electrodes for Efficient Light Trapping in Solar Cells. *Nat. Photon.* **2011,** *5*, 535-538.

50. Lin, A.; Phillips, J. Optimization of Random Diffraction Gratings in Thin-Film Solar Cells using Genetic Algorithms. *Sol. Energy Mater Sol. Cells* **2008,** *92*, 1689-1696.

51. Mortimer, R. J.; Rosseinsky, D. R.; Monk, P. M. S. Electrochromic Materials and Devices, 1st ed.; Wiley-VCH Verlag GmbH & Co. KGaA: Berlin, 2015.

52. Mortimer, R. J. Electrochromic Materials. *Annu. Rev. Mater. Res.* **2011**, *41*, 241-268.

53. Somani, P. R.; Radhakrishnan, S. Electrochromic Materials and Devices: Present and Future. *Mater. Chem. Phys.* **2003**, *77*, 117-133.

54. Granqvist, C. G. Electrochromics for Smart Windows: Oxide-Based Thin Films and Devices. *Thin Solid Films* **2014,** *564*, 1-38.

55. Park, C.; Na, J.; Han, M.; Kim, E. Transparent Electrochemical Gratings from a Patterned Bistable Silver Mirror. *ACS Nano* **2017,** *11*, 6977-6984.

56. Aubert, P. H.; Argun, A. A.; Cirpan, A.; Tanner, D. B.; Reynolds, J. R. Microporous Patterned Electrodes for Color-Matched Electrochromic Polymer Displays. *Chem. Mater.* **2004,** *16*, 2386–2393.

57. Xu, W.; Fu, K.; Ma, C.; Bohn, P. W. Closed Bipolar Electrode-Enabled Dual-Cell Electrochromic Detectors for Chemical Sensing. *Analyst* **2016,** *141*, 6018–6024.

58. *Xu, W.; Fu, K.; Bohn, P. W. Electrochromic Sensor for Multiplex Detection of Metabolites Enabled by Closed Bipolar Electrode Coupling. ACS Sens.* **2017,** *2*, 1020-1026.

59. Kirchmeyer, S.; Elschner, A.; Reuter, K.; Lovenich, W.; Merker, U. *PEDOT: Principles and Applications of an Intrinsically Conductive Polymer*; Eds.; CRC Press, 2010.

60. Sankaran, B.; Reynolds, J. R. High-Contrast Electrochromic Polymers from Alkyl-Derivatized Poly(3,4-ethylenedioxythiophenes). *Macromolecules* **1997,** *30*, 2582-2588.

61. Kumar, A.; Welsh, D. M.; Morvant, M. C.; Piroux, F.; Abboud, K. A.; Reynolds, J. R. Conducting Poly(3,4-alkylenedioxythiophene) Derivatives as Fast Electrochromics with High-Contrast Ratios. *Chem. Mater.* **1998,** *10*, 896-902.

62. Ruffo, R.; Celik-Cochet, A.; Posset, U.; Mari, C. M.; Schottner, G. Mechanistic Study of the Redox Process of an *In Situ* Oxidatively Polymerised Poly(3,4-ethylene-dioxythiophene) Film. *Sol. Energy Mater. Sol. Cells* **2008,** *92*, 140-145.

63. Cai, G.; Cui, M.; Kumar, V.; Darmawan, P.; Wang, J.; Wang, X.; Lee-Sie Eh, A.; Qian, K.; Lee, P. S. Ultra-Large Optical Modulation of Electrochromic Porous WO_3 Film and the Local Monitoring of Redox Activity. *Chem Sci.* **2016,** *7*, 1373-1382.

64. Wang, Y.; Runnerstrom, E. L.; Milliron, D. J. Switchable Materials for Smart Windows. *Annu. Rev. Chem. Biomol. Eng.* **2016,** *7*, 283-304.

65. Abe, O. O.; Jodhani, G.; Gouma, P. On the Coupled Ferroelectric-Electrochromic Effect of ε-WO_3. *J. Am. Ceram Soc.* **2018,** *101*, 12–15.

66. Meulenkamp, E. A. Mechanism of WO_3 Electrodeposition from Peroxy-Tungstate Solution. *J. Electrochem. Soc.* **1997,** *144*, 1664-1671.

67. Randriamahazaka, H.; Sini, G.; Tran Van, F. Electrodeposition Mechanisms and Electrochemical Behavior of Poly(3,4-ethylenedithiathiophene). *J. Phys. Chem. C* **2007,** *111*, 4553-4560.

68. Illy, B. N.; Cruickshank, A. C.; Schumann, S.; Da Campo, R.; Jones, T. S.; Heutz, S.; McLachlan, M. A.; McComb, D. W.; Riley, D. J.; Ryan, M. P. Electrodeposition of ZnO Layers for Photovoltaic Applications: Controlling Film Thickness and Orientation. *J. Mater. Chem.* **2011,** *21*, 12949-12957.

Chapter 2

Fabrication of PEDOT Nanocone Arrays with Electrochemically Modulated Broadband Antireflective Properties

2.1 Introduction

Periodic nanocone arrays are unique nanostructured surfaces with very useful antireflective and hydrophobic properties that have been incorporated into both natural systems, such as moths' eyes and lotus leaves,[1–3] and also modern technological devices, such as solar cells and self-cleaning windows.[4–6] Recently, we have developed a very simple method for fabricating polymeric two-dimensional hexagonal nanocone arrays over large areas (square cm) by the simultaneous oxygen plasma etching of a colloidal monolayer of polystyrene (PS) beads and an underlying polymer substrate. For the case of flexible fluorinated ethylene propylene (FEP) substrates, we fabricated FEP nanocone arrays and then coated them with a 50 nm gold thin film to create a plasmonic nanocone surface that was highly antireflective[7] and also

exhibited tunable superhydrophobic properties.[8] In this paper, we demonstrate that our nanocone array fabrication strategy can be used to create nanocone arrays from thin films of the electroactive polymer poly(3,4-ethylenedioxythiophene) (PEDOT). Thin PEDOT films have been studied extensively for their transmissive electrochromic properties;[9–13] we show here that PEDOT nanocone arrays formed by the oxygen plasma etching of an electrodeposited PEDOT thin film coated with a hexagonally closed packed (hcp) PS bead monolayer exhibit excellent broadband antireflectivity. Moreover, the oxidation state of the PEDOT nanocone array film can be modulated electrochemically and remains fixed when removed under potentiostatic control. Both the absorption spectrum and reflectivity spectrum are found to vary with film oxidation state, but each in a different manner due to different optical effects. Changes in the reflectivity spectrum of the PEDOT nanocone arrays with oxidation state were completely opposite to those observed from unmodified PEDOT thin films; this difference is attributed to the unique dependence of the PEDOT nanocone array reflectivity on the complex interfacial refractive index.

2.2 Experimental Section

2.2.1 Fabrication of PEDOT Thin Film

The fluorine-doped tin oxide coated glass (FTO-glass; ~7 Ω/sq, Sigma-Aldrich) was degreased by sonication in deionized water, acetone and methanol and then dried with a nitrogen jet. Additionally, FTO glass was treated by oxygen plasma cleaning (PDC-32G, Harrick Plasma) for 3min. Poly(3,4-ethylenedioxythiophene)-poly(styrenesulfonate) (PEDOT:PSS, 1.0 wt. % in H_2O, Sigma-Aldrich) was mixed with isopropyl alcohol and ethylene glycol (ratio 85:10:5) to enhance electronic conductivity and improve wetting.[1,2] Uniform and thin PEDOT:PSS layer was

coated on FTO by spincoating at 3000 rpm for 20 s. The sample was dried for 30 min on a hot plate at 130°C. Chronoamperometry was used to electrodeposit PEDOT films on the PEDOT:PSS coated FTO surface. The PEDOT electrodeposition were performed with a potentiostat (Autolab) at a constant potential of +1.0 V for 75 s to make 450 nm thick film with a Pt counter electrode, a Ag/AgCl reference electrode, and an aqueous electrolyte consisted with 0.02 M 3,4-ethylenedioxythiophene (EDOT, 97%, Sigma-Aldrich), 0.1M sodium dodecyl sulfate (SDS) and 0.1 M lithium perchlorate ($LiClO_4$, 99.5%, Alfa).

2.2.2 Fabrication of PEDOT Nanocone Arrays

A solution of polystyrene beads with a diameter of 0.2 μm (Polybead carboxylate, 2.6 w/v %, Polyscience) were centrifuged and transferred to a mixture containing ethanol and methanol with a 2:1 ration. Surfactant Triton X-100 (TX100, Fischer Scientific) was added to the solution at 7.5 mM. The concentration of PS beads was adjusted to about 5 w/v %. The PS beads were spincoated on PEDOT thin film with 650 rpm for 20 s, and allowed to dry at dried at room temperature. The PEDOT film with PS beads sample was etched by oxygen plasma (50W, 200mTorr, South Bay Technology) for 1 min 30 s. To remove any remaining PS beads, the sample was cleaned with tetrahydrofuran (THF, EMD) for 2h.

2.2.3 Characterization

For morphological characterization, a field-emission scanning electron microscope (FEI Magellan 400) was used. For UV-Vis measurements, a Hewlett Packard 8453 UV-Visible spectrophotometer was used. For reflectivity measurements, a halogen lamp was used as a white light source (7 V, DC regulated power supply, BK Presicion). The emitted light from a halogen light was coupled into an optical fiber (M25L01, Thorlabs), collimated with an achromatic lens (f = 50 mm, AC254-050-A-ML, Thorlabs), then aligned incident to the sample surface. The

reflected or transmitted light was coupled into an optical fiber (P1000-2-VIS/NIR, Ocean Optics) with an achromatic lens (f = 30 mm, AC254-030-A-ML, Thorlabs), then characterized with a UV-Vis spectrometer (USB4000, Ocean Optics). To measure the *ex situ* UV-vis spectra and reflectivity spectra, the samples applied potential for 20 seconds before removing the film from solution.

2.3 Results and Discussion

2.3.1 Fabrication of PEDOT Nanocone Array Surfaces

PEDOT nanocone arrays were fabricated from the simultaneous oxygen plasma etching of electrodeposited PEDOT thin films coated with a hcp PS bead monolayer. The formation of a PEDOT thin film through the electropolymerization and electrodeposition of 3,4-ethylenedioxythiophene (EDOT) has been demonstrated previously for films up to 300 nm in thickness.[12,14–16] To create stable thick PEDOT films, we developed a slightly modified electrodeposition process in which a very thin PEDOT:PSS layer was first spincoated onto a transparent FTO conductive substrate prior to the EDOT electropolymerizaton. The thickness of the electrodeposited PEDOT thin films was controlled by the electrodeposition time and set to a value of 450 nm as measured by SEM. (A plot of electrodeposition current density vs. time and the PEDOT film thickness are shown in Supporting Information in Appendix A.) A PS bead monolayer was then deposited onto the PEDOT thin film by spincoating in an ethanolic solution. As shown in the scheme in Figure 2.1, exposure of this surface to oxygen plasma etching created the PEDOT nanocone array. The PS bead monolayer initially protects the PEDOT thin film, but as the plasma etching constantly reduces the bead size, the amount of protected surface constantly decreases as the nanocone array is formed. The spacing of the nanocones within the

array is controlled by the original PS bead diameter, and the height of the nanocones is controlled by both the size of the PS beads and the thickness of the electrodeposited PEDOT thin film, as well as the differential bead/film etching rate. Two SEM images of a typical PEDOT nanocone array surface are shown in Figures 2.1b and 2.1c. The nanocones in this array were formed by 90 s of oxygen plasma etching of a 450 nm PEDOT thin film coated with a hcp monolayer of 200 nm diameter PS beads. The resultant nanocone array had an average height of 350 nm, and a small amount of residual PS can be seen on the nanocones in Figure 2.1c. To ensure removal of this residual PS, the films were thoroughly rinsed with tetrahydrofuran after etching.

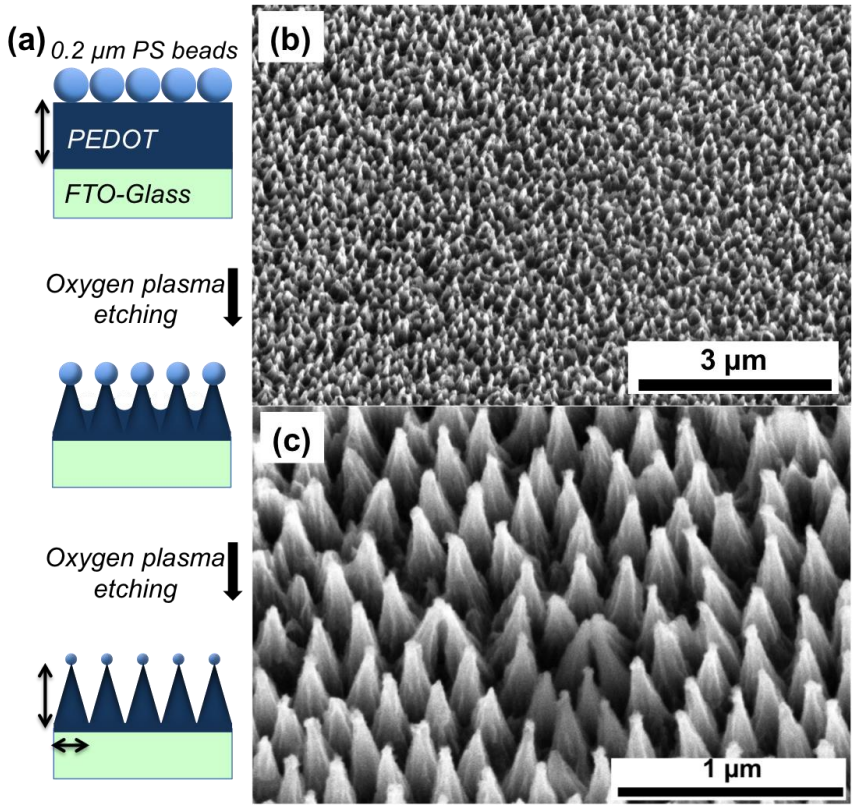

Figure 2.1. (a) Schematic diagram for the fabrication of PEDOT nanocone arrays (height: 350 nm, spacing: 200 nm) by oxygen plasma etching of a 450 nm electrodeposited PEDOT film on FTO glass coated with a 200 nm hcp PS bead monolayer. (b) SEM image of PEDOT nanocone arrays with low magnification and (c) detailed SEM image of PEDOT nanocones with high magnification and a tilted view.

2.3.2 Antireflective Nature of PEDOT Nanocone Array Surfaces

The PEDOT nanocone array surfaces created by this plasma etching process exhibited a very low reflectivity over a wide wavelength range. The reflectivity spectrum of the PEDOT nanocone array at a nearly normal incident angle of 8° is shown in Figure 2.2 (blue spectrum).

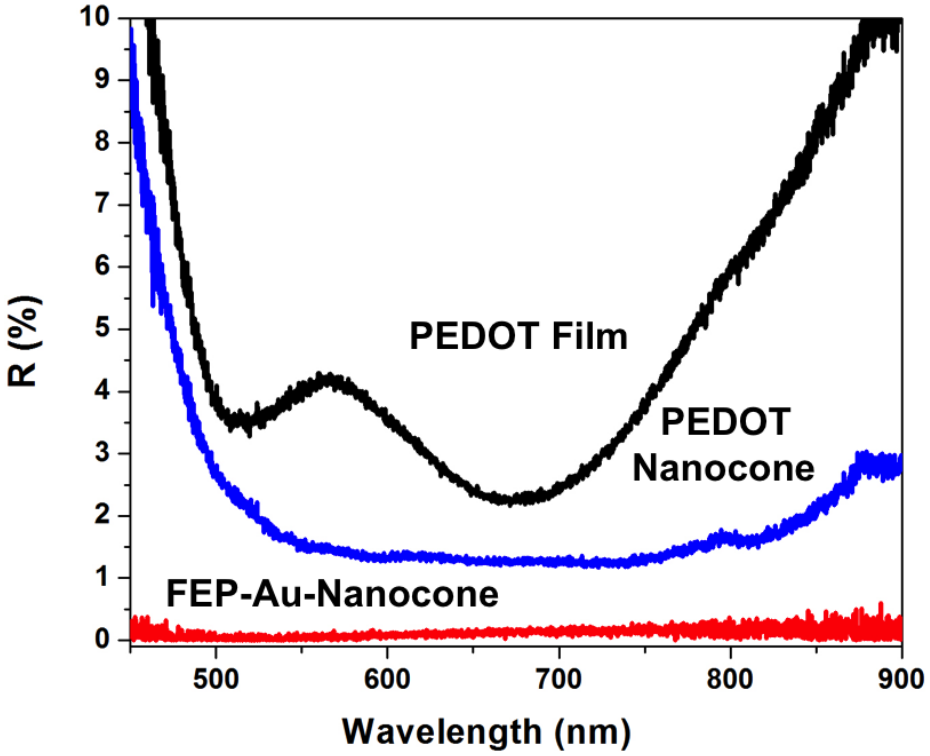

Figure 2.2. Reflectivity spectra at an incidence angle of 8° for a PEDOT nanocone array film (blue spectrum), an unmodified PEDOT thin film (black spectrum) and a plasmonic gold nanocone array thin film (red spectrum). The FEP-Au-nanocone array film was fabricated as described in Ref. 7.

The PEDOT nanocone array reflectivity is relatively featureless and less than 1.5%R over the entire wavelength range of 550 nm to 800 nm. For comparison, the reflectivity spectrum of an unmodified 450 nm thick electrodeposited PEDOT film (black spectrum) is also shown in Figure 2.2. In addition, similar reflectivity spectra were also observed at higher incident angles, as shown by reflectivity spectra obtained at incident angles of 45° and 67.5° in Figure 2.3.

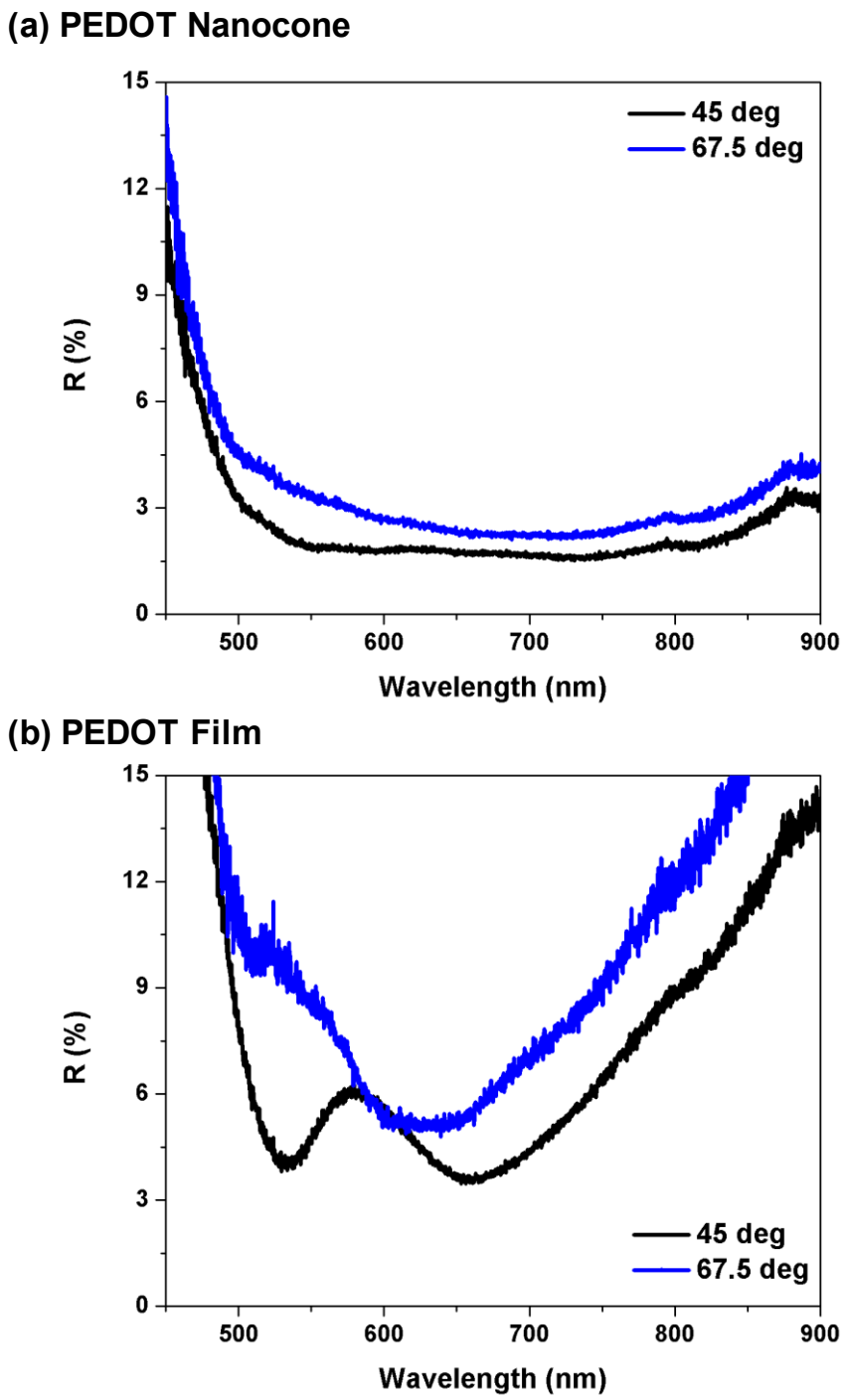

Figure 2.3. Reflectivity spectrum at an incidence angle of 45° (black spectrum) and 67.5° (blue spectrum) for a (a) PEDOT nanocone array film and (b) an unmodified PEDOT film.

The PEDOT nanocone array surface had lower percent reflectivity values at all wavelengths throughout the visible and near infrared for all incident angles as compared to the unmodified PEDOT thin film spectrum, and most noticeably did not show the strong reflectivity increase feature at 570 nm that was observed for the unmodified film. Additionally, a plasmonic gold-coated FEP nanocone array (red spectrum)[7] is also shown in the Figure. We deduce that the mechanism for the broadband antireflectivity of the PEDOT nanocones is the same as in the case of the plasmonic gold nanocone arrays, although as can be seen in the Figure the PEDOT nanocone arrays are not as antireflective as the gold-coated FEP nanocones. Silicon nanocone array surfaces described previously by other authors also show similar broadband antireflection properties.[17–19] The reflectivity of nanocone array surfaces has been modeled previously as a combination of graded refractive index and enhanced thin film absorption.[17,20,21] The higher aspect ratio of the gold-coated FEP nanocone arrays and their better absorptive properties are the two reasons why the antireflectivity is better for those surfaces.[7]

2.3.3 Electrochromism of PEDOT Nanocone Array Surfaces

Like all other previous studies of electrodeposited PEDOT thin films, the PEDOT nanocone array films were found to exhibit reversible electrochromism due to the modulation of the PEDOT film oxidation state with electrode potential in a $LiClO_4$ solution.[12,22] In addition to observing the *in situ* PEDOT electrochromic behavior in an electrochemical cell, the PEDOT films could be removed from solution under potentiostatic control to examine both their absorption spectrum and antireflective properties in air. Figure 2.4 plots the absorption spectra of the PEDOT nanocone arrays after removal from solution at three different potentials: +1.0 V, 0.0 V and −1.0 V vs. Ag/AgCl (all potentials were held for 20 s before removal from solution). As

shown previously by other researchers, the electrochromic behavior of PEDOT arises from changes in the electrochemical doping of the thin film, with the more reduced state (−1.0 V) being highly colored and the more oxidized state (+1.0 V) being less absorptive.[9,13,16] This can be seen both in the *ex situ* absorption spectra as well as in the two photographs of the PEDOT nanocone array film at +1.0 V and −1.0 V that are also shown in Figure 2.4. These spectra are qualitatively similar to spectra obtained from an unmodified PEDOT thin film removed at the same potentials (see Supporting Information in Appendix A).

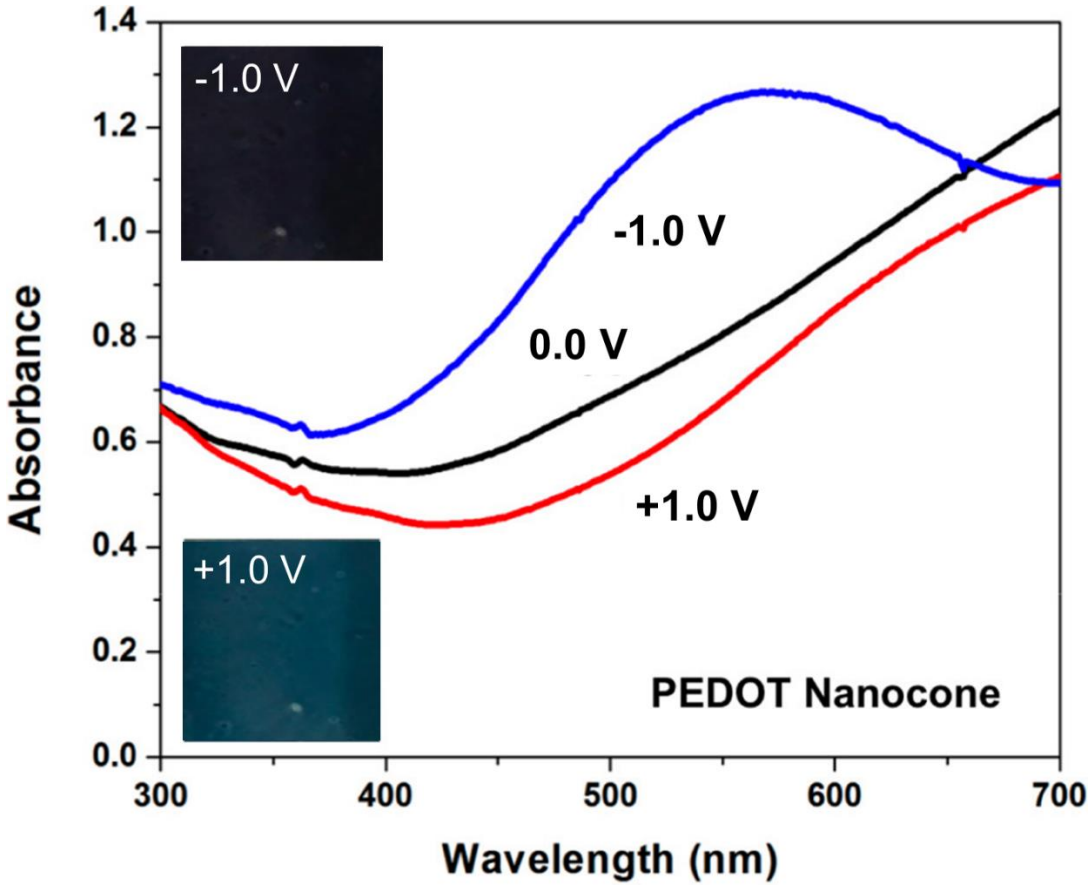

Figure 2.4. *Ex situ* UV absorption spectra of PEDOT nanocone arrays (inset: photographs at oxidized and reduced state) at three applied potentials vs. Ag/AgCl: -1.0 V (blue), 0.0 V (black) and +1.0 V (red).

2.3.4 Electrochemically Modulated Reflectivity of PEDOT Nanocone Array Surfaces

In contrast, the variations in the *ex situ* reflectivity spectra for PEDOT nanocone arrays removed at different electrode potentials were surprisingly different as compared to unmodified PEDOT thin film surfaces. Figures 2.5a and 2.5b show reflectivity spectra from a PEDOT nanocone array and an unmodified PEDOT thin film respectively after being removed from solution at the same three applied potentials as in Figure 2.4 (−1.0 V, 0.0 V and +1.0 V). The most dramatic differences are between spectra taken at −1.0 V to +1.0 V, where the reflectivity has significantly increased at all wavelengths for the PEDOT nanocone array film, but has decreased for the unmodified PEDOT thin film. The largest effect occurs at approximately 650 nm, where the PEDOT nanocone array reflectivity increases five-fold (from 0.67%R up to 4.14%R) whereas the unmodified PEDOT thin film reflectivity decreases four-fold (from 7.6%R down to 2.0%R). The featureless reflectivity spectrum of the PEDOT nanocone array in Figure 2.5a does not change significantly at the three different applied potentials, whereas there are significant band shifts in the spectrum of the unmodified PEDOT thin film in Figure 2.5b.

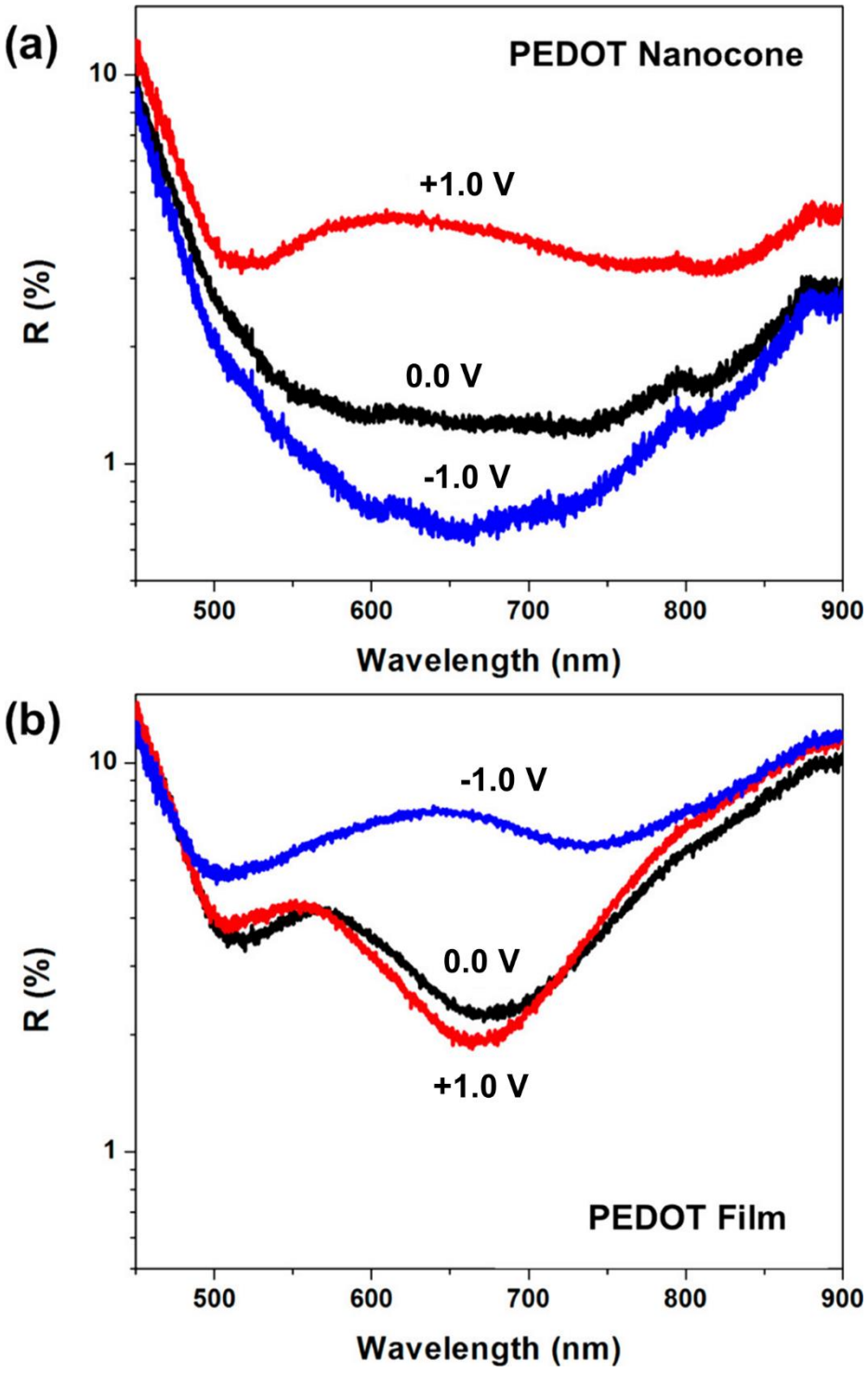

Figure 2.5. Electrochemically modulated reflectivity spectra for (a) PEDOT nanocone arrays and (b) unmodified PEDOT thin films which were removed from solution after 20 s at three different applied potentials: -1.0 V (blue spectrum), 0.0 V (black spectrum) and +1.0 V (red spectrum). The angle of incidence for the reflectivity spectra was 8°.

Additionally, when comparing changes in the reflectivity spectra from films removed at 0.0 V and +1.0 V, a proportional increase in the reflectivity spectrum was observed for the PEDOT nanocone array, whereas only relatively small reflectivity changes were observed for the unmodified PEDOT thin film. It is clear from the spectra in Figure 2.5 that the optical mechanism for the broadband electroreflectivity observed from the PEDOT nanocone array film must be very different to the mechanism for the electroreflectivity observed from the unmodified PEDOT film. To try to understand this effect, we performed three phase Fresnel reflectivity calculations (air/film/substrate, n1/n2/n3), as described in Figure 2.6, to show that an increase in film absorption (as modeled by an increase in the imaginary component of the film RI, n2 = 1.5 + x i, where x goes from 0 to 0.5) leads to a higher specular reflectivity at all angles.

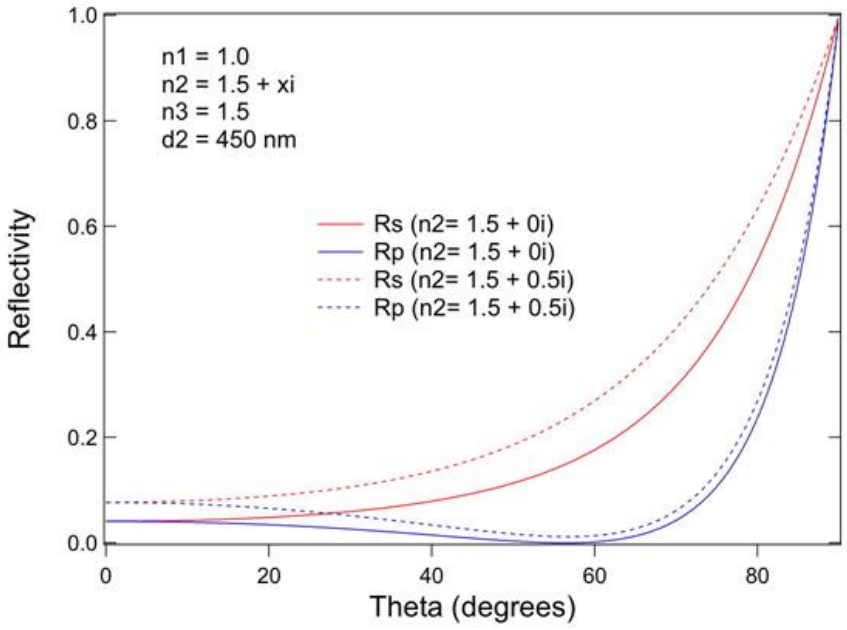

Figure 2.6. Three phase Fresnel reflectivity calculation (air; n1=1/film; n2=1.5+xi/substrate; n3=1.5) and plot of Reflectivity vs. theta (incident angle). An increase in PEDOT film absorption as modeled by an increase in the imaginary component of the film RI from zero to 0.5 leads to a higher specular reflectivity at all incident angles.

This is what we observed for the unmodified PEDOT films. In contrast, the PEDOT nanocone films showed the opposite behavior: an increase in nanocone absorptivity actually resulted in a decrease in the specular reflectivity. This effect has been observed previously in both the gold plasmonic nanocone arrays[7] and in silicon nanocone array surfaces.[17–19] The presence of highly absorbing nanocones on the surface results in a combination of multiple internal reflection, absorption and scattering processes that lead to a reduced reflectivity at all incident angles.

2.4 Conclusions

In summary, we have demonstrated that the fabrication process used previously to create gold plasmonic nanocone arrays also can be used with thin films of the electroactive polymer PEDOT to create electroreflective nanocone arrays over large areas. The PEDOT nanocone array surfaces exhibited a good broadband antireflectivity throughout the visible and near infrared wavelength regions due to the graded interfacial complex refractive index created by the PEDOT nanocones. Additionally, the broadband antireflectivity of the nanocone array surface could be controlled by the electrochemical modulation of the oxidation state of the PEDOT nanocones. The changes observed in the *ex situ* reflectivity spectra of the PEDOT nanocone arrays with oxidation state were opposite to those observed from unmodified PEDOT thin films; we attribute this marked difference to the unique optical behavior (a combination of broadband reflection, scattering and absorption) of the air-nanocone array interface for the case where the nanocone complex refractive index has a significant imaginary component. In this work, the electroreflectivity of the PEDOT nanocone arrays was probed with *ex situ* spectra; in future work we will further characterize the reversible *in situ* electroreflective behavior with real-time reflectivity measurements. The antireflective and electrochromic PEDOT semiconductor

nanocone array films described here should find applications in solar energy cells, optical sensors, and optical devices.

2.5 Acknowledgments

This work was supported by the National Science Foundation through grant CHE-1403506. SEM analysis were performed at the Irvine Materials Research Institute (IMRI) at UC Irvine.

2.6 References

1. Celia, E.; Darmanin, T.; Taffin de Givenchy, E.; Amigoni, S.; Guittard, F. Recent Advances in Designing Superhydrophobic Surfaces. *J. Colloid Interface Sci.* **2013**, *402*, 1–18.

2. Raut, H. K.; Ganesh, V. A.; Nair, A. S.; Ramakrishna, S. Anti-Reflective Coatings: A Critical, in-Depth Review. *Energy Environ. Sci.* **2011**, *4*, 3779-3804.

3. Clapham, P. B.; Hutley, M. C. Reduction of Lens Reflexion by the "Moth Eye" Principle. *Nature* **1973**, *244*, 281–282.

4. Tsui, K.; Lin, Q.; Chou, H.; Zhang, Q.; Fu, H.; Qi, P. Low-Cost, Flexible, and Self-Cleaning 3D Nanocone Anti-Reflection Films for High-Efficiency Photovoltaics. *Adv. Mater.* **2014**, *26*, 2805–2811.

5. Leem, J. W.; Kim, S.; Lee, S. H.; Rogers, J. A.; Kim, E.; Yu, J. S. Efficiency Enhancement of Organic Solar Cells Using Hydrophobic Antireflective Inverted Moth-Eye Nanopatterned PDMS Films. *Adv. Energy Mater.* **2014**, *4*, 1–7.

6. Wang, Y.; Lu, N.; Xu, H.; Shi, G.; Xu, M.; Lin, X.; Li, H.; Wang, W.; Qi, D.; Lu, Y.; Chi, L. Biomimetic Corrugated Silicon Nanocone Arrays for Self-Cleaning Antireflection Coatings. *Nano Res.* **2010**, *3*, 520–527.

7. Toma, M.; Loget, G.; Corn, R. M. Fabrication of Broadband Antireflective Plasmonic Gold Nanocone Arrays on Flexible Polymer Films. *Nano Lett.* **2013**, *13*, 6164–6169.

8. Toma, M.; Loget, G.; Corn, R. M. Flexible Teflon Nanocone Array Surfaces with Tunable Superhydrophobicity for Self-Cleaning and Aqueous Droplet Patterning. *ACS Appl. Mater. Interfaces* **2014**, *6*, 11110–11117.

9. Kirchmeyer, S.; Elschner, A.; Reuter, K.; Lovenich, W.; Merker, U.; Editors. *PEDOT: Principles and Applications of an Intrinsically Conductive Polymer.*; CRC Press, ***2010***.

10. Sankaran, B.; Reynolds, J. R. High-Contrast Electrochromic Polymers from Alkyl-Derivatized Poly(3,4-Ethylenedioxythiophenes). *Macromolecules* **1997**, *30*, 2582–2588.

11. Mortimer, R. J. Organic Electrochromic Materials. *Electrochim. Acta* **1999**, *44*, 2971–2981.

12. Kumar, A.; Welsh, D. M.; Morvant, M. C.; Piroux, F.; Abboud, K. a.; Reynolds, J. R. Conducting Poly(3,4-Alkylenedioxythiophene) Derivatives as Fast Electrochromics with High-Contrast Ratios. *Chem. Mater.* **1998**, *10*, 896–902.

13. Ruffo, R.; Celik-Cochet, A.; Posset, U.; Mari, C. M.; Schottner, G. Mechanistic Study of the Redox Process of an in Situ Oxidatively Polymerised poly(3,4-Ethylene-Dioxythiophene) Film. *Sol. Energy Mater. Sol. Cells* **2008**, *92*, 140–145.

14. Diderot, P. D.; Brosse, D.; Sini, G.; Van, F. T. Electrodeposition Mechanisms and Electrochemical Behavior of Poly (3 , 4-Ethylenedithiathiophene). *J. Phys. Chem. C* **2007**, *111*, 4553–4560.

15. Nguyen, V. Q.; Schaming, D.; Martin, P.; Lacroix, J. C. Highly Resolved Nanostructured PEDOT on Large Areas by Nanosphere Lithography and Electrodeposition. *ACS Appl. Mater. Interfaces* **2015**, *7*, 21673–21681.

16. Deutschmann, T.; Oesterschulze, E. Micro-Structured Electrochromic Device Based on Poly(3,4-Ethylenedioxythiophene). *J. Micromech. Microeng.* **2013**, *23*, 65032.

17. Zhu, J.; Yu, Z.; Burkhard, G. F.; Hsu, C.-M.; Connor, S. T.; Xu, Y.; Wang, Q.; McGehee, M.; Fan, S.; Cui, Y. Optical Absorption Enhancement in Amorphous Silicon Nanowire and Nanocone Arrays. *Nano Lett.* **2009**, *9*, 279–282.

18. Wang, K. X.; Yu, Z.; Liu, V.; Cui, Y.; Fan, S. Absorption Enhancement in Ultrathin Crystalline Silicon Solar Cells with Antireflection and Light-Trapping Nanocone Gratings. *Nano Lett.* **2012**, *12*, 1616–1619.

19. Jeong, S.; Garnett, E. C.; Wang, S.; Yu, Z.; Fan, S.; Brongersma, M. L.; McGehee, M. D.; Cui, Y. Hybrid Silicon Nanocone-Polymer Solar Cells. *Nano Lett.* **2012**, *12*, 2971–2976.

20. Brongersma, M. L.; Cui, Y.; Fan, S. Light Management for Photovoltaics Using High-Index Nanostructures. *Nat. Mater.* **2014**, *13*, 451–460.

21. Wang, Z. Y.; Zhang, R. J.; Wang, S. Y.; Lu, M.; Chen, X.; Zheng, Y. X.; Chen, L. Y.; Ye, Z.; Wang, C. Z.; Ho, K. M. Broadband Optical Absorption by Tunable Mie Resonances in Silicon Nanocone Arrays. *Sci. Rep.* **2015**, 1–6.

22. Aubert, P. H.; Argun, A. A.; Cirpan, A.; Tanner, D. B.; Reynolds, J. R. Microporous Patterned Electrodes for Color-Matched Electrochromic Polymer Displays. *Chem. Mater.* **2004**, *16*, 2386–2393.

Chapter 3

Ultra-Antireflective Electrodeposited Plasmonic and PEDOT Nanocone Array Surfaces

3.1 Introduction

Nanostructured array surfaces can provide excellent broadband antireflectivity over a wide range of optical wavelengths and incident angles, and have been incorporated as optical coatings into various devices such as solar cells,[1,2] photodetectors,[3] and electroreflective windows.[4] Traditionally, arrays of transparent zinc oxide nanostructures have been fabricated by chemical vapor deposition[5-7] or electrochemical methods[8-11] to create a graded interfacial refractive index coating that increases the transmittance of silicon solar cell devices by reducing the reflectivity of the device surface down to approximately 2-5%.[12-14] However, when a transparent nanostructured ZnO coating is used in a hierarchical fashion with a subwavelength periodic array of an absorbing material,[15,16] an even better broadband antireflective surface can

be created. Recently, we have demonstrated the fabrication of periodic absorptive nanocone arrays of gold-coated fluorinated ethylene propylene (FEP)[17] and the electroactive polymer poly(3,4-ethylenedioxythiophene) (PEDOT);[18] our large area fabrication process employs the oxygen plasma etching of a square centimeter scale polymer substrate or thin film that has been covered with a colloidal monolayer of polystyrene (PS) beads. The resultant plasmonic gold and PEDOT nanocone array surfaces both exhibited excellent broadband antireflectivity; for the gold surfaces a reflectivity of less than 1% was observed from 475 nm to 800 nm over a wide range of incident angles.[17] In this paper, we show that the reflectivity for both the gold and PEDOT nanocone arrays can be reduced even further by the electrodeposition of a nanostructured ZnO coating; for the PEDOT nanocone arrays, up to a 10-fold reduction in reflectivity is observed with the surface being 0.1% to 0.2% reflective from 475 nm to 800 nm while transmitting from 2% to 10% in the same spectral region. In addition, we demonstrate that the antireflective nature of the ZnO-coated nanocone arrays can be explained using 11-phase Fresnel calculations to model the graded refractive index and absorption changes at the air/nanocone interface. To the best of our knowledge, no one has fabricated surfaces with lower reflectivities than our broadband ultra-antireflective ZnO nanostructured surfaces. The ultra-antireflective ZnO-coated nanocone array surfaces are characterized with SEM, XRD, and XPS, and additionally are shown to be photocatalytic with potential as self-cleaning surfaces. Moreover, the PEDOT nanocone arrays are electro-reflective and thus can be incorporated into electro-optical devices.[18] These ultra-antireflective surfaces are extremely useful in applications where reflections must be absolutely minimized; examples include laser optics[19,20] and anti-glare coatings for mirrors displays, cameras, and lenses.[21,22]

3.2 Experimental Section

3.2.1 Fabrication of FEP-Au Nanocone Array Surfaces

A FEP substrate with a 0.005″ thickness (CS Hyde Company) was cleaned by rinsing with ethanol and MilliQ water followed by O_2 plasma cleaning (PDC-32G, Harrick Plasma) for 3 minutes. A solution of PS beads with a diameter of 1 μm (Polyscience Polybead® carboxylate, 2.6% w/v) was centrifuged and transferred to a mixture containing ethanol and methanol in a 2:1 ratio with 0.2% volume Triton X-100 surfactant, adjusted to a PS concentration of about 5%. To form the PS colloidal mask monolayer, the PS beads were spincoated onto the FEP substrate at 650 rpm for 15 seconds, and left at room temperature for a few minutes to dry the solvent. The PS bead/FEP substrate was then etched by O_2 plasma for 6 minutes to form periodic FEP nanocone arrays. The FEP nanocone arrays were finally coated with 50 nm of gold by thermal evaporation.

3.2.2 Fabrication of PEDOT Thin Film

A fluorine-doped tin oxide coated glass slide substrate (FTO glass; ~30 Ω/sq, Sigma-Aldrich) was cleaned by sonication in a 0.2% volume aqueous TX-100 solution, followed by sonication in ethanol, then dried under a nitrogen stream, and finally cleaned by O_2 plasma cleaning (PDC-32G, Harrick Plasma) for 3 minutes. A layer of PEDOT:PSS (2.0 wt % in H_2O, high conductivity grade, Sigma-Aldrich) was spincoated at 2000 rpm for 45 seconds onto the FTO substrate to improve wetting and conductivity. The sample was dried for 20 minutes in a 90°C oven. PEDOT thin film was then deposited electrochemically onto the FTO substrate using an aqueous plating solution consisting of 2.5 mM EDOT (97%, Sigma-Aldrich) and 12.5 mM $LiClO_4$ (99.5%, Alfa) via cyclic voltammetry. The electrodeposition was performed using a

potentiostat (Metrohm Autolab PGSTAT12) sweeping from +1.045 V to +0.9 V at 0.01 V/s for 10 cycles, with a Ag/AgCl reference electrode and a Pt counter electrode.

3.2.3 Fabrication of PEDOT Nanocone Array Surfaces

A solution of PS beads with a diameter of 1 μm (Polyscience Polybead® carboxylate, 2.6% w/v) was centrifuged and transferred to a mixture containing ethanol and methanol in a 2:1 ratio with 0.2% volume TX-100 surfactant, adjusted to a PS concentration of about 5%. To form the PS colloidal mask monolayer, the PS beads were spincoated onto the PEDOT film at 750 rpm for 15 seconds, and left at room temperature for a few minutes to dry the solvent. The PS bead/PEDOT sample was then etched by O_2 plasma for 2.5 minutes to form periodic PEDOT nanocone arrays.

3.2.4 Fabrication of ZnO-Coated Nanocone Array Surfaces

An aqueous solution of 0.1 M $Zn(NO_3)_2 \cdot 6H_2O$ (98%, Sigma-Aldrich) at pH 4 heated to 70°C was used as the plating solution. Electrodeposition was performed using a potentiostat (PGSTAT12, Metrohm) in a 3-electrode setup. The working electrode of either Au or PEDOT nanocone array surfaces was exposed to the plating solution for 150 seconds at an anodic potential of −0.9 V against a Ag/AgCl reference electrode and in the presence of a Pt counter electrode.

3.2.5 Characterization

SEM images were obtained on a FEI Magellan 400 field-emission scanning electron microscope at an accelerating voltage of 5 kV. Grazing incidence XRD measurements were performed on a Rigaku SmartLab X-ray Diffractometer, with the X-ray generator operating at 40 kV and 44 mA with Cu Kα irradiation. XPS measurements were performed using a Kratos Analytical AXIS Supra surface analysis instrument at an emission current of 15 mA. For

reflectivity and transmittance measurements, a halogen lamp was used as a white light source (10 V, B&K Precision DC regulated power supply). The emitted white light was coupled to an optical fiber (Thorlabs M25L01), collimated using an achromatic lens (f = 50 mm, Thorlabs AC254-050-A-ML), then made incident to the sample surface. The reflected or transmitted light from the sample surface is coupled to an optical fiber (Ocean Optics P1000-2-VIS/NIR) with an achromatic lens (f = 30 mm, Thorlabs AC254-030-A-ML), then measured with a UV-Vis-NIR spectrometer (Ocean Optics USB4000). Reflectivity measurements were calibrated with a silver mirror reference, whereas transmittance measurements were calibrated using air as reference.

3.2.6 Photocatalytic Degradation of Methylene Blue

1 mL of a 50 μM aqueous methylene blue (MB) solution and a 1 square cm photocatalytic surface (either ZnO-coated nanocone arrays or planar ZnO thin film) were added in a quartz cuvette. The cuvette was exposed to a UV lamp source (50 W, Oriel Instruments Hg(Xe) arc lamp) while stirring to ensure contact between the ZnO surface and the MB. The relative concentration of MB remaining was determined after the following time intervals: 0, 2, 4, 6, 8, 10, 12, and 14 minutes. Relative MB concentrations were determined from the absorbance measurement at $\lambda = 664$ nm using UV-Vis spectroscopy (Hewlett Packard 8453 UV-Visible spectrometer).

3.3 Results and Discussion

3.3.1 Fabrication of ZnO-Coated Nanocone Array Surfaces

Large scale periodic ZnO-coated nanocone array surfaces (areas on the order of square cm) were fabricated using a combination of colloidal lithography, plasma etching, vapor deposition, and electrochemistry. As shown in the scheme in Figure 3.1, the simultaneous

oxygen plasma etching of a hexagonally closed packed monolayer of PS bead colloidal mask spincoated onto either a FEP substrate or a PEDOT thin film created periodic nanocone arrays; nanocone formation occurs due to the simultaneous etching of both the PS colloidal mask and the polymer underneath.

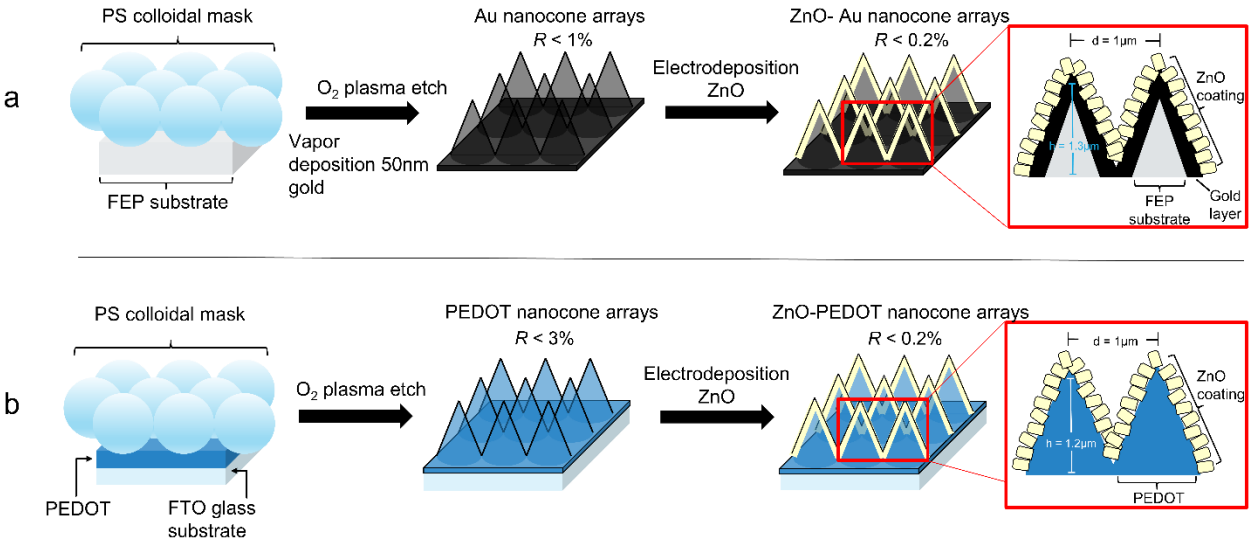

Figure 3.1. Schematic illustration of the fabrication of ultra-antireflective ZnO-coated nanocone arrays using (a) FEP-Au nanocone arrays and (b) PEDOT nanocone arrays.

The aspect ratio of the resultant nanocones can be optimized: the size of the PS beads controls the distance between the nanocones, while the O_2 plasma etching time controls the height of the nanocones. In this paper, PS beads with a 1 μm diameter were used as the colloidal mask. In the next step, the FEP nanocone arrays were made conductive via vapor deposition of a 50 nm layer of gold, whereas the PEDOT nanocone arrays were already conductive. Finally, an additional nanostructured ZnO coating was created using electrochemistry. In this approach, 0.1 M of aqueous zinc nitrate ($Zn(NO_3)_2$) at pH 4.0 was used as the plating solution, and electrodeposition occurred at 70°C for 150 seconds at an cathodic potential of −0.9 V against a

Ag/AgCl reference electrode. The mechanism of the ZnO electrodeposition process is described as follows: At a sufficiently negative applied potential, NO_3^- ions are reduced to generate OH^- ions (Eqn. (1)). The OH^- and the Zn^{2+} ions then result in the precipitation of ZnO onto the Au or PEDOT nanocone array working electrode (Eqn. (2)).[8-11]

$$NO_3^- + H_2O + 2e^- \rightarrow NO_2^- + 2OH^- \quad (1)$$

$$Zn^{2+} + 2OH^- \rightarrow ZnO \downarrow + H_2O \quad (2)$$

3.3.2 Characterization of ZnO-Coated Nanocone Array Surfaces

Nanostructured polycrystalline ZnO films were formed directly from this facile electrodeposition method, without the need for a subsequent thermal annealing step. The electrodeposition process was monitored by chronoamperometry of the working electrode (either the Au or PEDOT nanocone arrays), as shown in Supporting Information in Appendix B. The initial increase and the subsequent gradual decrease of the absolute current density over time indicated that the conductive nanocone array surfaces became slightly passivated with the addition of a ZnO thin film.

The morphology of the ZnO-coated nanocone arrays was characterized using a combination of scanning electron microscopy (SEM), X-ray diffraction (XRD), and X-ray photoelectron spectroscopy (XPS). SEM images from Figure 3.2 and Figure 3.3 show top-down and tilted views of the nanostructured ZnO thin film on Au and PEDOT nanocone arrays, respectively.

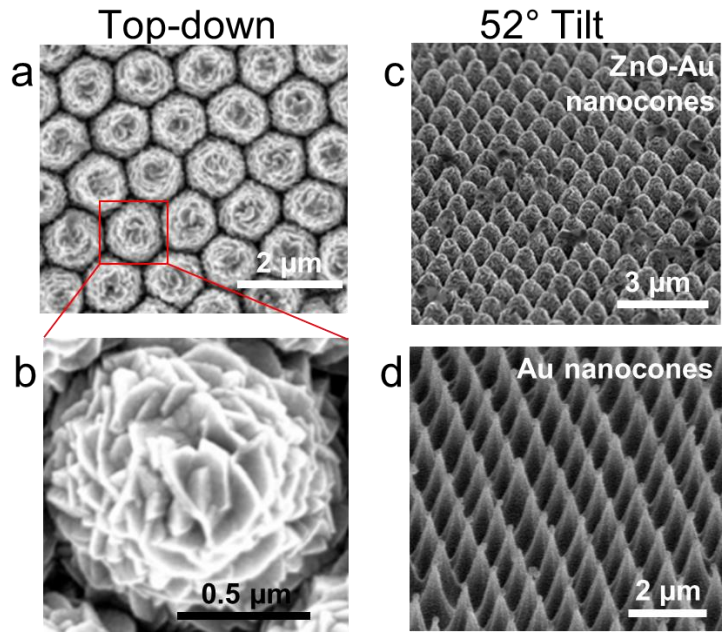

Figure 3.2. SEM images of ZnO-Au nanocone arrays from top-down (a, b) and tilted (c) views. (d) SEM image of Au nanocone arrays is shown for comparison.

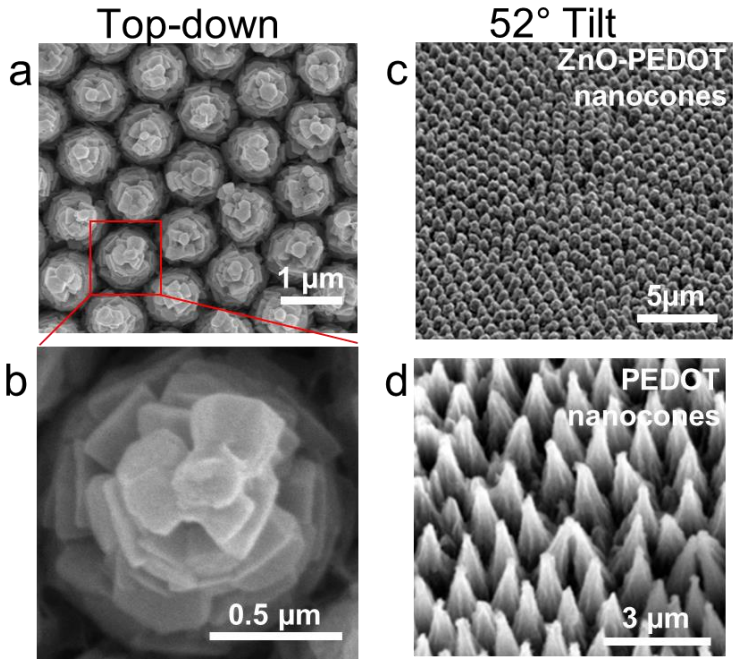

Figure 3.3. SEM images of ZnO-PEDOT nanocone arrays from top-down (a, b) and tilted (c) views. (d) SEM image of PEDOT nanocone arrays is shown for comparison.

From Figure 3.2a, c and Figure 3.3a, c, it can be seen that hexagonally closed packed ZnO-coated nanocones were created on a large scale, extending over an area of several square microns. Comparing the heights of the ZnO-coated nanocones with Au and PEDOT nanocones from Figure 3.2d and Figure 3.3d, respectively, using SEM measurements, we determined that a 25 nm of ZnO coating was formed during electrodeposition. Figure 3.2b and Figure 3.3b showed a high magnification image of an individual ZnO-coated Au and PEDOT nanocone, respectively, where we could see the individual ZnO nanostructures formed on the surface.

XRD analysis (see Supporting Information in Appendix B) revealed a polycrystalline wurzite crystal structure that grew primarily in the <002> direction, which is consistent with previous work in ZnO electrodeposition.[9,10] We also confirmed that ZnO was formed on both the Au and PEDOT nanocone array surfaces via XPS (see Supporting Information in Appendix B).

3.3.3 Photocatalytic Activity of ZnO-Coated Nanocone Array Surfaces

The photocatalytic activity of the ZnO-coated nanocone arrays was also characterized via the oxidative degradation of a methylene blue (MB) dye under UV conditions. As shown in Figure 3.4a, we evaluated the relative concentration of MB over time using UV-Vis spectroscopy under the following catalytic conditions: exposure to a ZnO-coated nanocone array surface, planar ZnO thin film surface, and no catalyst.

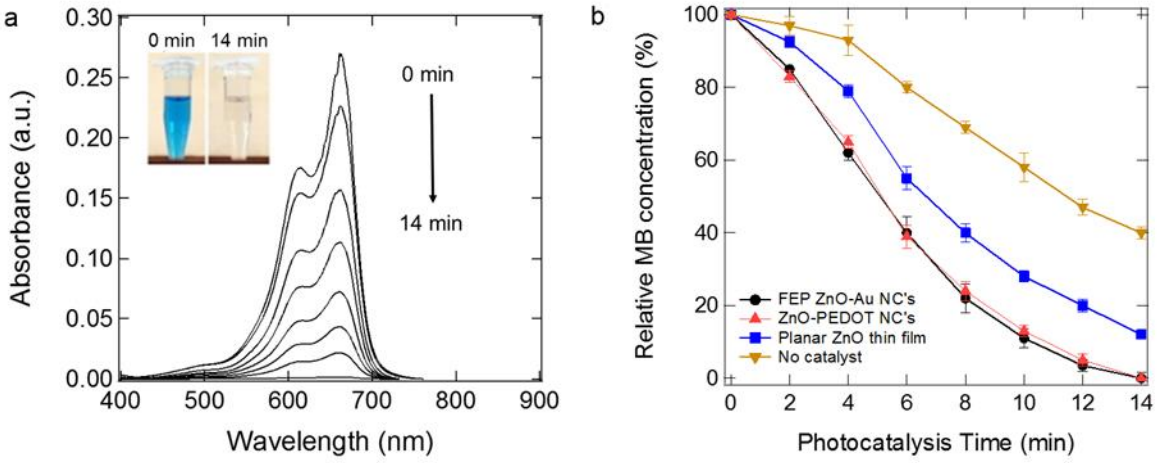

Figure 3.4. (a) UV-Vis absorbance spectra of methylene blue in the presence of the ZnO-coated nanocone array catalyst. The inset shows that the methylene blue is fully degraded after 14 minutes, thus losing all its color. (b) Confirmation of the increased surface area of the ZnO nanocone arrays via their improved photocatalytic performance in the degradation of methylene blue dye.

As shown in Figure 3.4b, 11±1% of the MB remained in solution after 14 minutes of exposure to a planar ZnO thin film surface, whereas 0±1% of the MB remained in solution after 14 minutes of exposure to a ZnO-coated nanocone array surface. It should be noted that the planar ZnO thin film surface used in this study is microscopically much smoother than the ZnO-coated nanocone array surface, as shown by the comparison of their SEM images in Supporting Information in Appendix B. For the planar ZnO thin film, the ZnO crystals are packed tightly in the <002> direction,[9,10] which drastically reduces the surface roughness factor compared to the periodic ZnO-coated nanocone arrays. This demonstrates that since the high surface area of the ZnO-coated nanocone arrays allowed for increased UV absorption,[23,24] the ZnO-coated nanocone array surface performed better as a photocatalyst compared to a planar ZnO thin film surface during MB degradation, and may find applications as self-cleaning surfaces.

3.3.4 Light Absorption of ZnO-Coated Nanocone Array Surfaces

Optical characterization revealed that the ZnO-coated nanocone array surfaces became more light absorbing and more antireflective than just Au and PEDOT nanocone arrays over a wide range of optical wavelengths from 475 nm to 800 nm. In Figure 3.5, the percent transmittance measurements of the ZnO-coated nanocone arrays compared to just Au and PEDOT nanocone arrays are shown. For all transmittance measurements, a halogen lamp was used as a white light source. The light was directed onto the nanocone array surface at a normal angle of incidence, and the transmitted light from the nanocone array surface was measured using a UV-Vis spectrometer. As shown in Figure 3.5a, the transmittance measurements of the Au nanocone arrays were T = 10% or less across the 475 nm to 800 nm spectral range, indicating strong light absorption. However, the transmittance measurements of the ZnO-Au nanocone arrays were T = 3% in the same spectral range, indicating up to a 3-fold improvement in the light absorbing ability of the Au nanocone arrays when they are decorated with ZnO nanostructures on the surface. Similarly, the transmittance measurements for the PEDOT nanocone arrays were T = 10% across the 475 nm to 800 nm spectral range, but decrease to T = 2% for the ZnO-PEDOT nanocone arrays from λ = 650 nm to 800 nm, indicating up to a 5-fold improvement in the light absorbing ability of the ZnO-PEDOT nanocone arrays across a wide range of optical wavelengths. A possible explanation for the increased light absorbance of the ZnO-coated nanocone arrays is that the ZnO nanostructures on the surface are acting as optical couplers. Although ZnO itself does not absorb in the 475 nm to 800 nm wavelength range, the ZnO nanostructures on the nanocone array surfaces act as subwavelength scattering components that result in the increased effective optical path length of incident light via coupling and trapping freely propagating plane waves between the ZnO nanostructures and the light absorbing material

underneath (either Au or PEDOT). Thus, the nanostructured ZnO surface enhances the light trapping capacity of the nanocone arrays and increases their effective absorption bands.[25,26,27]

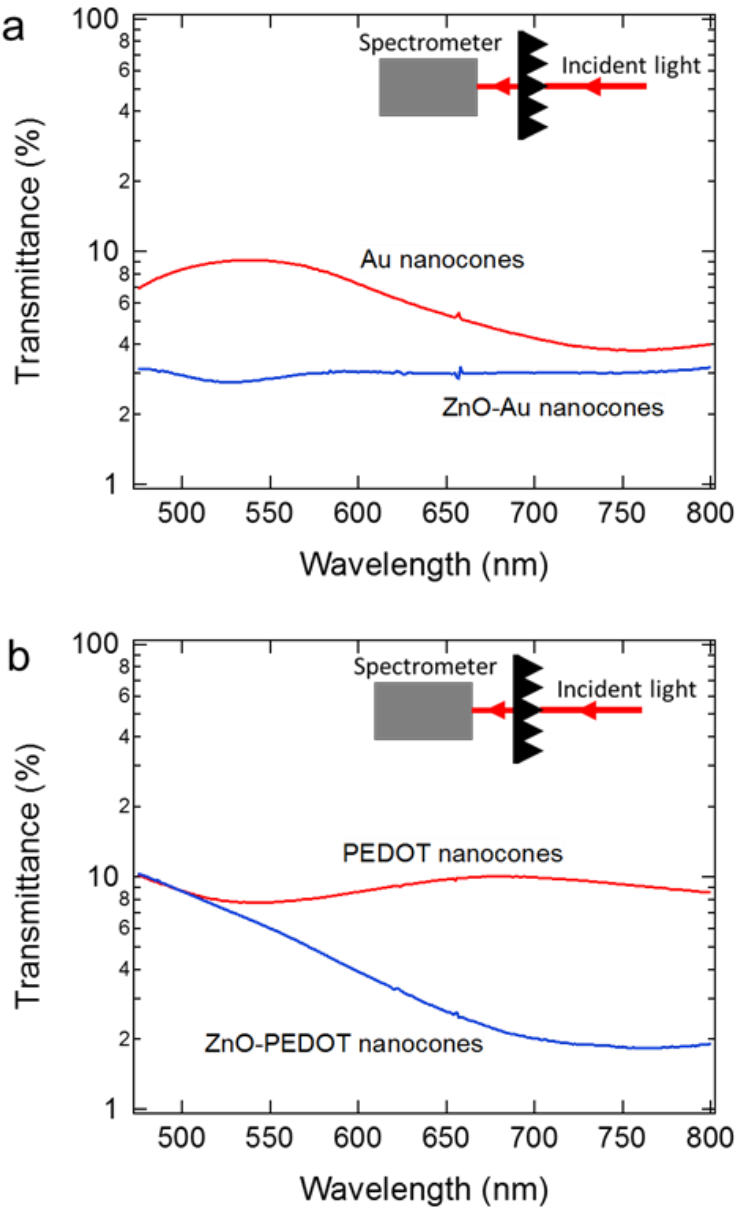

Figure 3.5. Transmittance spectra for (a) Au and ZnO-Au nanocone arrays and (b) PEDOT and ZnO-PEDOT nanocone arrays. The decrease in transmittance for the ZnO-coated nanocone arrays indicates the ZnO enhances the performance of the light absorbing material underneath (Au or PEDOT). The inserted schematic shows the optical setup used for transmittance measurements.

3.3.5 Ultra-Antireflective Properties of ZnO-Coated Nanocone Array Surfaces

The most striking effect of the addition of a nanostructured ZnO thin film onto the nanocone arrays was a significant increase in broadband antireflectivity of these surfaces. In our previous papers, we fabricated Au nanocone array surfaces that are less than 0.7% reflective ($R < 0.7\%$) at a nearly normal angle of incidence ($\theta = 8°$) from $\lambda = 475$ nm to 800 nm,[17] and we also recently fabricated PEDOT nanocone array surfaces that were less than 3% reflective ($R < 3\%$) over the same wavelength range.[18] The antireflective behavior of the ZnO-coated nanocone arrays are shown in Figure 3.6 and Figure 3.7. For the reflectivity measurements, the optical setup with a halogen lamp white light source at either angle of incidence $\theta = 8°$, 45°, or 67.5° was used as shown in the inset of Figure 3.7, and a silver mirror was used as reference calibration. In Figure 3.6a, reflectivity measurements are shown for ZnO-Au nanocones in comparison to Au and FEP nanocone arrays at $\theta = 8°$. The FEP nanocone arrays, visually matte white as seen in the photograph from Figure 3.6b, exhibited broadband antireflective properties at 2% reflective ($R = 2\%$) from $\lambda = 475$ nm to 800 nm. The addition of a 50 nm light absorbing gold thin film on the FEP nanocone arrays created a visually dark Au nanocone array surface (photograph shown in Figure 3.6c); the percent reflectivity decreased to $R < 0.7\%$ over the same spectral range, as seen in Figure 3.6a. Electrodeposition of a nanostructured ZnO film created ZnO-Au nanocone arrays that were visually even blacker than the Au nanocone arrays (Figure 3.6c), and the reflectivity measurements for the ZnO-Au nanocone arrays were reduced to $R < 0.3\%$ from 450 nm to 750 nm, with $R_{min} = 0.05\%$. We attribute the very low reflectivity exhibited by the ZnO-Au nanocone array surfaces to (i) increased light scattering by the ZnO nanostructures, and (ii) an enhancement in the graded interfacial complex refractive index created by addition of the nanostructured ZnO film to the nanocones.[28-31] To better understand the mechanism responsible

for the ultra-antireflective property of the ZnO nanocone arrays, we performed 11-phase Fresnel calculations to model the graded refractive index and absorption changes at the air/nanocone interface[32] (n_1 = air, n_{11} = bulk Au or ZnO-Au, and n_2, n_3, … , n_{10} = the effective refractive index calculated by averaging the refractive indices of air and the nanocone structure as a function of the distance away from the bottom of the nanocone). As shown in Figure 3.6, we performed these Fresnel calculations for Au nanocone arrays and ZnO-Au nanocone arrays, and the simulated reflectivity measurements match closely to our reflectivity measurements over a wide spectral range.

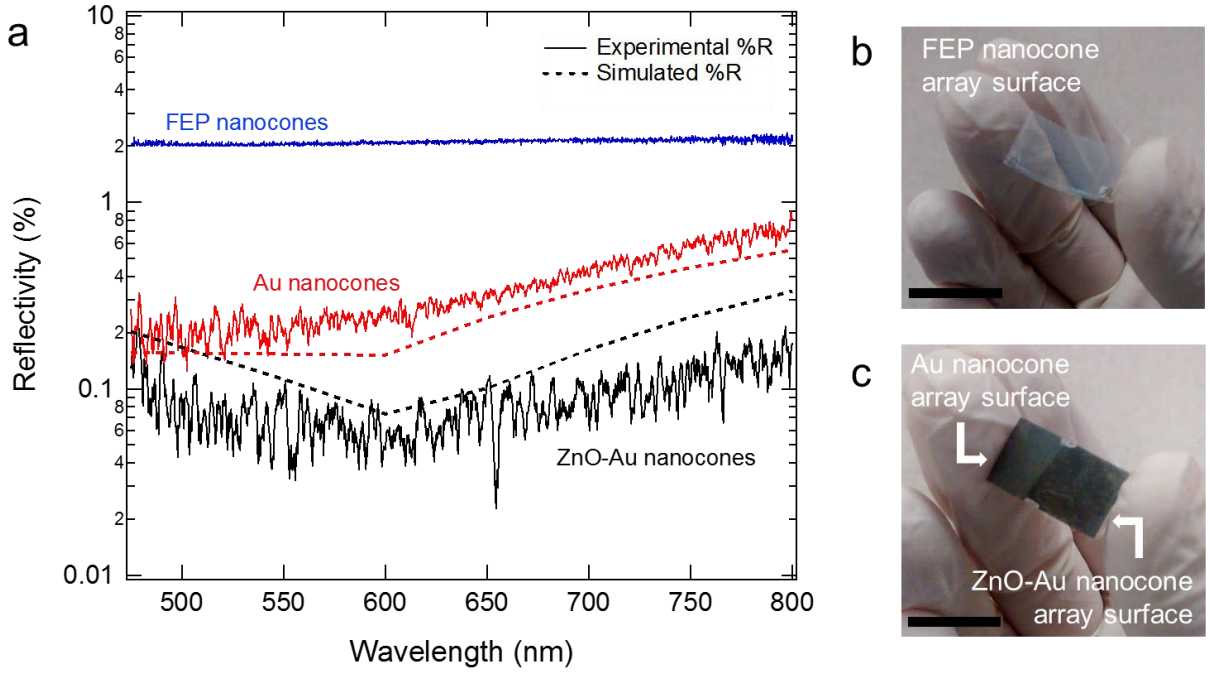

Figure 3.6. (a) Reflectivity spectra for various nanocone array structures composed of a FEP substrate. Reflectivity measurements are shown for incident light hitting the nanocone array surfaces at a nearly normal angle of incidence (θ) at 8°. Simulated reflectivity measurements obtained from 11-phase Fresnel calculations are also shown for Au and ZnO-Au nanocone arrays. The simulated and experimental reflectivity measurements match well and reveal that ZnO-Au nanocone array surfaces exhibit enhanced antireflective properties. Photographs of (b) FEP nanocone array surface, as well as (c) Au and ZnO-Au nanocone array surfaces, are shown. The scale bars on the lower left-hand corners represent 1 cm.

These calculations reveal that most of the observed decrease in reflectivity for the ZnO-Au nanocone arrays is due to the addition of a significant real refractive index component to the graded Au film (e.g., at 600 nm, $n_{Au} = 0.24 + 3.10i$, $n_{ZnO} = 2.00 + 0i$, and ZnO-Au is modeled using $n_{ZnO\text{-}Au} = 2.00 + 3.10i$). The complete Igor Pro macro for the aforementioned 11-phase Fresnel calculations is listed in Supporting Information in Appendix B.

Even more striking results were obtained for the PEDOT nanocone array surfaces. Visually, we observed once again from the photograph shown in Figure 3.7c that the ZnO-PEDOT nanocone arrays were blacker than the PEDOT nanocone arrays.

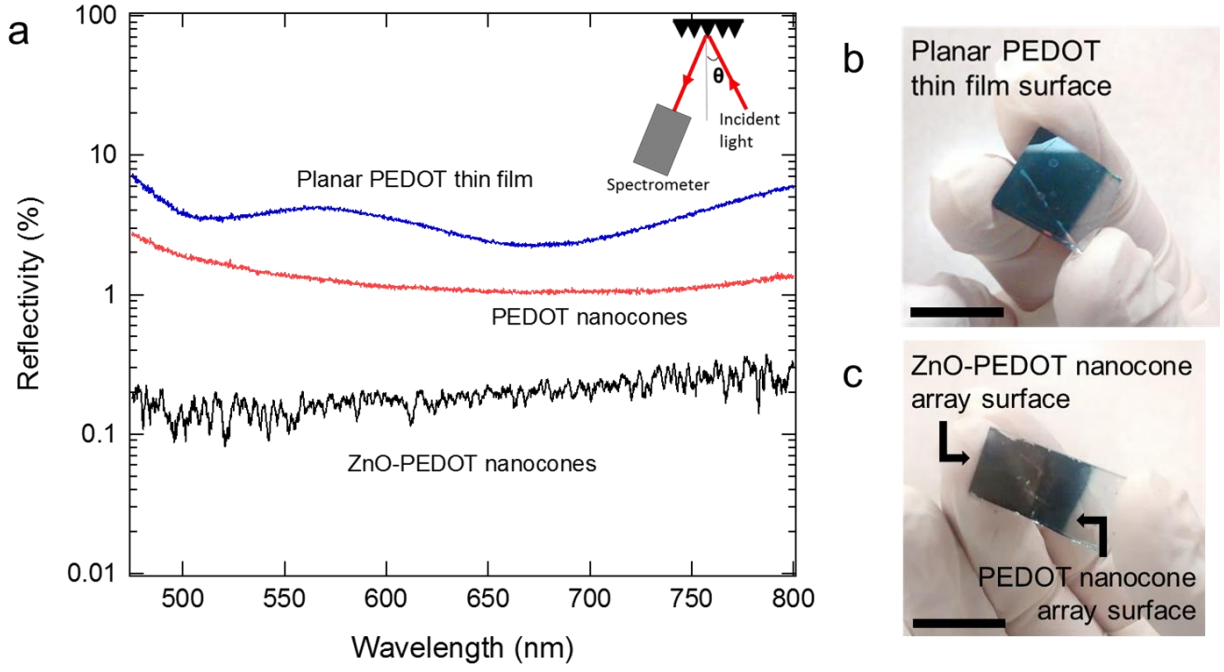

Figure 3.7. Reflectivity spectra for various nanocone array structures composed of a PEDOT substrate. The ZnO-PEDOT nanocone array surfaces exhibit enhanced antireflective properties. The inserted schematic shows optical setup used for reflectivity measurements. Reflectivity measurements are shown for incident light hitting the surfaces at a nearly normal angle of incidence (θ) at 8°. Photographs of (b) a planar PEDOT thin film surface, as well as (c) PEDOT and ZnO-PEDOT nanocone array surfaces, are shown. The scale bars on the lower left-hand corners represent 1 cm.

In Figure 3.7a, reflectivity measurements showed that while the PEDOT nanocone arrays were less than 3% reflective ($R < 3\%$) from 450 nm to 800 nm at $\theta = 8°$, the ZnO-PEDOT nanocone arrays were more than an order of magnitude less reflective at $R < 0.2\%$ over the same spectral range. Furthermore, a comparison between the reflectivity measurements of ZnO electrodeposited on a planar PEDOT thin film surface ($R < 5\%$) and the ZnO-PEDOT nanocone arrays ($R < 0.2\%$) reveals that the periodicity of the nanocone arrays, as opposed to just the roughness created by the ZnO crystals, is critical in suppressing reflectivity. Since the reflectivity spectra for both the ZnO-Au and ZnO-PEDOT nanocone arrays are very similar, the mechanism for the suppressed reflectivity of the ZnO-PEDOT nanocone arrays must be similar and thus can also be explained by increased light absorption and increased light scattering of the ZnO nanostructured surface. Finally, a very similar decrease in broadband reflectivity was also obtained for both ZnO-Au and ZnO-PEDOT nanocone arrays at higher angles of incidence ($\theta = 45°$ and $\theta = 67.5°$), as shown in Figure 3.8. To the best of our knowledge, no one has fabricated surfaces with lower reflectivity than our broadband ultra-antireflective ZnO nanostructured surfaces.

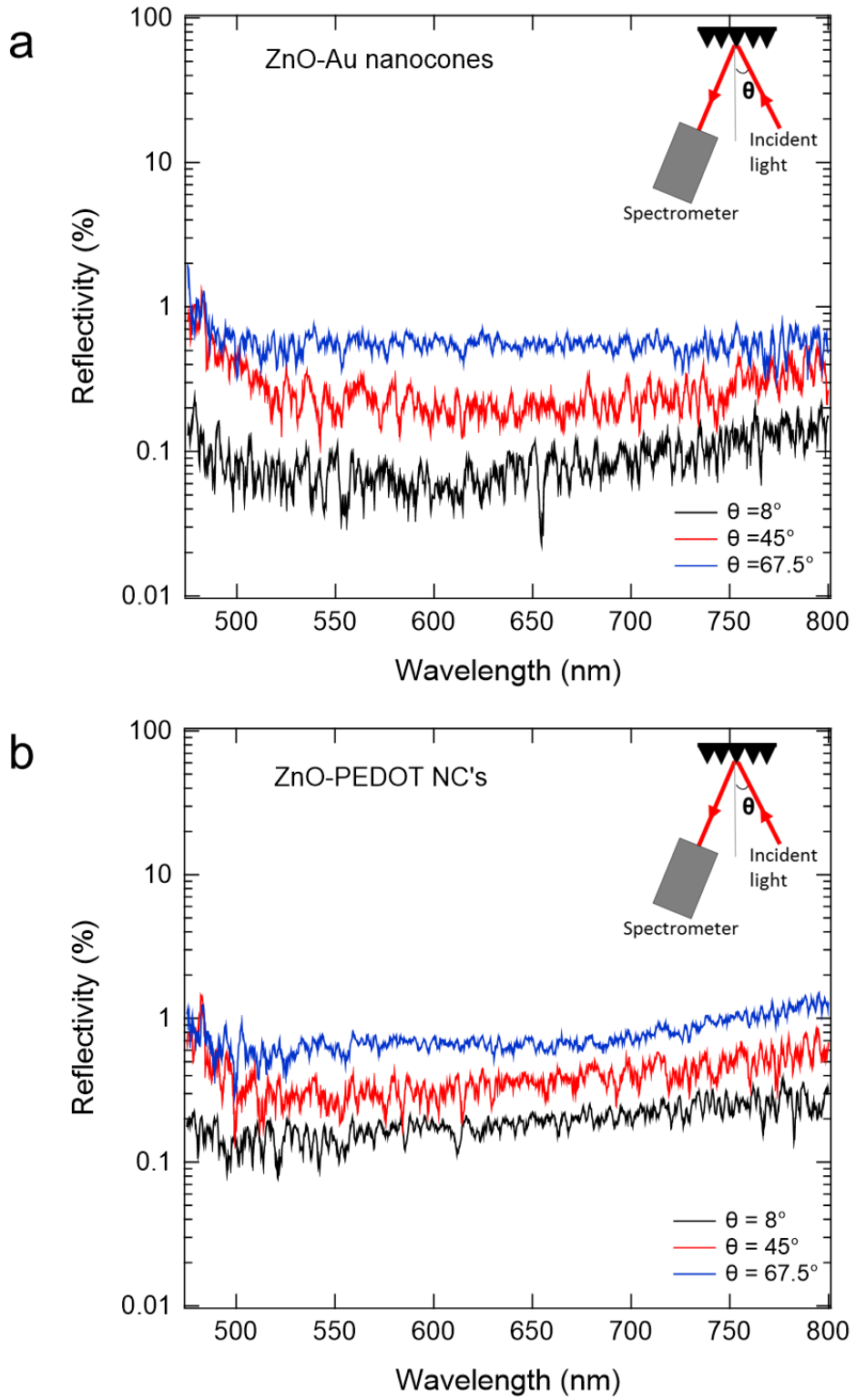

Figure 3.8. Reflectivity spectra for (a) ZnO-Au nanocone arrays and (b) ZnO-PEDOT nanocone arrays at various angles of incidence (θ), at 8° (black), 45° (red), and 67.5° (blue). The inserted schematic shows the optical setup used for reflectivity measurements.

3.4 Conclusions

We have demonstrated that electrodeposition of nanostructured ZnO films onto both FEP-Au and PEDOT periodic nanocone arrays creates excellent broadband antireflective surfaces that are less than 0.2% reflective over a large optical wavelength range of 475 nm to 800 nm. These surfaces are up to 10 times more antireflective than the nanocone arrays without the ZnO film. The nanostructured ZnO coating enhances (i) light scattering and (ii) the graded interfacial complex refractive index created by the Au or PEDOT nanocone array structures that is responsible for broadband antireflectivity. The ZnO nanostructures created from this process also increase the surface area of the nanocone arrays, resulting in a higher surface reactivity for potential photocatalytic applications. As these ZnO-coated nanocone array surfaces are easy to fabricate over large surface areas on flexible substrates, they should be easily implemented in various potential applications such as highly antireflective self-cleaning surface coatings for displays and solar panels.

3.5 Acknowledgments

This work was supported by the National Science Foundation through grant CHE-1403506. SEM, XRD, and XPS analyses were performed at the Irvine Materials Research Institute (IMRI) at UC Irvine.

3.6 References

1. Chen, Y.; Xu, Z.; Gartia, M. R.; Whitlock, D.; Lian, Y.; Liu, G. L. Ultrahigh Throughput Silicon Nanomanufacturing by Simultaneous Reactive Ion Synthesis and Etching. *ACS Nano* **2011,** *5,* 8002–8012.

2. He, J.; Gao, P.; Liao, M.; Yang, X.; Ying, Z.; Zhou, S.; Ye, J.; Cui, Y. Realization of 13.6% Efficiency on 20 um Thick Si/Organic Hybrid Heterojunction Solar Cells via Advanced Nanotexturing and Surface Recombination Suppression. *ACS Nano* **2015,** *9,* 6522–6531.

3. Fujii, T.; Gao, Y.; Sharma, R.; Hu, E. L.; DenBaars, S. P.; Nakamura, S. Increase in the Extraction Efficiency of GaN-Based Light-Emitting Diodes via Surface Roughening. *Appl. Phys. Lett*. **2004,** *84,* 855–857.

4. Araki, S.; Nakamura, K.; Kobayashi, K.; Tsuboi, A.; Kobayashi, N. Electrochemical Optical-Modulation Device with Reversible Transformation Between Transparent, Mirror, and Black. *Adv. Mater*. **2012,** *24,* OP122–OP126.

5. Wu, J. J.; Liu, S. C. Low-Temperature Growth of Well-Aligned ZnO Nanorods by Chemical Vapor Deposition. *Adv. Mater*. **2002,** *14,* 215–217.

6. Peiro, A. M.; Ravirajan, P.; Govender, K.; Boyle, D. S.; O'Brien, P.; Bradley, D. D. C.; Nelson, J.; Durrant, J. R. Hybrid Polymer/Metal Oxide Solar Cells Based on ZnO Columnar Structures. *J. Mater. Chem*. **2006,** *16,* 2088–2096.

7. Montenegro, D. N.; Souissi, A.; Martinez-Tomas, C.; Munoz-Sanjose, V.; Sallet, V. Morphology Transitions in ZnO Nanorods Grown by MOCVD. *J. Cryst. Growth* **2012,** *359,* 122–128.

8. Wahab, R.; Ansari, S. G.; Kim, Y. S.; Seo, H. K.; Kim, G. S.; Khang, G.; Shin, H.-S. Low Temperature Solution Synthesis and Characterization of ZnO Nano-Flowers. *Mater. Res. Bull*. **2007,** *42,* 1640–1648.

9. Illy, B. N.; Cruickshank, A. C.; Schumann, S.; Da Campo, R.; Jones, T. S.; Heutz, S.; McLachian, M. A.; McComb, D. W.; Riley, D. J.; Ryan, M. P. Electrodeposition of ZnO Layers for Photovoltaic Application: Controlling Film Thickness and Orientation. *J. Mater. Chem*. **2011,** *21,* 12949–12957.

10. Sun, S.; Jiao, S.; Zhang, K.; Wang, D.; Gao, S.; Li, H.; Wang, J.; Yu, Q.; Guo, F.; Zhao, L. Nucleation Effect and Growth Mechanism of ZnO Nanostructures by Electrodeposition from Aqueous Zinc Nitrate Baths. *J. Cryst. Growth* **2012,** *359*, 15–19.

11. Klochko, N. P.; Khrypunov, G. S.; Myagchenko, Y. O.; Melnychuk, E. E.; Kopach, V. R.; Klepikova, K. S.; Lyubov, V. M.; Kopach, A. V. Electrodeposited Zinc Oxide Arrays with the Moth-Eye Effect. *Semiconductors* **2014,** *48,* 531–537.

12. Tsui, K.; Lin, Q.; Chou, H.; Zhang, Q.; Fu, H.; Qi, P. Low-Cost, Flexible, and Self-Cleaning 3D Nanocone Anti-Reflection Films for High-Efficiency Photovoltaics. *Adv. Mater*. **2014,** *26,* 2805–2811.

13. Leem, J. W.; Kim, S.; Lee, S. H.; Rogers, J. A.; Kim, E.; Yu, J. S. Efficiency Enhancement of Organic Solar Cells Using Hydrophobic Antireflective Inverted Moth-Eye Nanopatterned PDMS Film. *Adv. Energy Mater*. **2014,** *4*, 1–7.

14. Wang, Y.; Lu, N.; Xu, H.; Shi, G.; Xu, M.; Lin, X.; Li, H.; Wang, W.; Qi, D.; Lu, Y., et al. Biomimetic Corrugated Silicon Nanocone Arrays for Self-Cleaning Antireflection Coatings. *Nano Res*. **2010,** *3,* 520–527.

15. Garnett, E.; Yang, P. Ordered Arrays of Dual-Diameter Nanopillars for Maximized Optical Absorption. *Nano. Lett*. **2010,** *10,* 1082–1087.

16. Wilson, S. J.; Hutley, M. C. The Optical Properties of 'Moth Eye' Antireflection Surfaces. *Opt. Acta* **1982,** *29,* 993–1009.

17. Toma, M.; Loget, G.; Corn, R. M. Fabrication of Broadband Antireflective Plasmonic Gold Nanocone Arrays on Flexible Polymer Films. *Nano Lett*. **2013,** *13,* 6164–6169.

18. So, S.; Fung, H. W. M.; Kartub, K.; Maley, A. M.; Corn, R. M. Fabrication of PEDOT Nanocone Arrays with Electrochemically Modulated Broadband Antireflective Properties. *J. Phys. Chem. Lett*. **2017,** *8*, 576–579.

19. Li, Y.; Zhang, J.; Zhu, S.; Dong, H; Jia, F.; Wang, Z.; Sun, Z.; Zhang, L.; Li, Y.; Li, H., et al. Biomimetic Surfaces for High-Performance Optics. *Adv. Mater*. **2009,** *21,* 4731–4734.

20. Busse, L. E.; Florea, C. M.; Frantz, J. A.; Shaw, L. B.; Aggarwal, I. D.; Poutous, M. K.; Joshi, R.; Sanghera, J. S. Anti-Reflective Surface Structures for Spinel Ceramics and Fused Silica Windows, Lenses and Optical Fibers. *Opt. Mater. Express* **2014**, *4*, 2504–2515.

21. Nuiis, A. M.; Horikx, J. J. Diffraction and Scattering at Antiglare Structures for Display Devices. *Appl. Opt*. **1994,** *33*, 4058–4068.

22. Tulli, D.; Hart, S. D.; Mazumder, P.; Carrilero, A.; Tian, L.; Koch, K. W.; Yongsunthon, R.; Piech, G. A.; Pruneri, V. Monolithically Integrated Micro- and Nanostructured Glass Surface with Antiglare, Antireflection, and Superhydrophobic Properties. *ACS Appl. Mater. Interfaces* **2014,** *6,* 11198–11203.

23. Shen, W.; Li, Z.; Wang, H.; Liu, Y.; Guo, Q.; Zhang, Y. Photocatalytic Degradation for Methylene Blue using Zinc Oxide Prepared by Codeposition and Sol-Gel Methods. *J. Hazard. Mater*. **2008,** *152,* 172–175.

24. Jang, Y. J.; Simer, C.; Ohm, T. Comparison of Zinc Oxide Nanoparticles and its Nano-Crystalline Particles on the Photocatalytic Degradation of Methylene Blue. *Mater. Res. Bull.* **2006,** *41,* 67–77.

25. Voss, T.; Svacha, G. T.; Mazur, E.; Konjhodzic D.; Marlow, F. High Order Waveguide Modes in ZnO Nanowires. *Nano Lett.* **2007,** *7,* 3675–3680.

26. Kim, S. K.; Song, K. D.; Kempa, T. J.; Day, R. W.; Lieber, C. M.; Park, H. G. Design of Nanowire Optical Cavities as Efficient Photon Absorbers. *ACS Nano* **2014,** *8,* 3707–3714.

27. Chang, Y.-M.; Lin, M.-L.; Lai, T.-Y.; Chen, C.-H.; Lee, H.-Y.; Lin, C.-M.; Wu, Y.-C. S.; Lin, Y.-F.; Juang, J.-Y. Broadband Omnidirectional Light Trapping in Gold-Decorated ZnO Nanopillar Arrays. *ACS Appl. Mater. Interfaces* **2017,** *9,* 11985–11992.

28. Tian, Y.; Hu, C.; Xiong, Y.; Wan, B.; Xia, C.; He, X.; Liu, H. ZnO Pyramidal Arrays: Novel Functionality in Antireflection. *J. Phys. Chem. C* **2010,** *114,* 10265–10269.

29. Robak, E.; Kotkowiak, M.; Drozdowski, H. Nanostructured Zinc Oxide Systems with Gold Nanoparticle Pattern for Efficient Light Trapping. *J. Phys. D: Appl. Phys*. **2016,** *49,* 045104.

30. Xu, S.; Adiga, N.; Ba, S.; Dasgupta, T.; Wu, C. F. J.; Wang, Z. L. Optimizing and Improving the Growth Quality of ZnO Nanowire Arrays Guided by Statistical Design of Experiments. *ACS Nano* **2009,** *3,* 1803–1812.

31. Jheng, B.-T.; Liu, P.-T.; Wang, M.-C.; Wu, M.-C. Effects of ZnO-Nanostructure Antireflection Coatings on Sulfurization-Free Cu_2ZnSnS_4 Absorber Deposited by Single-Step Co-Sputtering Process. *Appl. Phys. Lett*. **2013,** *103,* 052904.

32. Bond, W. L. Measurement of the Refractive Indices of Several Crystals. *J. Appl. Phys.* **1965,** *36,* 1674-1677.

Chapter 4

Quantitative Characterization of Optical Coupling in Nanoporous ZnO-WO_3 and ZnO-PEDOT Composite Electrodeposited Gratings using Electrodiffraction Measurements

4.1 Introduction

Zinc oxide's (ZnO) well-documented optical properties have been utilized for a variety of light-based applications. For example, its wide band gap (3.37 eV) has made ZnO a popular semiconductor material for photosensitized dyes with enhanced photovoltaic efficiency.[1-3] In addition to its semiconductor capabilities, ZnO has been observed to enhance the optical properties within various systems. ZnO was reported to improve the light trapping capabilities of

solar cells both as a thin film on an absorbing material[4] and as a nanopatterned surface.[5-6] Within our lab, we observed that ZnO nanostructures used in a hierarchical fashion on Au and PEDOT nanocone array surfaces enhanced the antireflective properties of the nanocone arrays via optical coupling.[7] This is striking because while ZnO has no absorptive properties itself, it seemed to enhance those of the host material beneath. To further our understanding of the optical enhancement of ZnO, we extend our previous work on ZnO nanocone arrays and turn to optical diffraction gratings made of composite electrodeposited ZnO and electrochromic WO_3 or PEDOT in order to quantify the optical coupling effects.

Optical diffraction gratings that split, redirect, and disperse light are fundamental optical elements that have been incorporated into a myriad of optical devices including laser barcode scanners, optical switches, and spectrometers.[8-16] Their simple design only requires a surface or thin film material with an optical response that varies periodically on the order of the wavelength of light in order to exhibit optical diffraction. If we define the linear optical response in terms of the complex refractive index $n = \eta + i\kappa$, then periodic variations in κ are typically called absorptive gratings, while periodic variations in η are described as phase gratings.[17-23] Within our own system, ZnO is known to have a large η value (η = 1.998 at 633 nm), but no κ. Therefore we theorize that any changes observed in κ in the presence of ZnO must be due to coupling of the ZnO with the absorptive components within the gratings.

In order to probe the absorptive effects (κ) in addition to the refractive effects (η) of our optical gratings, electrochromic materials were selected as an absorptive host material. Electrochromic thin films are a unique class of materials with a complex refractive index that can be varied reversibly by either oxidation or reduction reactions induced by changes in an applied potential in an electrochemical cell. The electrochromism of these thin films specifically refers to

the electrochemically induced color changes. Considering that any changes to the absorptive properties of a material implies a change to the imaginary part of the refractive index, electrochromic thin films demonstrate a potential dependence of κ; however, changes in η, the real part of the complex refractive index, can also occur. Two of the most well-studied electrodeposited electrochromic thin film materials are tungsten oxide (WO_3)[24-27] and poly(3,4-ethylenedioxythiophene) (PEDOT).[28-32] Typical potential dependent variations of κ for these two materials are ±0.09 and ±0.07, respectively, in the visible region at 600 nm.[33-34] Due to the potential dependence of η and κ for electrochromic thin films, diffraction gratings that are fabricated from these materials also exhibit a diffraction efficiency that varies with applied potential. This effect has been observed previously and has been denoted as either "electrochemically modulated diffraction"[22, 35-37] or "electrotunable diffraction",[38-39] but in this paper, we will denote this phenomenon simply as "electrodiffraction."

In this article, we have observed and quantified the enhancement of electrodiffraction from a novel two-component composite nanostructured diffraction grating that incorporates both an electrochromic material (either WO_3 or PEDOT) and a nanostructured high refractive index ZnO (η = 1.998 at 633 nm). These composite gratings are fabricated by a two-step electrodeposition process on a fluorine-doped tin oxide (FTO) coated glass substrate as depicted schematically in Figure 4.1. A pattern of 10 μm wide lines of either WO_3 or PEDOT separated by 5 μm of glass is created by electrodeposition onto an FTO glass substrate that is partially protected with a photopatterned film of photoresist. This initial electrochromic grating pattern has a film thickness of about 200 nm. A second electrodeposition step creates a nanostructured ZnO film on top of the electrochromic grating, with a film thickness of typically 600 nm. We show that this non-absorbing nanostructured ZnO film enhances both the optical absorption and

the electrodiffraction from this grating; the optical coupling between ZnO and the electrochromic host material and results in a four-fold increase of the electrodiffractive response.

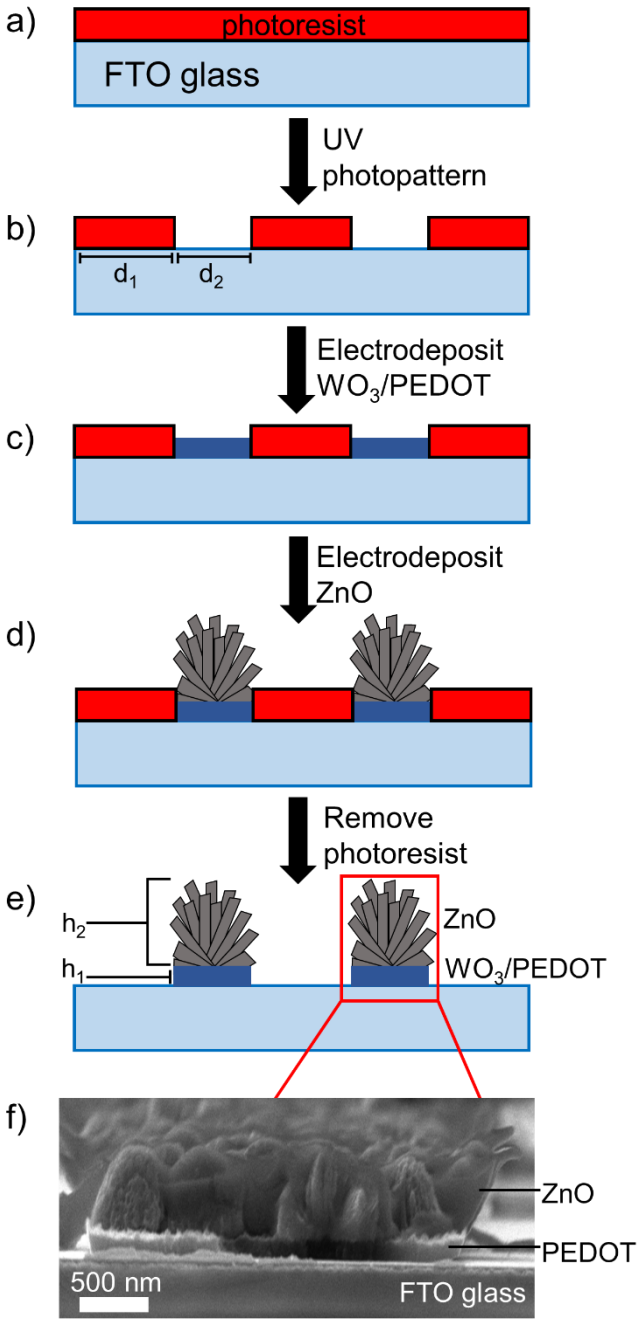

Figure 4.1. Schematic of the fabrication process of ZnO-WO_3 and ZnO-PEDOT gratings shown in a) – e). A cross-sectional SEM image f) reveals the various components of a sample ZnO-PEDOT grating.

4.2 Experimental Section

4.2.1 Fabrication of WO_3 Gratings

FTO coated glass slides (~30 Ω/sq cm, Sigma-Aldrich) were cleaned by ultrasonication in an aqueous Hellmanex (1%) solution, rinsed with deionized water and ethanol, and dried under an N_2 stream. The FTO coated glass slides were then plasma cleaned under O_2 plasma for 2 min. S1808 positive photoresist was spincoated at 2500 rpm for 80 s onto the glass slides, baked at 90°C for 25 min to evaporate photoresist solvent, and cooled to room temperature. The photoresist coated glass slides were exposed to a UV lamp source (50 W, Oriel Instruments He(Xe) arc lamp) for 3.5 s and patterned using a photomask with 5 μm wide Cr lines and 10 μm glass spacings. The photoresist was then developed for 25 s using MF-319 developer (Microchem), rinsed with deionized water, and dried under an N_2 stream. An electrical contact area was made by dissolving the corner of the photoresist with acetone using a Q-tip. WO_3 was then electrochemically deposited onto the photopatterned FTO substrate using a potentiostat (PGSTAT12, Metrohm Autolab) in a three-electrode setup. The working electrode of the photopatterned FTO substrate was exposed to an aqueous peroxytungstatic acid ($H_2W_2O_{11}$) plating solution for 150 s at a cathodic potential of −0.5 V vs. a Ag/AgCl reference electrode in the presence of a Pt counter electrode.

4.2.2 Fabrication of PEDOT Gratings

FTO glass slides (~30 Ω/sq cm, Sigma-Aldrich) were degreased by sonication in deionized water, acetone, and methanol, and then dried with a nitrogen jet. Poly(3,4-ethylenedioxythiophene)-poly(styrenesulfonate) (PEDOT:PSS, 2.0 wt. % in H_2O, Sigma-Aldrich) was mixed with isopropyl alcohol and ethylene glycol (ratio 85:10:5) to enhance electronic conductivity and improve wetting. A thin PEDOT:PSS layer was spincoated onto the

FTO glass substrate at 3000 rpm for 20 s. Positive photoresist (S1808, Microchem) was then spincoated at 2500 rpm for 80 s onto the FTO glass substrate, and baked at 90°C for 25 min to evaporate the photoresist solvent. After cooling down to room temperature, the photomask with 5 μm wide Cr lines and 10 μm glass spacings was placed flushed onto the substrate. The photoresist was exposed through the photomask using a UV lamp source (50 W, Oriel Instruments He(Xe) arc lamp) for 3.5 s. The photoresist was patterned and developed with MF-319 developer, rinsed with deionized water, and dried under a N_2 stream. An electrical contact area was made by dissolving the corner of the photoresist with acetone using a Q-tip. The PEDOT electrodeposition was performed with a potentiostat (PGSTAT12, Metrohm Autolab), where the FTO glass substrate was exposed to an aqueous electrolyte consisted with 0.02 M 3,4-ethylenedioxythiophene (EDOT, 97%, Sigma-Aldrich), 0.1 M sodium dodecyl sulfate (SDS) and 0.1 M lithium perchlorate ($LiClO_4$, 99.5%, Alfa), at a constant potential of +1.0 V vs. a Ag/AgCl reference electrode for 45 s in the presence of a Pt counter electrode.

4.2.3 Fabrication of Nanostructured ZnO Gratings

The electrodeposition of nanostructured ZnO was performed with a potentiostat (PGSTAT12, Metrohm Autolab) using a three-electrode setup. An aqueous solution containing 0.1 M $Zn(NO_3)_2$•$6H_2O$ (98%, Sigma-Aldrich) and 0.1 M KCl heated to 70°C was used as the plating solution. The working electrode of either a WO_3 or PEDOT grating array surface was exposed to the plating solution for 600 s at a constant potential of −0.9 V vs. a Ag/AgCl reference electrode and in the presence of a Pt counter electrode to form a nanostructured ZnO film over the WO_3 or PEDOT gratings. Finally, the sample was rinsed with acetone to remove remaining photoresist, and dried under a N_2 stream.

4.2.4 Morphological Characterization

SEM images were obtained using a FEI Magellan 400 field-emission scanning electron microscope at an accelerating voltage of 5 kV. AFM measurements were collected using an Asylum Research MFP-3D, and AFM images were analyzed using Gwyddion imaging processing software. XPS measurements were collected using a Kratos Analytical AXIS Supra surface analysis instrument, with an emission current of 15 mA during analysis. For UV-Vis/NIR absorbance measurements, a Jasco V-670 UV-Vis/NIR spectrophotometer was used. To measure *ex situ* absorbance spectra, a potential of −1.0 V vs. Ag/AgCl was applied to the grating surfaces for 30 s in a 0.1 M $LiClO_4$ in polycarbonate solution before removing the grating surfaces from solution for spectroscopic analysis. To measure *in situ* absorbance spectra, UV-Vis/NIR measurements were collected while a potential of −1.0 V vs. Ag/AgCl was applied to the grating surfaces in a 0.1 M $LiClO_4$ in polycarbonate solution.

4.2.5 Optical Diffraction Analysis

For diffraction and transmittance measurements, the grating surface was placed in an electrochemical cell connected to a potentiostat (Palmsens3, Palmsens) in a three-electrode setup. The grating sample was placed in a 0.1 M $LiClO_4$ in polycarbonate solution under alternating step potentials of −1.0 V and +1.0 V (15 s at each potential for a total duration of 250 s) vs. a Ag/AgCl reference electrode and in the presence of a Pt counter electrode. Light from a HeNe laser (λ = 633nm, 12 mW, LHRP-1201, Research Electro-Optics), *p*-polarized using a polarizer (Newport), was emitted and chopped at a frequency of 1.0 kHz using an optical chopper (Stanford Research Instruments SR540). A transmission geometry was employed in these optical measurements, where the intensities of the diffracted light (at the n = 1 spot) and transmitted light (at the n = 0 spot) were measured by a photodiode (Hamamatsu) connected to a DSP lock-in amplifier (EG&G model 7220). The photodiode potentials were recorded by a

Labview program. For %T measurements at the $n = 0$ spot, a FTO glass substrate was used as reference. For %DE measurements, the photodiode intensities at the $n = 1$ spot were divided by the photodiode intensity at the $n = 0$ spot at +1.0 V vs. Ag/AgCl (when the grating is at its most transmissive state).

4.3 Results and Discussion

4.3.1 Electrodeposition and Characterization of ZnO-WO_3 and ZnO-PEDOT Gratings

4.3.1.1 WO_3 electrodeposition

The mechanism of WO_3 electrodeposition from acidic peroxytungstatic acid ($H_2W_2O_{11}$) solutions has been described previously by other researchers.[40-41] Electrodeposition occurred at negative potentials (−0.4 V vs. Ag/AgCl for 150 s) through a combination of electrochemical reduction and disproportionation of the four peroxide (O_2^{2-}) anions in the peroxytungstate ions as described in Equation 1, where x is either 0, 4 or 8:

$$W_2O_{11}^{2-} + (2+x)\,H^+ + xe^- \rightarrow 2WO_3 + \frac{(2+x)}{2}H_2O + \frac{(8-x)}{4}\,O_2 \qquad (1)$$

If $x = 8$, then all four of the peroxide anions are reduced electrochemically to three O^{2-} ions (in the electrodeposited WO_3) and five H_2O. If $x = 0$, then the four peroxide anions disproportionate to form three O^{2-} ions, H_2O and two O_2. In addition to the peroxide reduction, a non-stoichiometric amount of W^{6+} ions in the WO_3 are also reduced to W^{5+}:

$$zH^+ + WO_3 + ze^- \rightarrow H_zWO_3 \qquad (2)$$

This tungsten reduction is verified by the observation of a blue color of the electrodeposited WO_3 film.

4.3.1.2 PEDOT electrodeposition

A PEDOT film was formed by the electrodeposition of 3,4-ethylenedioxythiophene (EDOT) using a slightly modified procedure of a previously reported method.[42-45] To generate stable, uniform PEDOT films, it was necessary to first spincoat a thin layer of PEDOT:PSS solution onto the FTO glass substrate to enhance conductivity and improve wetting of the surface, followed by the electropolymerization of EDOT to form a thicker layer of PEDOT. For the electrodeposition, an aqueous plating solution consisting of 0.02 M EDOT, 0.1 M SDS and 0.1 M $LiClO_4$ was employed. A constant potential of +1.0 V vs. Ag/AgCl was applied for 45 s to a photopatterned FTO glass substrate in the presence of a Pt counter electrode, creating a large scale (on the squared cm scale) uniform electroactive film. The electrodeposited film is in the reduced state, as evidenced by its blue color.

4.3.1.3 ZnO electrodeposition

Nanostructured ZnO was selectively deposited electrochemically on top of the WO_3 or PEDOT thin film. In our approach, 0.1 M aqueous zinc nitrate at pH 4.0 heated to 70°C was used as the plating solution, and electrodeposition occurred for 600 s at a potential of −0.9 V vs. Ag/AgCl to ensure full coverage of ZnO over WO_3 or PEDOT gratings. An SEM image of a ZnO-PEDOT grating sample with a ZnO electrodeposition time of 300 s, as shown in Supporting Information Figure S1, revealed sparse coverage of ZnO on the grating surface. The mechanism of the ZnO electrodeposition process has been discussed in previous works,[7, 46-47] and is summarized as follows: At a sufficiently negative applied potential, OH^- ions are generated, likely via the reduction of NO_3^- (Eqn. (4)). The OH^- and the Zn^{2+} ions then result in the precipitation of ZnO onto the working electrode of either WO_3 or PEDOT gratings (Eqn. (5)).

$$NO_3^- + H_2O + 2e^- \rightarrow NO_2^- + 2OH^- \quad (4)$$

$$Zn^{2+} + 2OH^- \rightarrow ZnO \downarrow + H_2O \quad (5)$$

4.3.1.4 Grating fabrication

The ZnO-WO_3 and ZnO-PEDOT gratings were fabricated using a combination of photolithography and electrodeposition. As shown in the scheme in Figure 4.1, after a layer of photoresist was spincoated onto conductive FTO glass slides, UV photopatterning was employed to create an array of photoresist stripes of width d_1 = 5 µm that were separated by 10 µm spacings of glass substrate. WO_3 or PEDOT was then selectively deposited electrochemically onto the exposed glass to form arrays of continuous micron-scale stripes of width d_2 = 10 µm. After the electrodeposition of both the electrochromic and ZnO layers, the photoresist was removed using acetone to create a diffraction grating surface that consists of an array of 10 µm wide ZnO-WO_3 or ZnO-PEDOT stripes separated by 5 µm wide spacings. The morphology of the ZnO-WO_3 and ZnO-PEDOT diffraction gratings was characterized using a combination of SEM, AFM, and XPS. A cross-sectional SEM image in Figure 4.1f shows the various components of a sample composite ZnO-PEDOT grating, while SEM images in Figure 4.2 shows a) ZnO-WO_3 gratings and b) ZnO-PEDOT gratings that are composed of an array of 10 µm wide stripes that extend continuously over a length of several microns with 5 µm spacings in between.

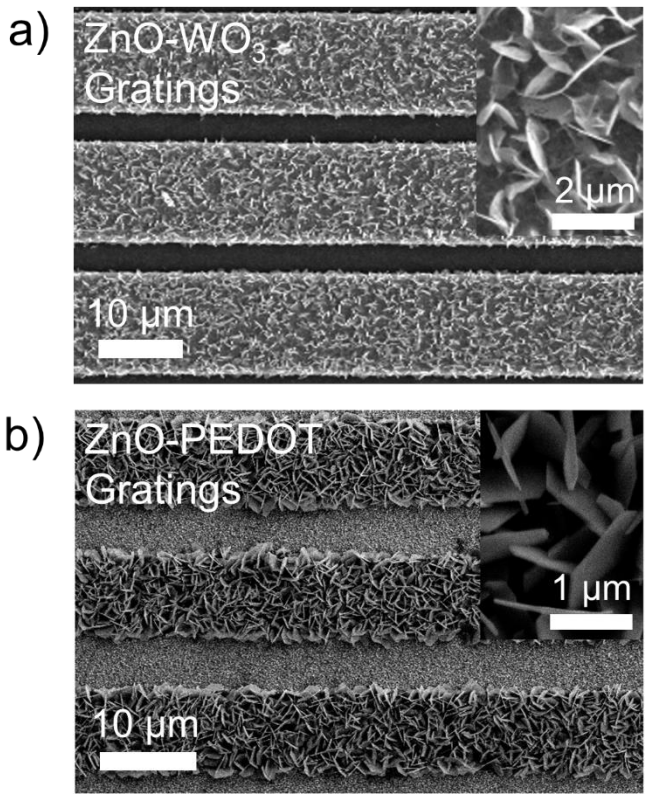

Figure 4.2. SEM images of a set of a) ZnO-WO_3 and b) ZnO-PEDOT gratings. The insets show high-resolution images of the nanostructured ZnO overlayer decorating the gratings.

It should also be noted that the lower contrast in Figure 4.2b compared to Figure 4.2a is due to the presence of a thin layer of PEDOT:PSS in the 5 μm spacings between the ZnO-PEDOT stripes in the ZnO-PEDOT gratings (since a thin layer of PEDOT:PSS was spincoated onto the FTO glass substrate to ensure stable electropolymerized PEDOT thin films), whereas the ZnO-WO_3 stripes are separated by 5 μm spacings of glass substrates in the ZnO-WO_3 gratings. The insets of the SEM images show high-resolution images of the nanostructured ZnO, where the individual flake-like ZnO nanostructures on the surface are depicted. This is a contrast to the mostly planar and featureless morphology of the WO_3 or PEDOT gratings before the addition of the ZnO layer, as confirmed by SEM images in Supporting Information in Appendix C. In addition, AFM measurements (see Supporting Information in Appendix C) reveal that an

electrochromic layer of height h_1 = 200 nm was formed, and a nanostructured ZnO layer of height h_2 = 600 nm was formed. Furthermore, XPS measurements confirmed the formation of ZnO over both the WO_3 and PEDOT grating surfaces (shown in Supporting Information in Appendix C).

4.3.2 Absorbance Spectra of ZnO-WO_3 and ZnO-PEDOT Gratings

The absorbance spectra of the composite gratings were measured using a normal incidence transmission geometry, and it was revealed that the addition of a nanostructured ZnO overlayer on both the WO_3 and PEDOT gratings resulted in enhanced light absorption capabilities. The UV-Vis/NIR absorbance spectra for an electrodeposited WO_3 thin film (blue curve), an electrodeposited WO_3 grating (red curve) and an electrodeposited composite ZnO-WO_3 grating (black curve) are all shown in Figure 4.3a. These three *ex situ* spectra were obtained from samples that were first held at an applied potential of −1.0 V vs. Ag/AgCl for 30 s in an electrochemical cell containing a 0.1 M $LiClO_4$ solution, then removed for spectroscopic measurements. As seen in Figure 4.3a, there is a strong absorbance peak around 1000 nm for the both the planar WO_3 thin films and the WO_3 gratings. Photographs of these two surfaces are also shown in Figure 3a and both exhibit the well-known blue color associated with reduced WO_3 electrochromic films. The spectrum of the WO_3 grating shows a slightly stronger absorption band than the planar thin film, and thus the color of the WO_3 grating is a darker blue.

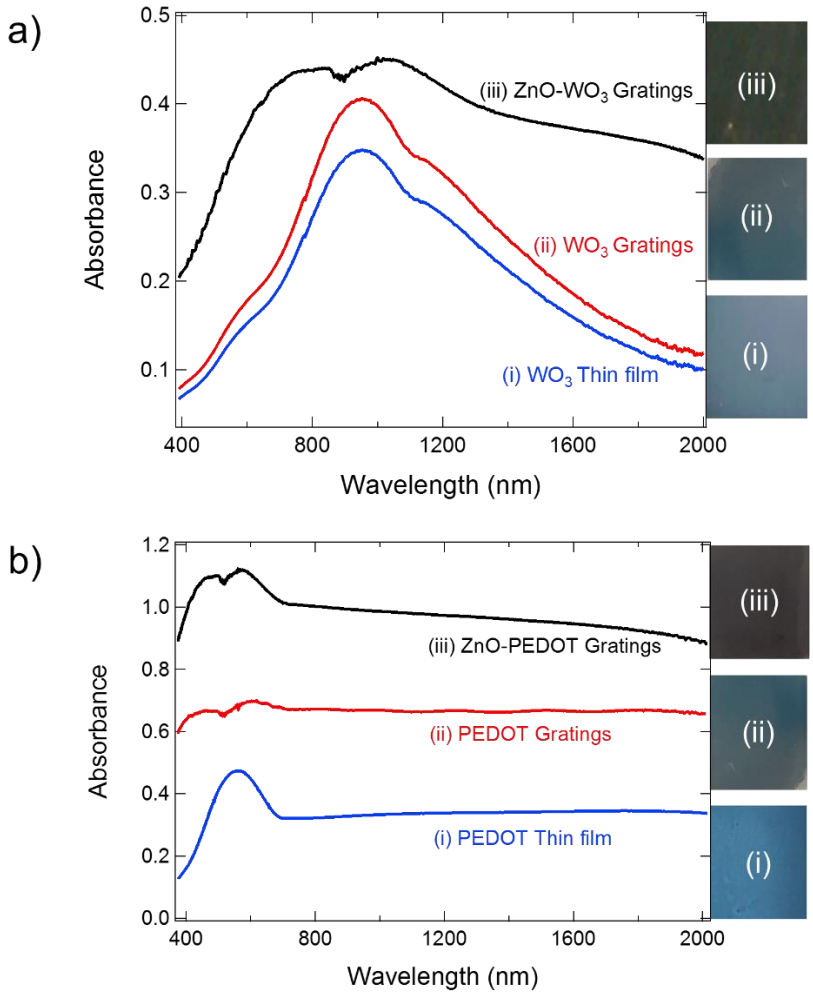

Figure 4.3. a) UV-Vis/NIR spectra of ZnO-WO_3 gratings, WO_3 gratings, and WO_3 thin film. b) UV-Vis/NIR spectra of ZnO-PEDOT gratings, PEDOT gratings, and PEDOT thin film. Photographs of each sample are also shown.

In contrast, the spectrum of the ZnO-WO_3 grating shows significantly enhanced absorbance at all wavelengths from 400 nm to 2000 nm. The addition of the nanostructured ZnO overlayer must enhance the light absorption capabilities of the WO_3 grating underneath, since the electrodeposited ZnO has a high refractive index but no absorptive component ($\kappa = 0$). The UV-Vis/NIR absorbance spectrum of ZnO does not exhibit any absorption bands from 400 nm to 2000 nm, due to its high bandgap of 3.3 eV (375 nm).[48] Nevertheless, the addition of ZnO to

form the ZnO-WO_3 gratings significantly enhances the optical absorption of the WO_3 gratings. The enhanced absorption also results in changes in visual appearance of the ZnO-WO_3 gratings, which becomes black as shown in Figure 4.3a. This data clearly shows that there is a significant amount of light coupled or redirected from the nanostructured ZnO overlayer to the underlying WO_3 portion of the grating structure.

A similar effect was observed for ZnO-PEDOT gratings. The UV-Vis/NIR absorbance spectra of an electrodeposited planar PEDOT thin film, an electrodeposited PEDOT grating, and an electrodeposited ZnO-PEDOT grating are shown in Figure 4.3b. It has been shown previously that PEDOT thin films exhibit a π to π^* transition with a bad gap of 1.7 eV (775 nm), thus PEDOT thin films in the reduced state show significant optical absorption near 600 nm,[31-32, 49] as evidenced by the blue trace in Figure 4.3b. Similar to the WO_3, PEDOT films also have a characteristic blue color in the reduced state as seen in the inset to Figure 4.3b. The PEDOT grating adds an additional absorption band at 450 nm (see Figure 4.3b) that has been attributed to an interference effect of the PEDOT grating, and is a darker blue in color as seen in the Figure 4.3b inset. As in the case of the ZnO-WO_3 gratings, the ZnO-PEDOT gratings also show a broadband enhancement in the UV-Vis/NIR absorbance spectrum, and has a black visual appearance, also seen in the inset of Figure 4.3b. We attribute this enhanced absorption from of ZnO-PEDOT gratings to the same mechanism as in the of ZnO-WO_3 gratings: coupling or redirection of light from the nanostructured ZnO overlayer to the underlying PEDOT grating.

4.3.3 Electrodiffraction of ZnO-WO_3 and ZnO-PEDOT Gratings

While the nanostructured ZnO overlayer enhances the absorptive properties of WO_3 and PEDOT gratings, there is an even larger effect on the electrochemically modulated diffraction.

Electrodiffraction from electrodeposited ZnO-WO_3 and ZnO-PEDOT gratings at λ= 633 nm was measured *in situ* at normal incidence in an electrochemical cell containing 0.1 M $LiClO_4$ in polycarbonate, as shown schematically in Figure 4.4a. A representative diffraction pattern is shown in Figure 4.4b.

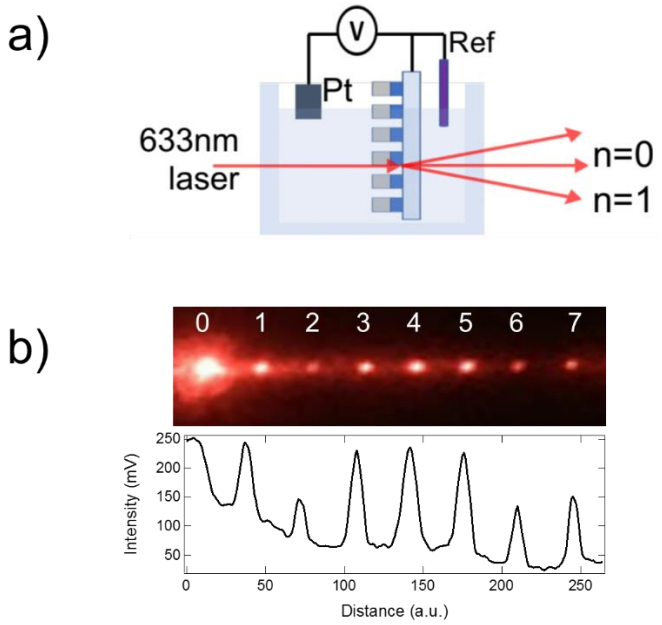

Figure 4.4. a) Schematic of the setup used for electrochemically modulated optical measurements of ZnO-WO_3 and ZnO-PEDOT gratings. b) Photograph of and intensity profile of diffraction pattern created by a set of ZnO-WO_3 gratings.

To measure the electrodiffractive and electrochromic response, the applied potential to a ZnO-WO_3 or ZnO-PEDOT grating was stepped between −1.0 V to +1.0 V vs. Ag/AgCl every 15 seconds. The current transients from the potential steps are shown in Figure 4.5. The current transients are higher for the ZnO-WO_3 grating as compared to the WO_3 grating, as shown in Figure 4.5b; we attribute this to the larger charging currents for high surface area nanostructured ZnO. Similar trends were observed for the ZnO-PEDOT and PEDOT gratings in Figure 4.5c.

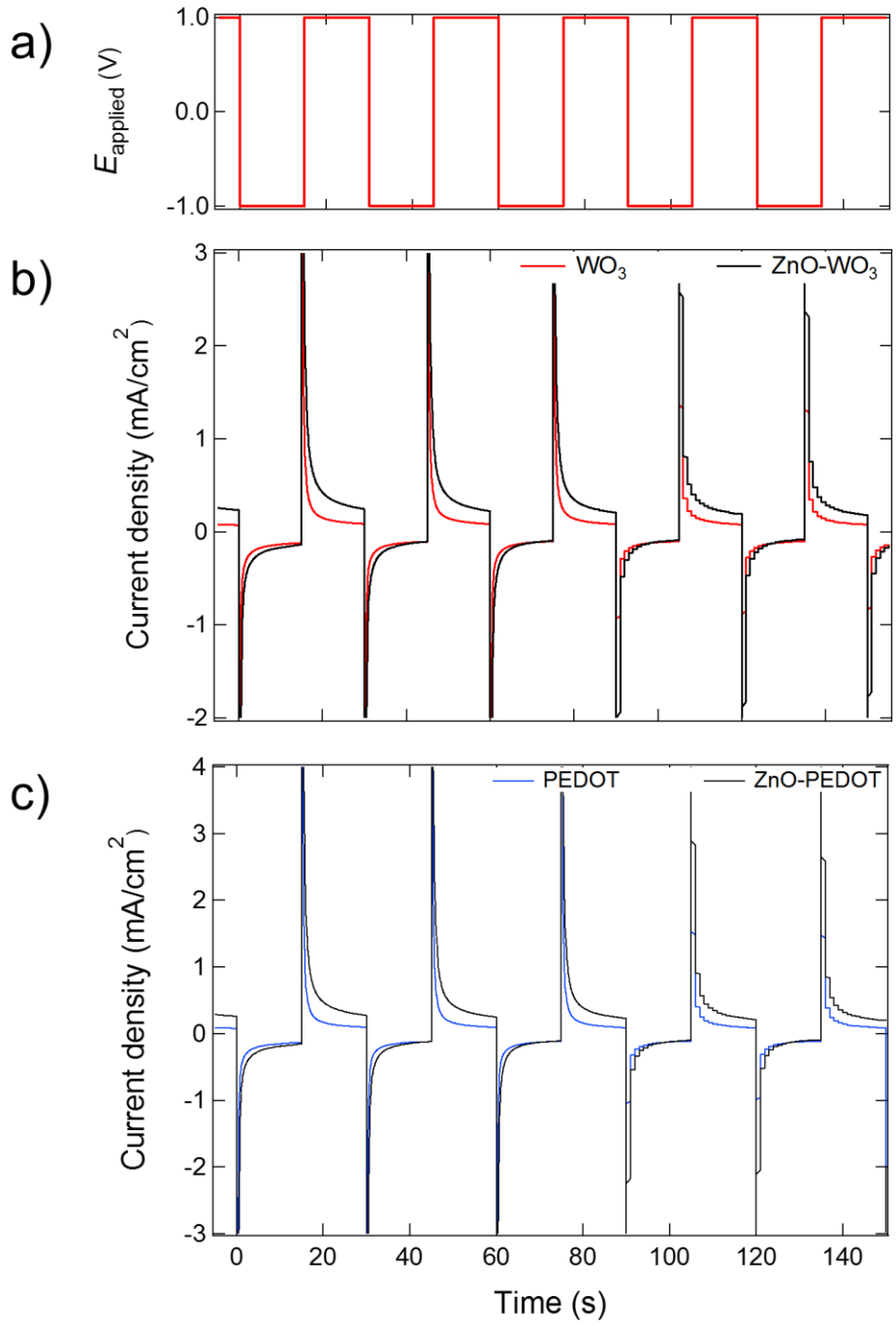

Figure 4.5. a) For the applied step potentials of −1.0 V and +1.0 V vs. Ag/AgCl, corresponding current transients for b) ZnO-WO_3 and WO_3 gratings, as well as c) ZnO-PEDOT and PEDOT gratings are shown.

The electrochemically modulated optical signals for electrochromic changes (transmission at $n = 0$) and first order diffraction ($n = 1$) were acquired as a function of time from both ZnO-WO_3 gratings (Figures 4.6b and 4.6c) and ZnO-PEDOT gratings (Figures 4.7b and 4.7c). Transmission measurements at $n = 0$ were collected *in situ* at normal incidence at $\lambda = 633$ nm in an electrochemical cell containing 0.1 M $LiClO_4$ in polycarbonate using a FTO coated glass slide as reference. To ensure reproducibility, optical measurements were acquired as the applied potentials were stepped between +1.0 V and –1.0 V (potentials measured against Ag/AgCl) for a total of 10 times. The %T observed in Figure 4.6b from the $n = 0$ spot for both WO_3 gratings and ZnO-WO_3 gratings varied reversibly with the applied potential as a result of the electrochromic properties of WO_3. For the WO_3 grating, %T switched between 79% at +1.0 V to 27% at −1.0 V vs. Ag/AgCl. This variation in %T is indicative of the electrochromic effects displayed by the WO_3 grating, with larger Δ%T values indicating a greater optical contrast under an applied potential. At −1.0 V, Li ion intercalation and electron injection into the WO_3 grating lead to an increase in κ and thus the large increase (Δ%T = 52%) in light absorption. This effect has been observed previously, on both planar WO_3 films and gratings.[24-26] Similar electrochromic effects were observed for the ZnO-WO_3 gratings, with a Δ%T = 46%. However, the average intensity of the transmitted light was lower for the ZnO-WO_3 gratings as compared to undecorated WO_3 gratings (T_{ave} = 40% vs T_{ave} = 55%). This decrease is expected from the absorption spectra results discussed in the previous section.

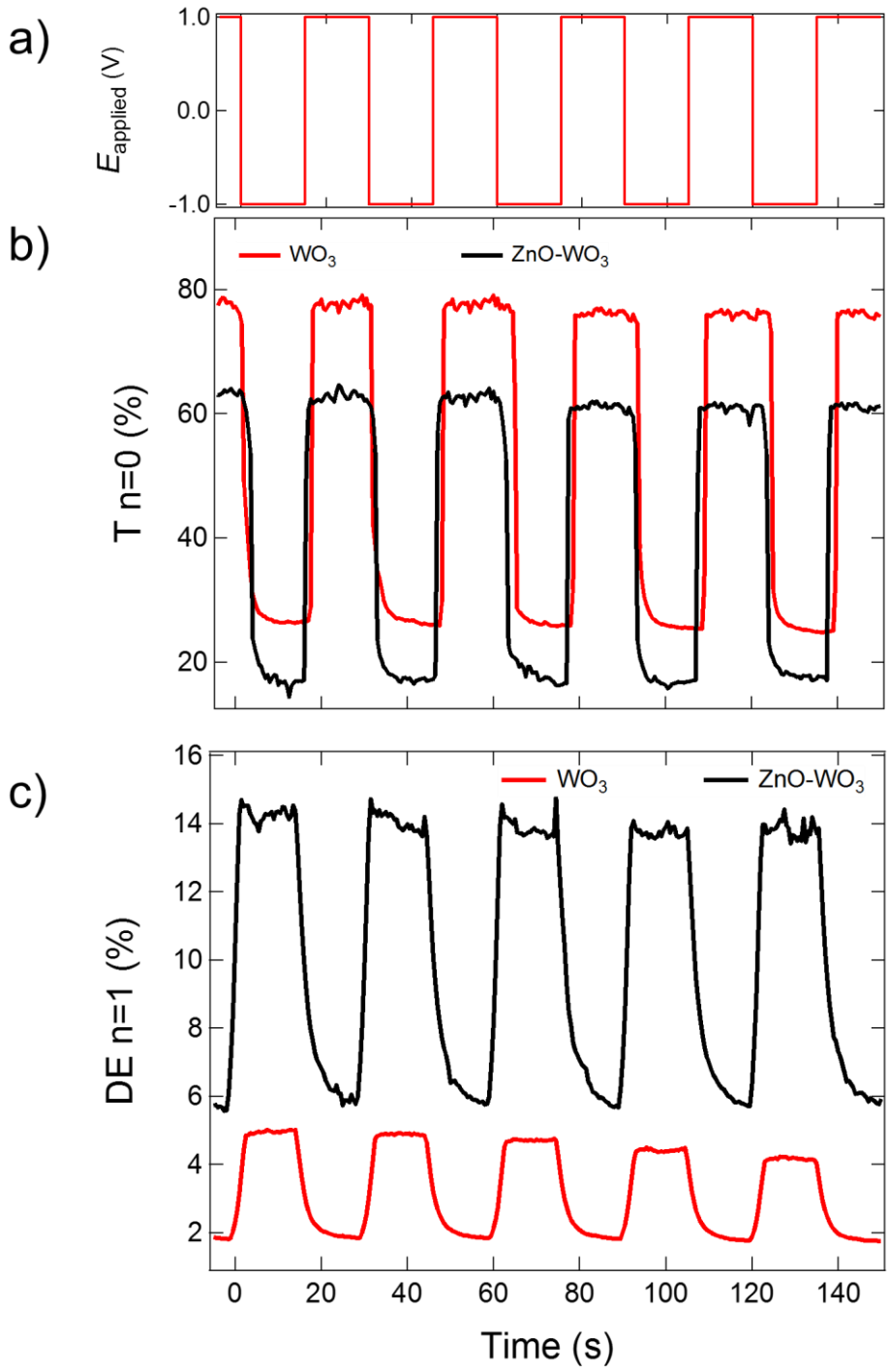

Figure 4.6. Optical measurements of ZnO-WO_3 and WO_3 gratings after a) applied potentials of −1.0 V and +1.0 V vs. Ag/AgCl showing the b) transmittance at the n = 0 spot and the c) diffraction efficiency at the n = 1 spot.

Then, for electrodiffraction experiments, optical measurements were also collected *in situ* at normal incidence at $\lambda = 633$ nm in an electrochemical cell containing 0.1 M $LiClO_4$ in polycarbonate using the gratings' $n = 0$ transmission measurements at +1.0 V vs. Ag/AgCl (the gratings' most transmissive state) as reference. To ensure reproducibility, %DE measurements were reported as the applied potentials were stepped between +1.0 V and –1.0 V (potentials measured against Ag/AgCl) for a total of 10 times. In contrast to the electrochromic behavior, both the average and the electrochemically modulated diffraction efficiency (%DE) observed for the $n = 1$ diffraction spot were greater for the ZnO-WO_3 gratings compared to the WO_3 gratings. It should also be noted that the electrochemical modulation of %DE was 180° out of phase with the modulation of %T. A comparison of Figures 4.6b and 4.6c revealed that the more absorptive state at $n = 0$ (for the applied potential −1.0 V vs. Ag/AgCl) displayed a low %T but a high %DE, and vice versa at +1.0 V vs. Ag/AgCl. From the red trace in Figure 4.6c, an average %DE of 3.2% and an electrochemically modulated Δ%DE of 2.4% were observed for WO_3 gratings. As for the ZnO-WO_3 gratings (black trace in Figure 4.6c), the average %DE increased to 10%, and the electrodiffraction increased to a Δ%DE of 9.7% – four times higher than the gratings without ZnO. A similar effect was observed for the case of the ZnO-PEDOT and PEDOT gratings. As seen in the Figure 4.7b, for PEDOT gratings, %T and Δ%T were 45% and 35% respectively; these values decreased to 36% and 27% for ZnO-PEDOT gratings.

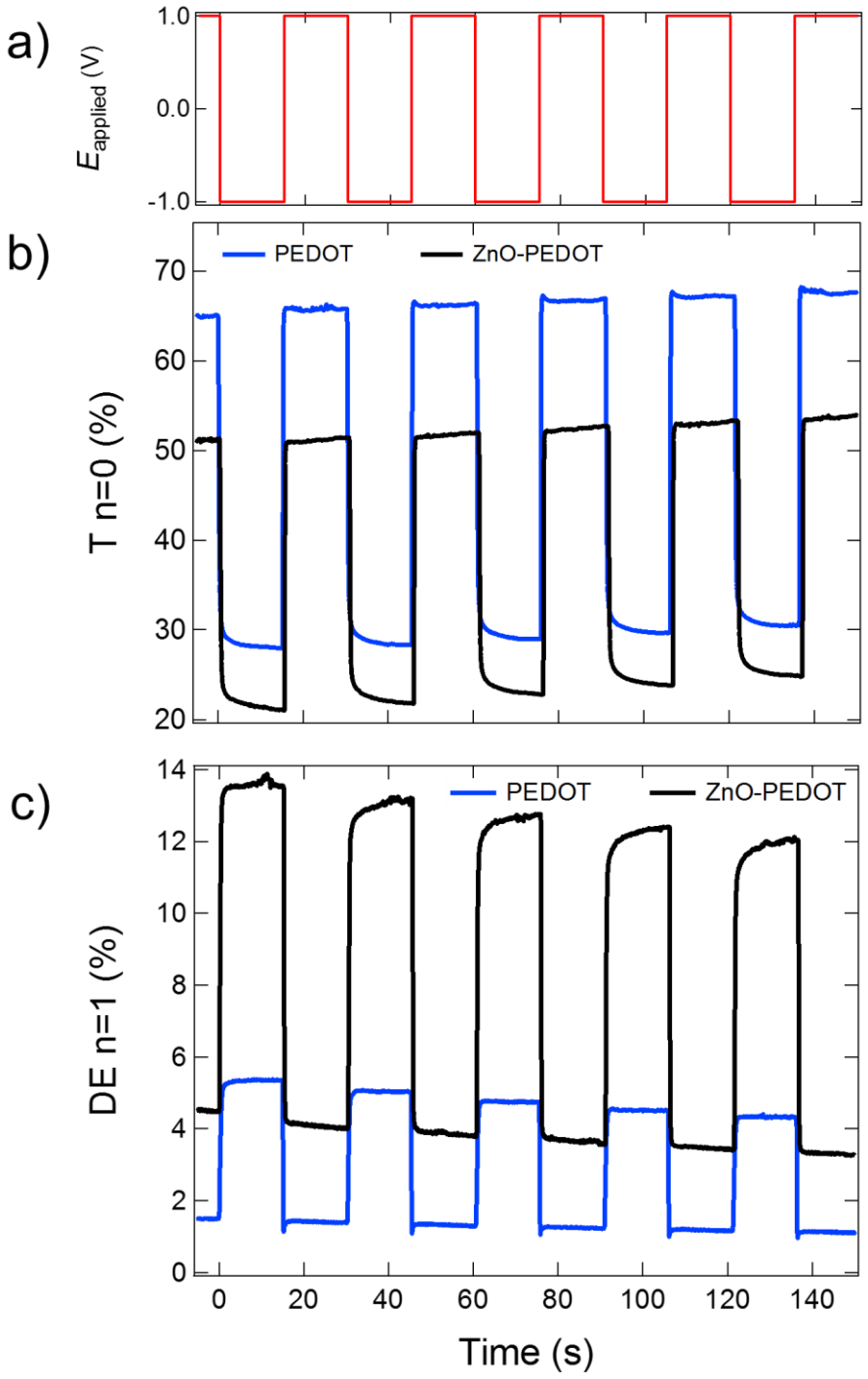

Figure 4.7. Optical measurements of ZnO-PEDOT and PEDOT gratings after a) applied potentials of −1.0 V and +1.0 V vs. Ag/AgCl showing the b) transmittance at the n = 0 spot and the c) diffraction efficiency at the n = 1 spot.

However, the diffraction efficiencies again showed significant increases: an average %DE and Δ%DE were 3.5% and 2.8% for PEDOT gratings, but increased significantly to 8.5% and 8.3% respectively as shown in Figure 4.6c. The drastic increase of Δ%DE displayed by the ZnO-WO_3 and ZnO-PEDOT gratings compared to their counterpart WO_3 and PEDOT gratings indicates a significant improvement of their electrodiffractive performance, likely due to optical coupling between ZnO and the host material. By reporting Δ%DE values, we have demonstrated that we are able to quantify optical coupling between the non-absorptive nanostructured ZnO overlayer and the absorptive host material (WO_3 and PEDOT).

To understand these changes in the average %DE and Δ%DE, we need to consider the contributions to η and κ for the composite gratings. In the case of thin gratings, the diffraction efficiency *DE* is a linear combination of an absorptive component and a phase component (Eqn. (6)):[22, 38, 50]

$$DE = a(\Delta\kappa)^2 + b(\Delta\eta)^2 \qquad (6)$$

This equation can be used to explain the increases in the average %DE, but not the electrodiffractive component (Δ%DE). For the case of the composite ZnO-WO_3 and ZnO-PEDOT gratings in this paper, an additional coupling between the ZnO and the absorptive WO_3 or PEDOT is observed, even though no electrodiffractive effect ($\Delta\kappa = \Delta\eta = 0$) is observed with ZnO gratings alone (optical measurements shown in Supporting Information in Appendix C). Instead, the nanostructured ZnO overlayer redirects light into the electrochromic WO_3 or PEDOT component of the grating. This type of optical coupling occurs because the electrodeposited nanostructured ZnO coating is on the same scale as the light; similar optical effects have been previously observed in calculations of the diffraction efficiency of taller gratings.[35, 50] Furthermore, the high surface area, nanostructured nature of the ZnO provides an

additional coupling mechanism via a series of total internal reflection from the ZnO to the absorptive material underneath.[6] To support our proposed mechanism for optical coupling, we showed that ZnO-PEDOT gratings without a fully covered ZnO overlayer displayed much weaker electrodiffractive effects (measurements in Supporting Information in Appendix C). ZnO-PEDOT gratings with a sparse ZnO overlayer only displayed a 1.5-fold enhancement of Δ%DE compared to PEDOT gratings, which indicates weaker optical coupling between the sparse ZnO overlayer and the absorptive material underneath. Thus, the presence of the electrodeposited ZnO, in a combination of the nanoscale structure and metamaterial patterning, is crucial for creating enhanced electrodiffraction.

4.4 Conclusions

The enhanced absorption and electrodiffraction observed from the composite ZnO-WO_3 and ZnO-PEDOT gratings described in this paper clearly demonstrate that there is a strong optical coupling between the electrodeposited nanostructured ZnO overlayer and the electrochromic thin film layer underneath. This coupling has some significant implications; the presence of both nanoscale structuring and metamaterial patterning (e.g., gratings, nanocone arrays, or nanoring arrays) are both required for this coupling to occur. The electrodiffraction from these gratings increases in the presence of the high surface area nanostructured ZnO, even though the ZnO itself has no absorptive (κ) or electrochromic (Δκ) behavior. In these gratings, the ZnO enhances the delivery of light to the underlying electrochromic materials via optical coupling. We have also observed this coupling effect previously in the enhanced antireflectivity of PEDOT and gold nanocone arrays that were coated with electrodeposited ZnO

nanostructures.[7] Going forward, we should be able to employ this coupling effect to enhance the production of electron-hole pairs by enhancing the optical absorption of TiO_2, In_2O_3, or Si semiconductor patterned gratings, nanocone arrays, or nanoring arrays.

4.5 Acknowledgments

This work was supported by the National Science Foundation through grant CHE-1403506. SEM and XPS analyses were performed at the Irvine Materials Research Institute (IMRI) at UC Irvine. UV-Vis/NIR measurements were performed at the UC Irvine Laser Spectroscopy Labs. The authors would also like to thank the Penner Group for their help with AFM measurements.

4.6 References

1. Murakoshi, K.; Yanagida, S.; Capel, M.; Castner, E. W. Interfacial Electron Transfer Dynamics of Photosensitized Zinc Oxide Nanoclusters. In *Nanostructured Materials*, American Chemical Society: 1997; Vol. 679, pp 221-238.

2. Conradt, J.; Sartor, J.; Thiele, C.; Maier-Flaig, F.; Fallert, J.; Kalt, H.; Schneider, R.; Fotouhi, M.; Pfundstein, P.; Zibat, V.; Gerthsen, D. Catalyst-Free Growth of Zinc Oxide Nanorod Arrays on Sputtered Aluminum-Doped Zinc Oxide for Photovoltaic Applications. *J. Phys. Chem. C* **2011,** *115*, 3539-3543.

3. Gonzalez-Valls, I.; Lira-Cantu, M. Vertically-Aligned Nanostructures of ZnO for Excitonic Solar Cells: A Review. *Energy Environ. Sci.* **2009,** *2*, 19-34.

4. Müller, J.; Rech, B.; Springer, J.; Vanecek, M. TCO and Light Trapping in Silicon Thin Film Solar Cells. *Sol. Energy* **2004,** *77*, 917-930.

5. Battaglia, C.; Escarré, J.; Söderström, K.; Charrière, M.; Despeisse, M.; Haug, F.-J.; Ballif, C. Nanomoulding of Transparent Zinc Oxide Electrodes for Efficient Light Trapping in Solar Cells. *Nat. Photon.* **2011,** *5*, 535.

6. Lin, A.; Phillips, J. Optimization of Random Diffraction Gratings in Thin-Film Solar Cells using Genetic Algorithms. *Sol. Energy Mater Sol. Cells* **2008,** *92*, 1689-1696.

7. Fung, H. W. M.; So, S.; Kartub, K.; Loget, G.; Corn, R. M. Ultra-Antireflective Electrodeposited Plasmonic and PEDOT Nanocone Array Surfaces. *J. Phys. Chem. C* **2017,** *121*, 22377-22383.

8. Yaqoob, Z.; Riza, N. A. Passive Optics No-Moving-Parts Barcode Scanners. *IEEE Photonics Technology Letters* **2004,** *16*, 954-956.

9. Boudoux, C.; Yun, S. H.; Oh, W. Y.; White, W. M.; Iftimia, N. V.; Shishkov, M.; Bouma, B. E.; Tearney, G. J. Rapid Wavelength-Swept Spectrally Encoded Confocal Microscopy. *Opt. Express* **2005,** *13*, 8214-8221.

10. Chen, J.; Bos, P. J.; Vithana, H.; Johnson, D. L. An Electro-Optically Controlled Liquid Crystal Diffraction Grating. *Appl. Phys. Lett.* **1995,** *67*, 2588-2590.

11. Glesk, I.; Bock, P. J.; Cheben, P.; Schmid, J. H.; Lapointe, J.; Janz, S. All-Optical Switching using Nonlinear Subwavelength Mach-Zehnder on Silicon. *Opt. Express* **2011,** *19*, 14031-14039.

12. Williams, G. V. M.; Do, M. T. T.; Raymond, S. G.; Bhuiyan, M. D. H.; Kay, A. J. Optically Switchable Diffraction Grating in a Photochromic/Polymer Thin Film. *Appl. Opt.* **2015,** *54*, 6882-6886.

13. P. Bousquet. *Spectroscopy and Its Instrumentation*; Hilger: London, 1971.

14. C. Palmer. *Diffraction Grating Handbook*, 6th ed.; Newport Corporation: New York, 2005.

15. Arafat Hossain, M.; Canning, J.; Ast, S.; Cook, K.; Rutledge, P. J.; Jamalipour, A. Combined "Dual" Absorption and Fluorescence Smartphone Spectrometers. *Opt. Lett.* **2015,** *40*, 1737-1740.

16. Yang, M.; Wang, H.; Li, M.; He, J.-J. In *An Echelle Diffraction Grating for Imaging Spectrometer*, SPIE Optical Engineering + Applications, SPIE: 2016; p 7.

17. Cheben, P.; Bock, P. J.; Schmid, J. H.; Lapointe, J.; Janz, S.; Xu, D.-X.; Densmore, A.; Delâge, A.; Lamontagne, B.; Hall, T. J. Refractive Index Engineering with Subwavelength Gratings for Efficient Microphotonic Couplers and Planar Waveguide Multiplexers. *Opt. Lett.* **2010,** *35*, 2526-2528.

18. Knop, K. Rigorous Diffraction Theory for Transmission Phase Gratings with Deep Reectangular Grooves. *J. Opt. Soc. Am.* **1978,** *69*, 1206-1210.

19. Botten, I. C.; Craig, M. S.; McPhedran, R. C.; Adams, J. L.; Andrewartha, J. R. The Dielectric Lamellar Diffraction Grating. *Optica Acta* **1981,** *28*, 413-428.

20. Kondrachova, L. V.; May, R. A.; Cone, C. W.; Vanden Bout, D. A.; Stevenson, K. J. Evaluation of Lithium Ion Insertion Reactivity via Electrochromic Diffraction-Based Imaging. *Langmuir* **2009,** *25*, 2508-2518.

21. Bailey, R. C.; Hupp, J. T. Large-Scale Resonance Amplification of Optical Sensing of Volatile Compounds with Chemoresponsive Visible-Region Diffraction Gratings. *JACS* **2002,** *124*, 6767-6774.

22. Schanze, K. S.; Bergstedt, T. S.; Hauser, B. T.; Cavalaheiro, C. S. P. Photolithographically-Patterned Electroactive Films and Electrochemically Modulated Diffraction Gratings. *Langmuir* **2000,** *16*, 795-810.

23. Massari, A. M.; Stevenson, K. J.; Hupp, J. T. Development and Application of Patterned Conducting Polymer Thin Films as Chemoresponsive and Electrochemically Responsive Optical Diffraction Gratings. *J. Electroanal. Chem.* **2001,** *500*, 185-191.

24. Mortimer, R. J.; Rosseinsky, D. R.; Monk, P. M. S. Electrochromic Materials and Devices, 1st ed.; Wiley-VCH Verlag GmbH & Co. KGaA: Berlin, 2015.

25. Mortimer, R. J. Electrochromic Materials. *Annu. Rev. Mater. Res.* **2011,** *41*, 241-268.

26. Somani, P. R.; Radhakrishnan, S. Electrochromic Materials and Devices: Present and Future. *Mater. Chem. Phys.* **2003,** *77*, 117-133.27.

27. Granqvist, C. G. Electrochromics for Smart Windows: Oxide-Based Thin Films and Devices. *Thin Solid Films* **2014,** *564*, 1-38.

28. Kirchmeyer, S.; Elschner, A.; Reuter, K.; Lovenich, W.; Merker, U. *PEDOT: Principles and Applications of an Intrinsically Conductive Polymer*; Eds.; CRC Press, 2010.

29. Sankaran, B.; Reynolds, J. R. High-Contrast Electrochromic Polymers from Alkyl-Derivatized Poly(3,4-ethylenedioxythiophenes). *Macromolecules* **1997,** *30*, 2582-2588.

30. Mortimer, R. J. Organic Electrochromic Materials. *Electrochim. Acta* **1999,** *44*, 2971-2981.

31. Kumar, A.; Welsh, D. M.; Morvant, M. C.; Piroux, F.; Abboud, K. A.; Reynolds, J. R. Conducting Poly(3,4-alkylenedioxythiophene) Derivatives as Fast Electrochromics with High-Contrast Ratios. *Chem. Mater.* **1998,** *10*, 896-902.

32. Ruffo, R.; Celik-Cochet, A.; Posset, U.; Mari, C. M.; Schottner, G. Mechanistic Study of the Redox Process of an *In Situ* Oxidatively Polymerised Poly(3,4-ethylene-dioxythiophene) Film. *Sol. Energy Mater. Sol. Cells* **2008,** *92*, 140-145.

33. Von Rottkay, K.; Rubin, M.; Wen, S. J. Optical Indices of Electrochromic Tungsten Oxide. *Thin Solid Films* **1997,** *306*, 10-16.

34. Pettersson, L. A. A.; Ghosh, S.; Inganäs, O. Optical Anisotropy in Thin Films of Poly(3,4-ethylenedioxythiophene)–Poly(4-styrenesulfonate). *Org. Electron.* **2002,** *3*, 143-148.

35. Dang, X.; Massari, A. M.; Hupp, J. T. Electrochemically Modulated Diffraction - A Novel Strategy for the Determination of Conduction-Band-Edge Energies for Nanocrystalline Thin-Film Semiconductor Electrodes. *Electrochem. Solid-State Lett.* **2000,** *3*, 555-558.

36. Kim, Y.; Kim, Y.; Kim, S.; Kim, E. Electrochromic Diffraction from Nanopatterned Poly(3-hexylthiophene). *ACS Nano* **2010,** *4*, 5277-5284.

37. Park, C.; Na, J.; Han, M.; Kim, E. Transparent Electrochemical Gratings from a Patterned Bistable Silver Mirror. *ACS Nano* **2017,** *11*, 6977-6984.

38. Tian, S.; Armstrong, N. R.; Knoll, W. Electrochemically Tunable Surface-Plasmon-Enhanced Diffraction Gratings and their (Bio-)sensing Applications. *Langmuir* **2005,** *21*, 4656-4660.

39. Matsui, T.; Ozaki, M.; Yoshino, K. In *Electro-Tunable Liquid Crystal Waveguide Laser*, Optical Science and Technology, the SPIE 49th Annual Meeting, SPIE: 2004; p 12.

40. Meulenkamp, E. A. Mechanism of WO_3 Electrodeposition from Peroxy-Tungstate Solution. *J. Electrochem. Soc.* **1997,** *144*, 1664-1671.

41. Cai, G.; Cui, M.; Kumar, V.; Darmawan, P.; Wang, J.; Wang, X.; Lee-Sie Eh, A.; Qian, K.; Lee, P. S. Ultra-Large Optical Modulation of Electrochromic Porous WO_3 Film and the Local Monitoring of Redox Activity. *Chem Sci.* **2016,** *7*, 1373-1382.

42. So, S.; Fung, H. W. M.; Kartub, K.; Maley, A. M.; Corn, R. M. Fabrication of PEDOT Nanocone Arrays with Electrochemically Modulated Broadband Antireflective Properties. *J. Phys. Chem. Lett.* **2017,** *8*, 576-579.

43. Randriamahazaka, H.; Sini, G.; Tran Van, F. Electrodeposition Mechanisms and Electrochemical Behavior of Poly(3,4-ethylenedithiathiophene). *J. Phys. Chem. C* **2007,** *111*, 4553-4560.

44. Nguyen, V.-Q.; Schaming, D.; Martin, P.; Lacroix, J.-C. Highly Resolved Nanostructured PEDOT on Large Areas by Nanosphere Lithography and Electrodeposition. *ACS Appl. Mater. Interfaces* **2015,** *7*, 21673-21681.

45. Donavan, K. C.; Arter, J. A.; Pilolli, R.; Cioffi, N.; Weiss, G. A.; Penner, R. M. Virus−Poly(3,4-ethylenedioxythiophene) Composite Films for Impedance-Based Biosensing. *Anal. Chem.* **2011,** *83*, 2420-2424.

46. Illy, B. N.; Cruickshank, A. C.; Schumann, S.; Da Campo, R.; Jones, T. S.; Heutz, S.; McLachlan, M. A.; McComb, D. W.; Riley, D. J.; Ryan, M. P. Electrodeposition of ZnO Layers for Photovoltaic Applications: Controlling Film Thickness and Orientation. *J. Mater. Chem.* **2011,** *21*, 12949-12957.

47. Sun, S.; Jiao, S.; Zhang, K.; Wang, D.; Gao, S.; Li, H.; Wang, J.; Yu, Q.; Guo, F.; Zhao, L. Nucleation Effect and Growth Mechanism of ZnO Nanostructures by Electrodeposition from Aqueous Zinc Nitrate Baths. *J. Cryst. Growth* **2012,** *359*, 15-19.

48. Xu, L.; Chen, Q.; Xu, D. Hierarchical ZnO Nanostructures Obtained by Electrodeposition. *J. Phys. Chem. C* **2007,** *111*, 11560-11565.

49. Deutschmann, T.; Oesterschulze, E. Micro-Structured Electrochromic Device Based on Poly(3,4-ethylenedioxythiophene). *J. Micromech. Microeng.* **2013,** *23*, 065032.

50. Nelson, K. A.; Casalegno, R.; Miller, R. J. D.; Fayer, M. D. Laser-Induced Excited State and Ultrasonic Wave Gratings: Amplitude and Phase Grating Contributions to Diffraction. *J. Chem. Phys.* **1982,** *77*, 1144-1152.

Appendix A

Supporting Information for

Fabrication of PEDOT Nanocone Arrays with Electrochemically Modulated Broadband Antireflective Properties

A.1 PEDOT Electrodeposition Current Density vs. Time

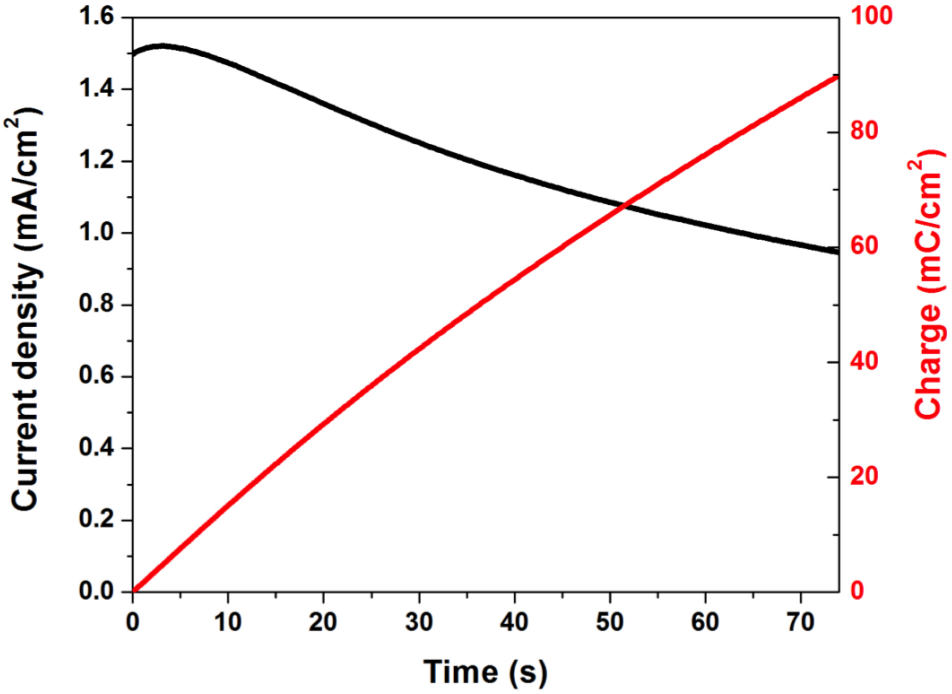

Figure A.1. Current density and charge curves during PEDOT electropolymerzation and electrodeposition at +1.0V on thin PEDOT:PSS coated FTO conductive substrate.

A.2 Electrodeposited PEDOT Film Thickness

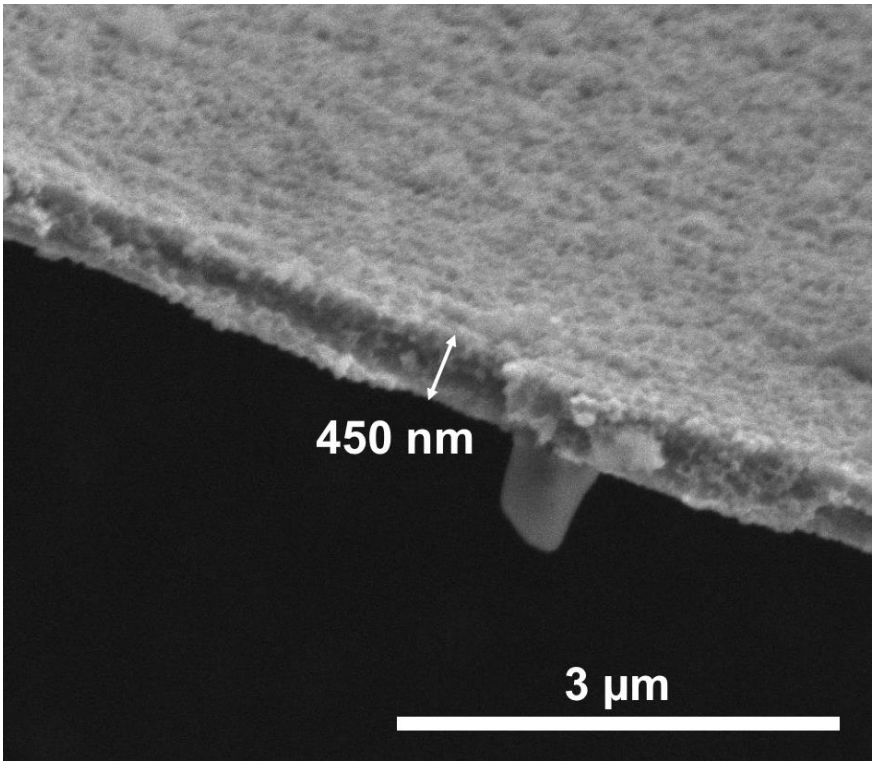

Figure A.2. SEM image shows that an unmodified electrodeposited PEDOT film has a film thickness of 450 nm.

A.3 Electrochromic Behavior of an Unmodified PEDOT Planar Thin Film

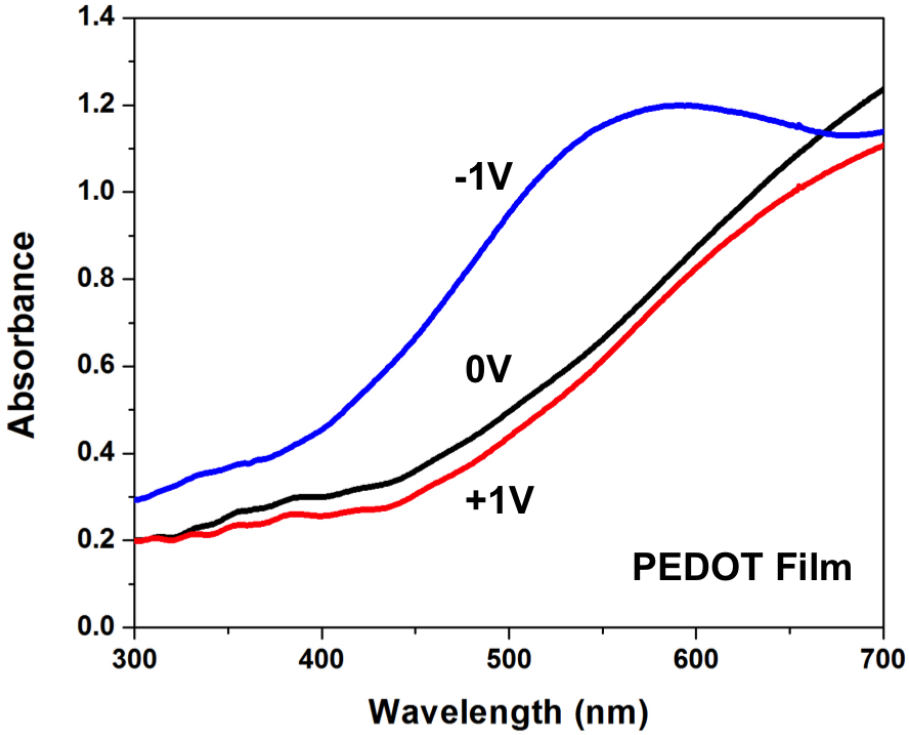

Figure A.3. Electrochromic behavior of an unmodified PEDOT thin film. UV–visible absorption spectra of PEDOT film removed from solution after 20s under potentiostatic control at three potentials: -1.0V (blue spectrum), 0.0V (black spectrum) and +1.0V (red spectrum) vs. Ag/AgCl.

A.4 References

(1) Kim, Y. H.; Sachse, C.; MacHala, M. L.; May, C.; Müller-Meskamp, L.; Leo, K. *Adv. Funct. Mater*. ***2011***, 21, 1076–1081.

(2) Park, H.; Shi, Y.; Kong, J. *Nanoscale* ***2013***, 5, 8934–8939.

Appendix B

Supporting Information for

Ultra-Antireflective Electrodeposited Plasmonic and PEDOT Nanocone Array Surfaces

B.1 ZnO Electrodeposition Current Density vs. Time

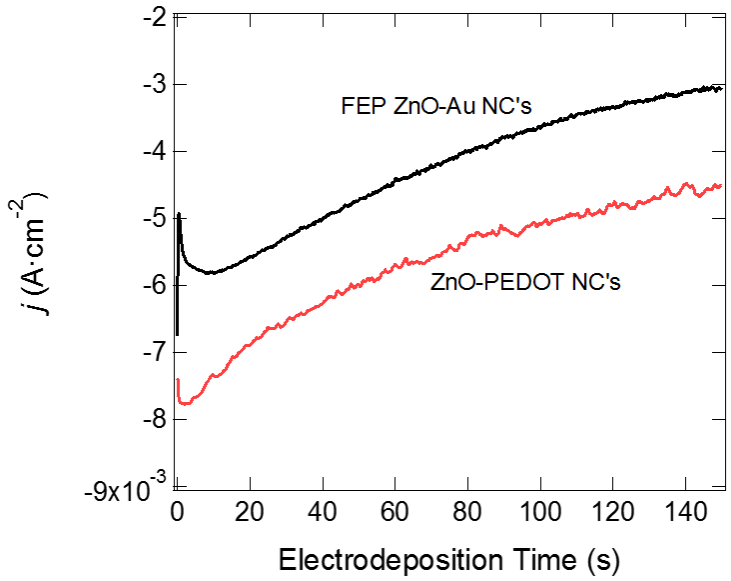

Figure B.1. Electrochemical characterization of the formation of the nanostructured ZnO thin film via electrodeposition.

B.2 XRD Analysis of ZnO-Coated Nanocone Arrays

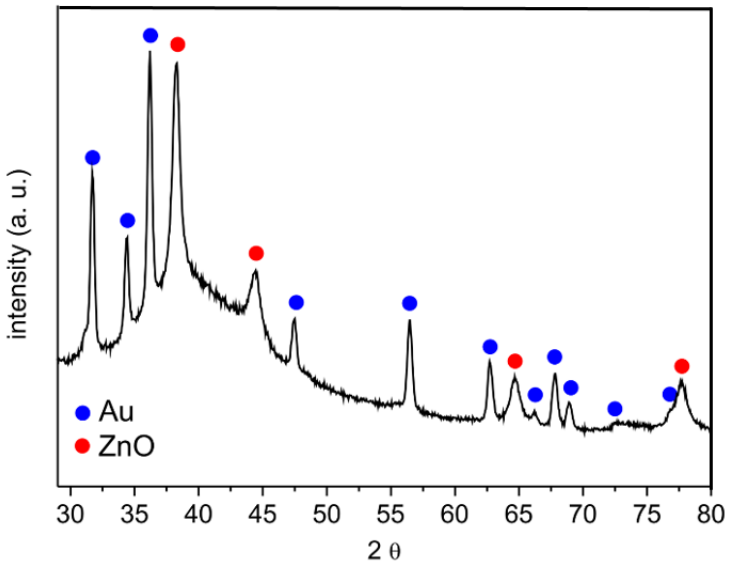

Figure B.2. XRD analysis of the ZnO-coated nanocone arrays indicates a wurzite structure with polycrystalline ZnO growing primarily in the <002> direction.

B.3 XPS Analysis of ZnO-Coated Nanocone Arrays

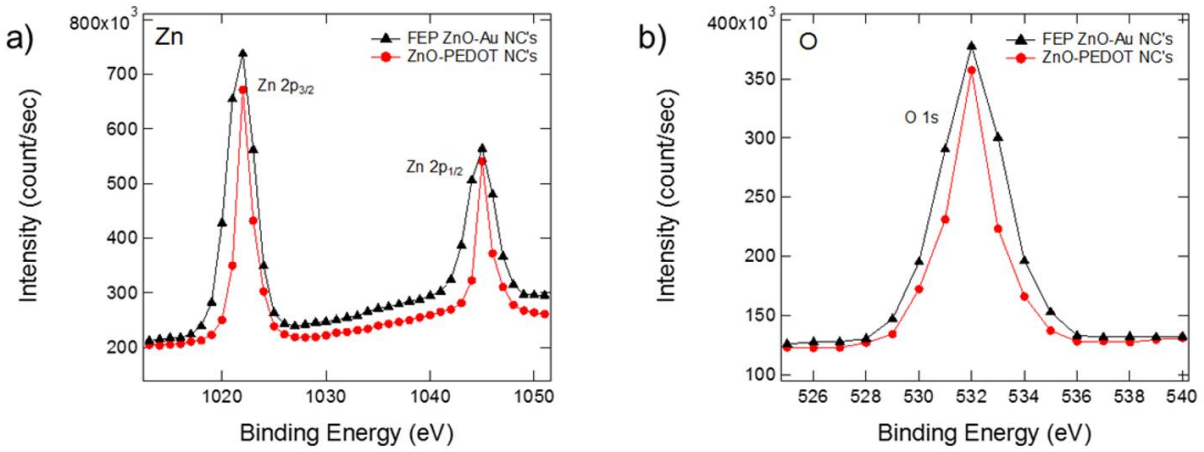

Figure B.3. XPS analysis confirming the presence of ZnO on the surface of the FEP ZnO-Au nanocone arrays and the ZnO-PEDOT nanocone arrays. a) indicates the presence of both Zn $2p_{3/2}$ and Zn $2p_{1/2}$ peaks, while b) indicates the presence of the O 1s peak.

B.4 Morphologies of ZnO-Coated Nanocone Arrays and Unmodified Planar ZnO Thin Film

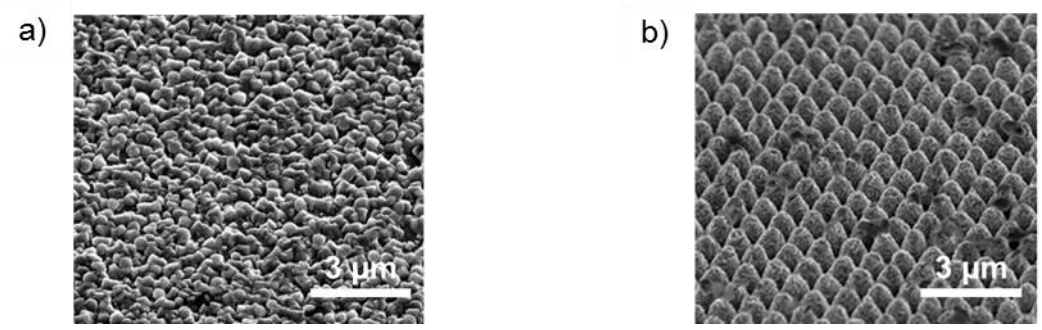

Figure B.4. SEM images of a) the planar ZnO thin film surface and b) the ZnO nanocone arrays used in the methylene blue degradation. For the planar ZnO thin film, the ZnO crystals are packed tightly together, reducing the surface roughness factor compared to the periodic ZnO-coated nanocone arrays.

B.5 Experimental Details for Simulated %R Measurements for Nanocone Arrays

The simulated %R measurements were obtained using 11-phase Fresnel calculations, where n_1 = air, n_{11} = bulk Au or ZnO-Au, and n_2, n_3, … , n_{10} = the effective refractive index calculated by averaging the refractive indices of air and the nanocone structure as a function of the distance away from the bottom of the nanocone. For Au, n_{11} at various λ was referenced from values reported in literature. To calculate the real part of n_2, n_3, … , n_{10}, the following formula was used:

$n_{\text{xreal}} = n_{xreal} = n_{xreal+1} + (\frac{1-n_{11real}}{10})$, where $2 < x < 10$

To calculate the imaginary part of n_2, n_3, … , n_{10}, the following formula was used:

$n_{\text{xim}} = n_{11im}e^{-(\frac{11-x}{7})}$, where $2 < x < 10$

For ZnO-Au, n_{11} at various λ was modeled using the refractive index of ZnO reported in literature. However, we also combined the imaginary part of Au's refractive index to model the absorptive nature of the ZnO-Au nanocone arrays (e.g., at 600 nm, $n_{\text{Au}} = 0.24 + 3.10i$, $n_{\text{ZnO}} = 2.00 + 0i$, and ZnO-Au is modeled using $n_{\text{ZnO-Au}} = 2.00 + 3.10i$). To calculate the real and imaginary parts of n_2, n_3, … , n_{10} for the ZnO-Au nanocone arrays, the same formulas listed above were used. Other important parameters for the Fresnel calculations include setting the film height for each phase from n_2, n_3, … , n_{10} to 100 nm, and setting the angle of incidence to 8°.

B.6 Igor Pro Macro for 11-Phase Fresnel Reflectivity Measurements for Simulated %R Measurements for Nanocone Arrays

```
Make/N=900/D Refs,theta,rad,Refp
Make/N=900/D/C
rs1,rs2,rs3,rs4,rs5,rs6,rs7,rs8,rs9,rs10,rs12,rs13,rs14,rs15,rs16,rs17,rs18,rs19,rs110,c1,c2,c3,c4,c5,c6,c7,c
8,c9,c10,c11,b1,b2,b3,b4,b5,b6,b7,b8,b9,rp1,rp2,rp3,rp4,rp5,rp6,rp7,rp8,rp9,rp10,rp12,rp13,rp14,rp15,rp
16,rp17,rp18,rp19,rp110
variable lambda := 496
variable h := 100.0
variable/c ic := cmplx(0,1)
variable/c n1 := cmplx(1.00,0)
variable/c n2 := cmplx(0.9916,0.508674)
variable/c n3 := cmplx(0.9832,0.586788)
variable/c n4 := cmplx(0.9748,0.676898)
variable/c n5 := cmplx(0.9664,0.780846)
variable/c n6 := cmplx(0.958,0.900757)
variable/c n7 := cmplx(0.9496,1.039081)
variable/c n8 := cmplx(0.9412,1.198648)
variable/c n9 := cmplx(0.9328,1.382718)
variable/c n10 := cmplx(0.9244,1.595055)
variable/c n11 := cmplx(0.916,1.84)
theta := x/10
rad := theta*pi/180
c1 := n1*cos(rad)
c2 := sqrt(n2^2-(n1*sin(rad))^2)
c3 := sqrt(n3^2-(n1*sin(rad))^2)
c4 := sqrt(n4^2-(n1*sin(rad))^2)
c5 := sqrt(n5^2-(n1*sin(rad))^2)
c6 := sqrt(n6^2-(n1*sin(rad))^2)
c7 := sqrt(n7^2-(n1*sin(rad))^2)
c8 := sqrt(n8^2-(n1*sin(rad))^2)
c9 := sqrt(n9^2-(n1*sin(rad))^2)
c10 := sqrt(n10^2-(n1*sin(rad))^2)
c11 := sqrt(n11^2-(n1*sin(rad))^2)
```

Appendix C

Supporting Information for

Quantitative Characterization of Optical Coupling in Nanoporous ZnO-WO_3 and ZnO-PEDOT Composite Electrodeposited Gratings using Electrodiffraction Measurements

C.1 Morphology of WO_3 and PEDOT Gratings

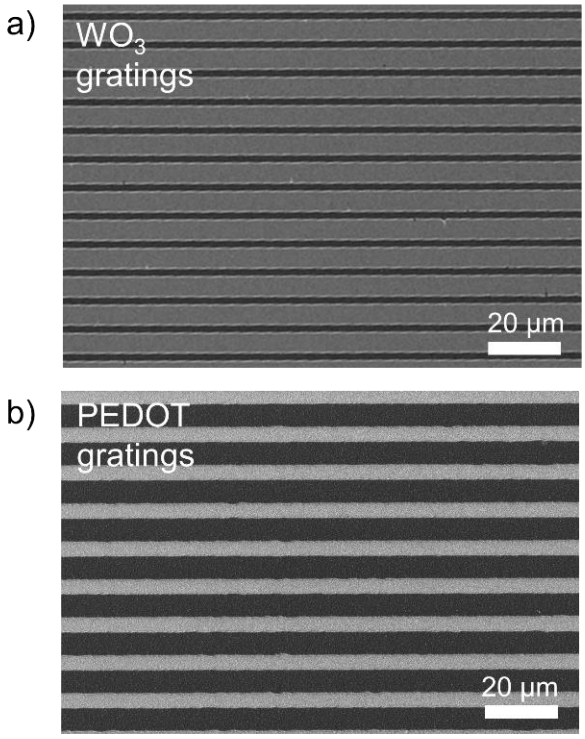

Figure C.1. SEM images of a) WO_3 gratings and b) PEDOT gratings.

C.2 AFM Measurements of ZnO Composite Gratings

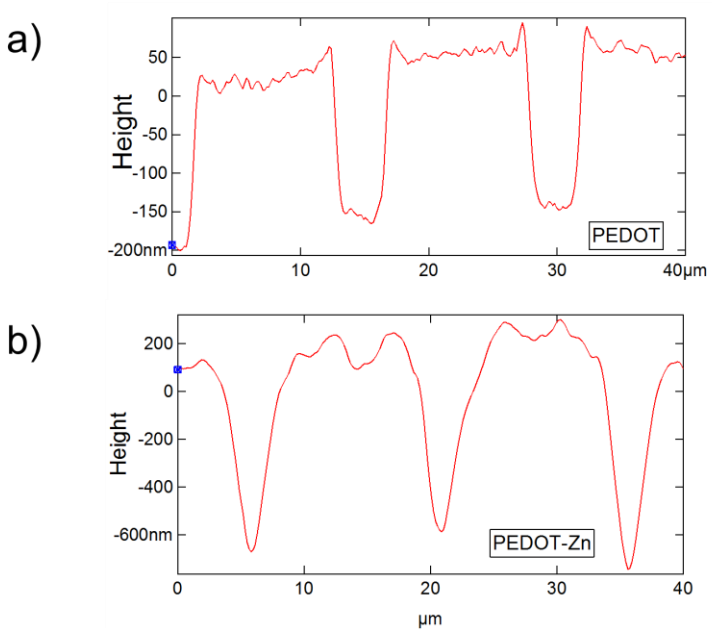

Figure C.2. AFM measurements revealed the heights of a) the PEDOT layer and b) the ZnO overlayer from a ZnO-PEDOT grating. Cross-sectional SEM images of c) the ZnO-PEDOT grating sample confirm AFM measurements and show the various components of the composite ZnO-PEDOT grating.

C.3 XPS Characterization of ZnO Composite Gratings

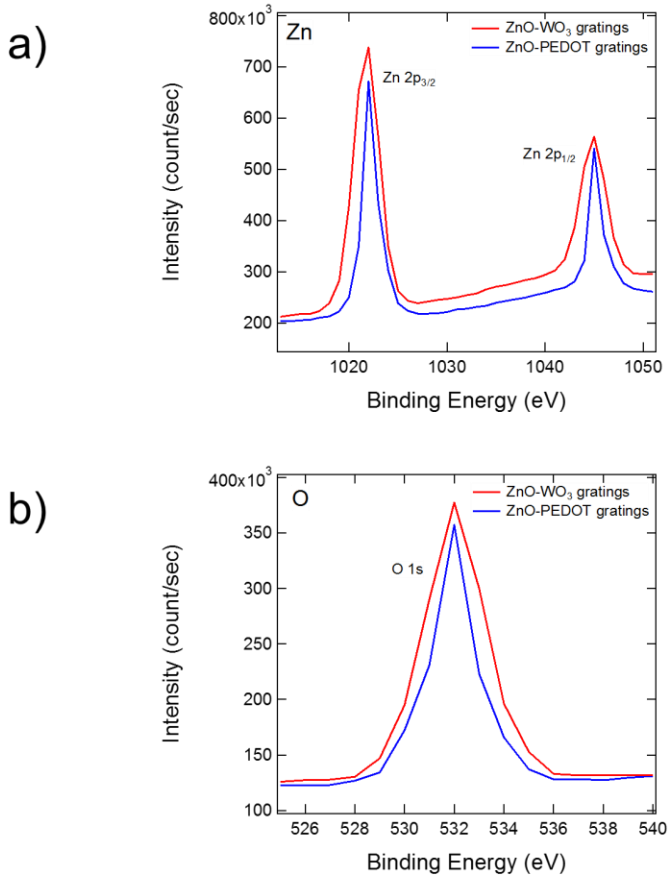

Figure C.3. XPS measurements confirmed the formation of a ZnO overlayer on our ZnO-WO_3 gratings and ZnO-PEDOT gratings.

C.4 Electrochromic and Electrodiffrative Measurements for ZnO Only Gratings

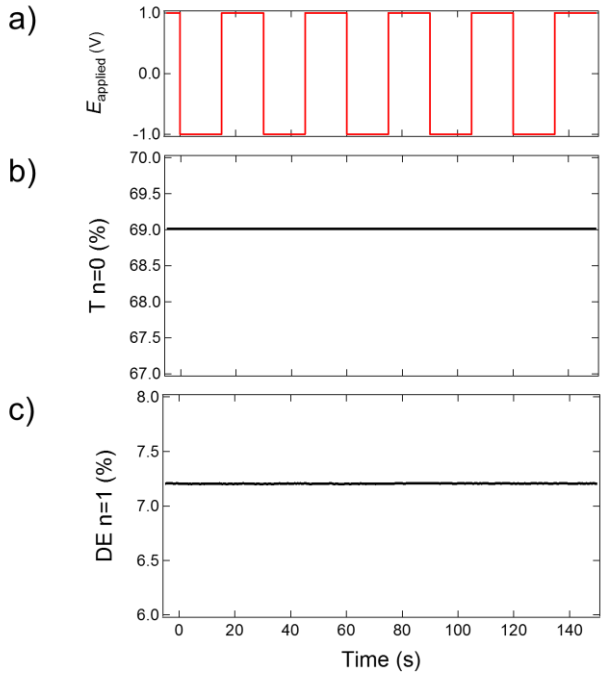

Figure C.4. Optical measurements of ZnO only gratings after a) applied potentials of −1.0 V and +1.0 V vs. Ag/AgCl showing the b) transmittance at the n = 0 spot and the c) diffraction efficiency at the n = 1 spot.

C.5 Electrochromic and Electrodiffrative Measurements of Sparsely ZnO Covered ZnO Composite Gratings

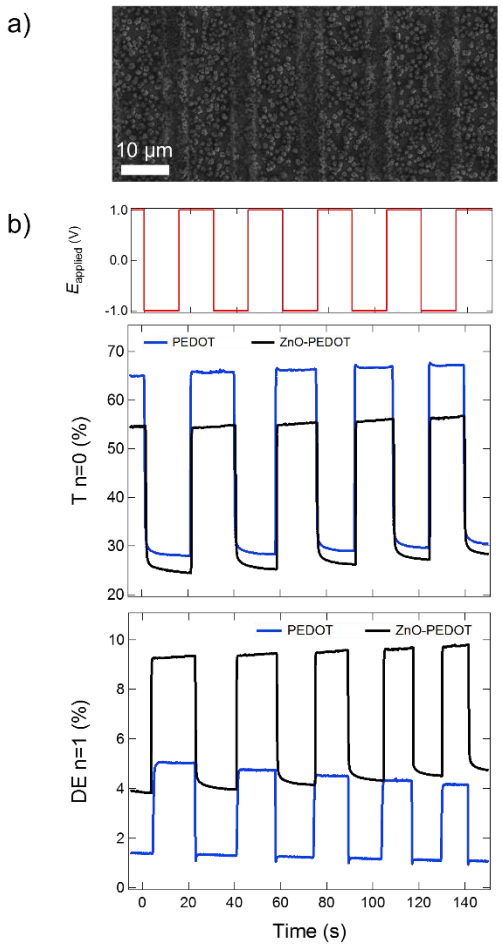

Figure C.5. a) SEM image of a sparsely ZnO covered ZnO-PEDOT grating. b) Optical data reveals a much weaker electrodiffractive effect at applied potentials of +1.0 V and –1.0 V vs. Ag/AgCl for the sparsely ZnO covered ZnO-PEDOT grating (with ZnO electrodeposition time of 300 s). The ZnO-PEDOT grating here only displayed a 1.5-fold enhancement of Δ%DE compared to the PEDOT grating.